The Study of Atomic Autoionisation and Inner Shell Photoionisation of Diatomic Molecules using Photoelectron Spectroscopy

by

B J Goodwin

Physics Department

A thesis submitted to the

University of Manchester for the degree

of doctor of philosophy

in the Faculty of Science

October 1991

Th 16893
(PSWG9)
Brian John

✓

CONTENTS

ABSTRACT

A photoelectron spectrometer incorporating a new type of position sensitive multidetector has been used at the Daresbury Synchrotron Radiation Source to study the spectra of N_2, CO and HCl. Results have been obtained with a two dimensional scanning technique where photoelectron intensity is measured as a function of collection energy and incident photon energy.

The increased sensitivity afforded by the new detector has revealed many satellite lines in the inner-valence ionisation region for each gas. Thus the extent of the breakdown of the molecular orbital picture of ionisation has been established for these diatomic molecules. Atomic autoionisation following neutral photodissociation of each target gas has also been studied.

No portion of the work referred to
in this thesis has been submitted in support of
an application for another degree or qualification
of this or any other university or
other institute of learning.

FORWARD

Having graduated from the University of Manchester in 1987 the author continued to study at the same University and in 1988 was awarded a Diploma in Advanced Studies in Science. From October 1987 to October 1990 the author was supported by the Science and Engineering Research Council.

ACKNOWLEDGEMENTS

I would foremost like to thank Dr John Comer for his excellent supervision and support. Without his patience and ability to smile in the face of disaster this thesis would not bear my name.

Thanks are also due to:

Dr Ant Wills for his patience, understanding and expertise.

Dr Tim Reddish for help with the data analysis.

Dr Fred Currell for mixing brilliance with foolishness.

Dr J.V.Hatfield and members of the Department of Electrical Engineering and Electronics (UMIST) for their expertise in the development of the detector.

The staff at the Daresbury Synchrotron, in particular Dr Mike MacDonald.

Alan Venables and Dave Coleman for technical advice and expertise.

Neil Morris and Dr Nick Bowring for invaluable computing assistance.

Members of the AMP group past and present, particularly Dr Steve L Hill, for all their help and support.

The S.E.R.C. for financial assistance.

I am also grateful to my Mother, Father, Sister, Brother, Patrick, Elaine and Bernard for their love, encouragement and financial assistance.

Finally, I thank all my friends for their encouragement.

CHAPTER ONE

INTRODUCTION AND REVIEW OF PHOTOELECTRON SPECTROSCOPY

1.1 Introduction

Photoionisation is the process of ejecting an electron from an atom or molecule using radiation and has been studied for many years. In 1887, Hertz [1] first used ultraviolet light incident upon a solid to observe the photoelectric effect. This method of study was soon applied to atoms and molecules in the gas phase. In 1905, Einstein [2] used such observations to formulate the photoelectric effect in terms of photons.

In photoelectron spectroscopy monochromatic radiation is used to eject electrons from atoms and molecules. The kinetic energy and angular distribution of the ejected electrons are then analysed to provide information on the structural properties of the ions produced.

In the most conceptually simple process, a monochromatic photon beam of energy $h\nu$, incident on an atom or molecule may remove an electron if $h\nu$ is greater than the binding energy of that electron. If the recoil energy of the ion is neglected, energy conservation gives the kinetic energy of an electron ejected from an orbital i as

$$E_i = h\nu - I_i \quad \text{....1.1}$$

where I_i is the ionisation potential or binding energy of the

electron in the i^{th} orbital.

More complex analysis can provide information on the energy levels and electron configurations of atoms and molecules.In the case of molecules, an understanding of the internal dynamics and geometrical structure can be gained if the vibrational states of the ion can be resolved.

At present, high resolution photoelectron spectroscopy can provide information on the vibrational frequency of diatomic molecules, the resolving power of this technique being of the order of 5×10^{-21}J (30meV). An improvement of a factor of 10 would allow rotational fine structure to be observed, and such developments are an exciting prospect.

The photon energy required to remove the most loosely bound electrons corresponds to the first ionisation potential, which falls between 4.3 and 24.6eV for all atoms and molecules. At higher photon energy an electron may be removed from an inner shell. Electrons from higher orbitals may subsequently fill this vacancy resulting in the emission of a photon or the ejection of an Auger electron. Furthermore, simultaneous excitation of more than one electron may occur during ionisation.

1.2 Multielectron Processes

Observations of the simultaneous excitation of two or more electrons, although normally much weaker than one electron processes, have attracted great interest. This is due to the failure of the simple independent electron picture to describe the processes, which are only possible because of electron correlations. Study of these phenomena therefore yields insight into

the nature of electron correlations.

Two Electron Excitation

Three types of double excitations can be considered:

a) Both of the electrons may be excited to bound levels. This can be represented by the configuration [core]n′l′n″l″ which is a resonant process since it will only occur for a single photon energy for each configuration. These states are most likely to decay by ejecting an electron, a process called autoionisation. The energy of the ejected electron is independent of the incident photon energy.

b) One electron may be excited to a bound level and the other is free, [core]n′l′ϵl″. This is an ionic state, where electron correlation has enabled the excitation of an electron to the n′l′ level to accompany the ionisation. Such states are commonly referred to as satellite states, producing satellite lines in the photoionisation spectra. One measure of the strength of electron correlation is the relative intensity of satellite lines to lines arising from single electron photoionisation processes.

c) Both electrons may be ejected, giving the configuration [core]ϵl′ϵl″. This is known as double photoionisation and leaves neither of the continuum electrons with well defined kinetic energy.

Double photoionisation is of particular interest at threshold where the two electrons are far from the core, with low kinetic energies,

allowing correlation effects to become dominant [3].

1.3 Atomic Autoionisation

Excitation of a diatomic molecule into a repulsive state may result in dissociation of the molecule into its atomic fragments:

$$AB + h\nu \rightarrow AB^* \rightarrow A + B^*$$

If, as shown above, an atomic fragment is left in an excited state, it may decay by ejection of an electron. This process is called atomic autoionisation and produces electrons with constant kinetic energy independent of the incident photon energy. Observations of this phenomenon provide information about both the molecule and the atomic fragment.

1.4 Rydberg Series

1.4.1 One electron excitation

This case can be conveniently represented by the excited configurations [core]n′l. The excited n′l electron (Rydberg electron) then forms a Rydberg series with $n' = n+1, n+2...\infty$ where n is the principle quantum number of the highest level electron in the core.

Increasing n′ corresponds to exciting the Rydberg electron into orbitals of progressively larger radii, where the nucleus and remaining electrons produce an essentially hydrogenic like field. In the series limit ($n' = \infty$) the Rydberg electron is free and a positive ion remains.

The energy of a series member with principle quantum number n is given by;

$$E_n = I - \frac{RZ^2}{(n-\delta)^2} = I - \frac{RZ^2}{(n^*)^2} \quad \ldots.1.2$$

where I is the ionisation potential representing the series limit, Z is the charge of the core without the Rydberg electron and R is the Rydberg energy (13.606eV).

The electric field seen by the Rydberg electron due to the core deviates from a true hydrogenic field (a coulomb field of point charge Z) by an amount represented by the quantum defect, δ. This deviation arises from the penetration of the wavefunction of the excited electron into the core. The effective quantum number n^* often replaces the quantity $n-\delta$.

1.4.2 Two electron excitation

Rydberg series may be considered with the configuration [core]n′l′n″l″ where $n' \geq 3$ and constant for a given series. The n″l″ orbital holds the Rydberg electron belonging to a Rydberg series $n'' = n', n'+1, n'+2 \ldots \infty$. In the series limit ($n'' = \infty$) the Rydberg electron becomes free, leaving a positive ion [core]n′l′. The quantum defects for this type of system show the screening effect of the excited n′l′ electron.

Rydberg series of great interest are those with n′=n″ throughout the series. In this case the excited electrons are highly correlated and in the series limit both excited electrons become free leaving a doubly charged ion.

1.5 The Franck-Condon Principle

An electronic transition may be accompanied by a change in the vibrational quantum number v. Although quantum mechanics imposes no restrictions on these changes, vibrational lines observed in photoelectron spectra do not all have the same intensity.

This phenomena is explicable in terms of the Franck-Condon principle which states that an electronic transition takes place so rapidly that a vibrating molecule does not change its internuclear distance appreciably during the transition. The intensity of the transition is thus determined by the magnitude of the overlap integral between the electronic wavefunctions of the two states involved.

The effect of the Franck-Condon principle on the spectra of transitions between states of varying internuclear separation can be seen in figure 1.5.

1.6 Light Sources

Obtaining suitable light sources has been a major problem for photoelectron spectroscopists. The majority of earlier experiments used the discrete wavelengths produced by the helium resonance lamp (mainly 584Å but occasionally others including 304Å). The neon and argon resonances have also been used but this restriction to just a few discrete wavelengths has hampered studies.

This is particularly true where resonant processes such as autoionisation are present, be it as the process under investigation or as a

Figure 1.5

The effect of the Franck-Condon principle for a) upper and lower states of equal internuclear separation, b) internuclear distance a little greater than that in the lower state, and c) upper state internuclear distance considerably greater.

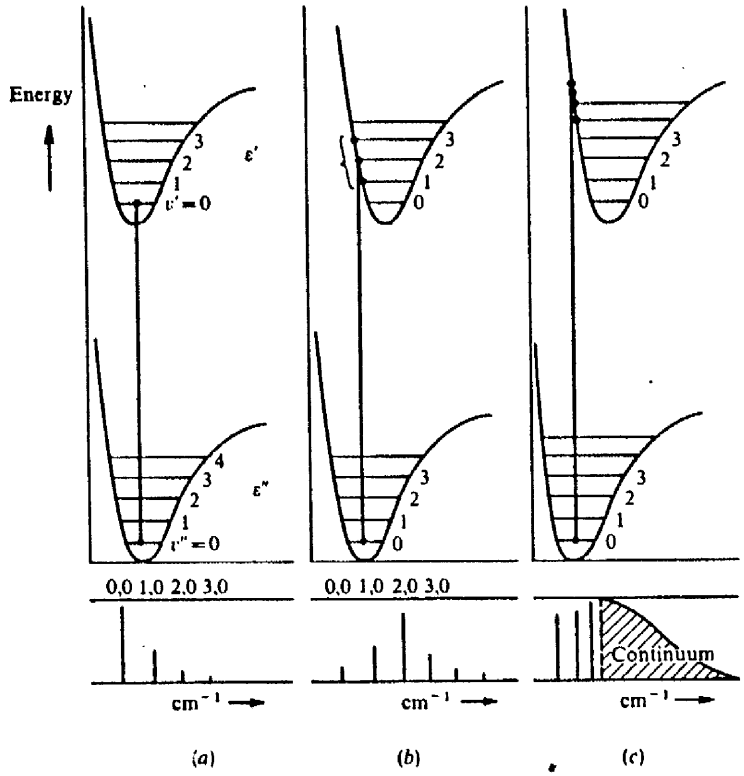

competing process to non-resonant photoionisation.

Attempts to overcome this restriction include that of Vilesov et al [4] using dispersed radiation from a windowed hydrogen lamp to examine the photoelectron spectra of organic molecules. The incident energy of this source suffered from an upper limit of 11eV due to the cut off of the LiF window. Blake and Carver [5] used the helium continuum to take photoelectron spectra of O_2, N_2 and H_2O but poor resolution left many states unresolved.

Various authors [6][7][8] have used the wavelengths of resonant autoionising states, previously determined from photoabsorption and photoionisation experiments, to perform subsequent photoelectron experiments. The low intensity of the helium continuum still only allowed observation of the most intense features with very long collection times, (several hours at each wavelength).

The advent of synchrotron radiation revolutionised photoelectron spectroscopy. These sources provide continuous radiation from infra-red to hard X-rays, which by monochromation can be tuned over the required energy range. Sufficient intensity and resolution have been obtained from existing monochromators to investigate many processes including those dependent on a variable wavelength.

Many of these experiments have also exploited the inherent polarisation of synchrotron radiation and investigated features as a function of wavelength, ejected electron energy and the angle of electron emission.

1.7 Angular distribution of photoelectrons

If the incident radiation is polarised, photoelectron intensity is a function of the direction of the ejected electron relative to the electric vector of the photons. In the dipole approximation, the yield of photoelectrons, $dN_i/d\Omega$, ejected into unit solid angle by plane-polarised radiation is given by

$$\frac{dN_i}{d\Omega} \propto \frac{\sigma_i}{4\pi}(1 + \beta P_2(Cos\theta))....1.3$$

where σ_i is the total cross-section for an ionisation channel i, $P_2(Cos\theta)$ is the second Legendre polynomial and β is the angular asymmetry parameter. The value of β depends on photon energy and can range from -1 to +2. The angular distribution of photoelectrons for four fixed values of β are shown in figure 1.7.

The second Legendre polynomial is given by

$$P_2(Cos\theta) = 3/2Cos^2\theta - 1/2....1.4$$

where θ is the angle between the ejected electron and the electric vector of the incident radiation.

Monochromated synchrotron radiation is partially (or elliptically) polarised. If the photon direction is given by the z-axis of a cartesian co-ordinate system, and I_x and I_y are the x and y components of the light intensity, the degree of polarisation is defined by;

$$P = \left|\frac{I_x - I_y}{I_x + I_y}\right|....1.5$$

Figure 1.7

Angular distribution of photoelectrons excited by plane polarised radiation for values of the asymmetry parameter β = -1, 0, +1 and +2.

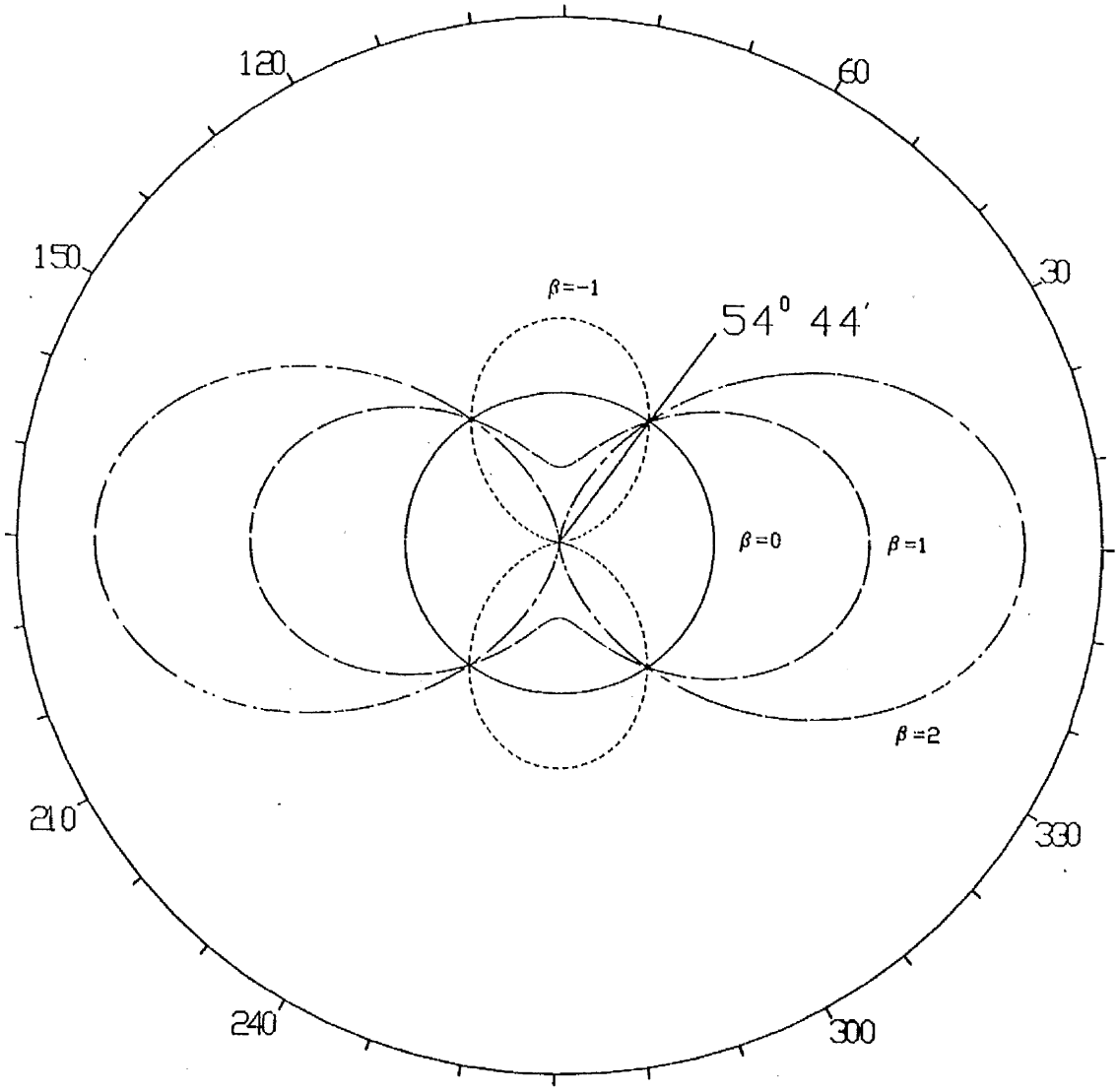

Representing the direction of the ejected photoelectron by the angles θ_x and θ_y with respect to the x and y axes, equation 1.3 now becomes;

$$\frac{dN_i}{d\Omega} \propto \frac{\sigma_i}{4\pi}\{1 + \frac{3}{4}\beta[(1+P)Cos^2\theta_x + (1-P)Cos^2\theta_y - \frac{2}{3}]\}....1.6$$

The x-axis is oriented parallel to the direction of maximum polarisation. If $\theta_x = \theta_y = 54°44'$ the part of this expression containing θ and P vanishes. Thus photoelectron measurements taken at this "magic angle" are independent of angular distribution effects. This has been shown for plane polarisation in figure 1.7, and is true for all values of P.

In the present experiment, the photoelectrons are collected in the x-y plane with $\theta_x = 90 - \theta_y$. Given this restriction the magic angle depends on the polarisation P and is only 54°44″ for P=1.

1.8 Alternative Spectroscopic Techniques

1.8.1 Photoabsorption Spectroscopy

The high resolution (<0.1Å) of this technique often enables numerous Rydberg series for simple molecules to be identified both above and below the first ionisation limit. Accurate series limits and configurations can be deduced from observed spacings and intensities.

1.8.2 Fluorescence Spectroscopy

Excited neutral or ionic states may decay radiatively. One such process is shown in figure 1.8 where the techniques of observation are indicated for each transition. The emitted photons can be observed by either of two basic

Figure 1.8

Schematic illustration of some of the complementary spectroscopic techniques.

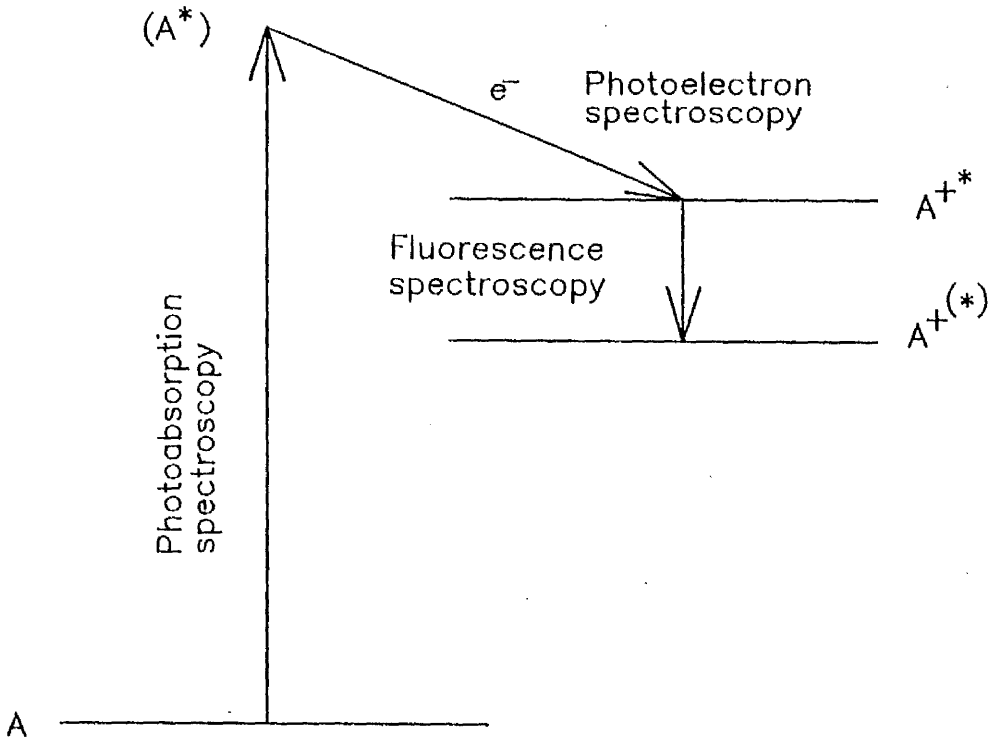

methods of fluorescence spectroscopy.

In the first method broad band VUV radiation is used to excite a large number of states which subsequently decay by fluorescent emission to a number of final states. In the second method the exciting source is monochromatic and tunable. Particular fluorescent transitions can thus be recorded as a function of excitation energy.

1.8.3 Optical Emission Spectroscopy

Optical transitions between ionic levels are observed at long wavelengths with this technique, allowing very high resolution. Optical emission spectroscopy can therefore generally reveal more ionic states than photoelectron spectroscopy and often provides data used in the assignment of ionic states observed in photoelectron spectra.

1.8.4 Electron Energy-Loss Spectroscopy

This technique closely resembles photoabsorption spectroscopy, with the advantage that the source, an electron beam, can easily be varied in energy continuously, with uniform intensity over a large range. The excitation energy of atomic and molecular states can then be obtained by measuring the difference in energy ("energy-loss") between the incident electron beam and electrons scattered inelastically from the target gas.

The resolution of electron energy loss spectroscopy is rather poorer than for photoabsorption spectroscopy, 15meV being particularly good. However, the main advantage of electron energy-loss experiments is found at

low impact energy and high scattering angle where the optical selection rules are relaxed and electric dipole forbidden transitions become relatively intense.

1.8.5 Ion-Yield Measurements

This technique involves the measurement of positive ion yield as a function of incident photon or electron beam energy. For atoms the results can be combined with photoabsorption measurements to investigate the relative popularity of photoionisation and radiative decay routes, ie photoionisation efficiency.

For molecules it is also possible that positive ions may result from dissociation. Mass analysis of the ions is therefore necessary before photoionisation efficiency can be determined, and this can provide complementary information for atomic autoionisation studies.

1.8.6 (e-2e) Spectroscopy

This technique, analogous to photoelectron spectroscopy, is often used to determine the energy levels of ionic molecular states. The source is an electron beam tuned over the required energy range. Pairs of electrons are then detected in coincidence. Each pair can be considered as one inelastically scattered electron, e_s, and one electron ejected during ionisation, e_i:

$$e + M \rightarrow M^+ + e_s + e_i$$

Observation of the coincidence rate measured as a function of

total electron collection energy provides binding energy spectra of the ionic states produced.

Simultaneous determination of the angular distribution of the scattered and ejected electrons yields extra information such as ion recoil momentum. Within the impulse approximation this is equal in magnitude and opposite in sign to the momentum of the ejected electron prior to ionisation [9]. This type of (e, 2e) work is sometimes called Binary (e, 2e) or Electron Momentum Spectroscopy.

(e, 2e) studies often provide the only available reference data for valence ionisation of molecules. Unfortunately this data suffers from low resolution due to the low count rate of coincidence measurements and vibrational levels are not resolved.

1.9 Conclusion

A brief review of photoelectron spectroscopy has been given above with an outline of specific areas of interest where it has become a powerful tool of investigation.

The main aim of this work is to provide highly resolved photoelectron spectra in the inner-valence photoionisation region of diatomic molecules. Improvements in sensitivity and resolution are important if further insight into electron correlation is to be gained from the observation of satellite lines (sect.1.2b). This type of study also allows the observation of atomic autoionisation processes which accompany the photoionisation spectra.

The present spectrometer has been designed and constructed

with particular attention to the resolution and sensitivity required. Principle features include a new type of electron detector, in the form of a large scale integrated chip, and the technique of 2D data collection used to observe processes of different energy dependence simultaneously.

The synchrotron, spectrometer and new detector are described in chapters 2,3 and 4 respectively. Chapter 5 shows the methods of data acquisition. A theory is presented in chapter 6 which uses electron correlation to help overcome the shortfall of the independent particle model in explaining the satellite spectra.

Results obtained for N_2, CO and HCl are presented in chapters 7, 8 and 9 where the theory of atomic autoionisation is presented with the use of specific examples. Previous experimental observations, together with calculations made by several authors from the theory of chapter 6, have been compared to the results in the relevant chapters.

CHAPTER TWO

THE SYNCHROTRON

2.1 Introduction

The energy range, intensity and resolution of vacuum ultraviolet radiation required for this study has been provided by the Daresbury synchrotron radiation source (SRS). The design and performance of the SRS and the monochromators used are described below.

2.2 Synchrotron Radiation

An accelerating charged particle will emit radiation. A non-relativistic charged particle accelerating due to an enforced circular path will emit radiation in the characteristic dipole pattern shown in figure 2.1(a). At relativistic speeds the particle will emit radiation with a conical angular distribution, represented in figure 2.1(b). The half angle of the cone (0.26mrad for 2GeV electrons) is given by $1/\gamma$, where γ is the ratio of the orbiting particles energy to its rest mass energy. The central axis of the cone always lies along the instantaneous velocity vector of the particle.

Synchrotrons use this process to provide radiation continuous from infra-red to hard X-rays. Tuneable monochromators can then select an energy range of radiation unsurpassed by other sources. The resulting photon beam is generally accepted with a broader energy distribution than is possible with discharge line sources, but this allows much higher

Figure 2.1

The angular distributions of emitted intensity from a) a non-relativistic, and b) a relativistic charged particle in a circular orbit.

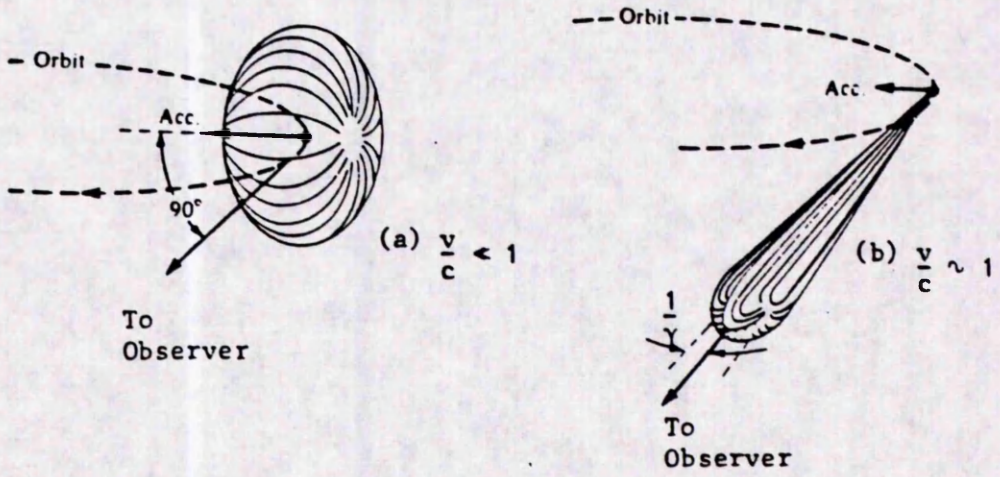

fluxes to be used.

Synchrotron radiation also exhibits strong polarisation, found to be 100% for emission in the orbital plane, decreasing slightly for radiation out of this plane. The electric vector lies in the orbital plane and perpendicular to the emission direction. This is important for photoelectron measurements where angular distributions are of interest.

2.3 The Daresbury Synchrotron Radiation Source (SRS)

The SRS consists of a linear accelerator, booster synchrotron and main storage ring which are shown schematically in figure 2.2. Electrons reaching 12MeV in the linear accelerator are injected into a booster synchrotron where they undergo further acceleration by a radio frequency (r.f) accelerator. At 600MeV the electrons are injected into the main storage ring where they reach their maximum energy, 2GeV, again using an r.f. accelerator.

A typical initial current of 200-250mA consists of 160 discrete electron bunches, contained in their orbit by 16 dipole magnets. The electron beam has a half life of approximately 12 hours, due mainly to scattering of electrons by residual background gas (pressure $\leq 10^{-9}$ torr).

2.4 Monochromators

Vacuum ultraviolet (VUV) radiation is strongly absorbed by all materials. Thus the most effective VUV optical systems employ mirrors and diffraction gratings used in reflection. The absorption of radiation, on reflection from a given surface, is a function of photon energy and the angle of incidence.

Figure 2.2

Schematic layout of the Daresbury Synchrotron Radiation Source.

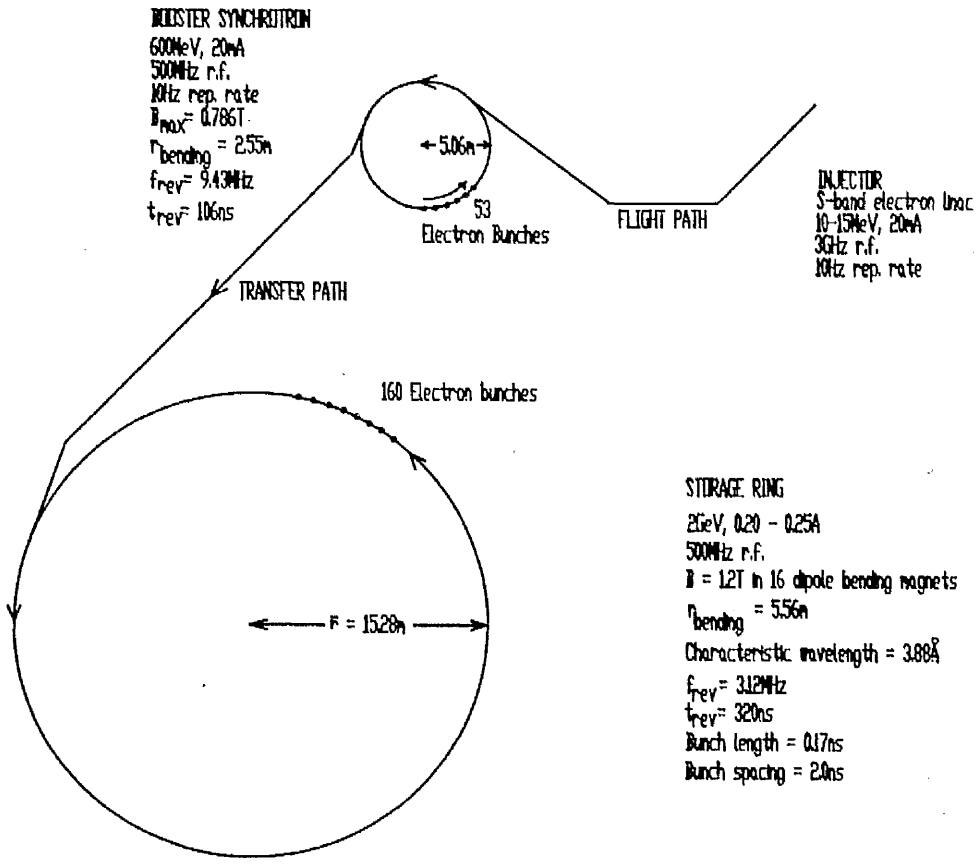

Absorption increases with photon energy and is highest for normal incidence. Optical instruments handling high energy photons therefore tend to use low (grazing) angles of incidence. Absorption also depends on the number density, n, of the reflecting surface, highest absorption occurring for materials with low n. Optical components are therefore coated with high number density materials such as gold or platinum.

At Daresbury there are two VUV monochromators which have been used for the present experiments. The first is of the normal incidence type, used for high resolution work in the range 17 - 28eV, while the second operates at grazing incidence and is used for studies requiring higher photon energies, 25 - 70eV.

2.4.1 McPherson 5m Normal Incidence Monochromator (NIM)

This monochromator, shown schematically in figure 2.3(a), employs a single grating with 1200 lines/mm and is used for high resolution (0.1 - 1.0Å) studies in the range 10 - 30eV (1200 - 400Å). The normal incidence design produces minimal optical abberations, a requirement for high resolution. The grating is designed to provide high photon fluxes but this is at the cost of the energy range over which the monochromator may operate. The performance of the grating used for the present experiments is shown in figure 2.4.

Figure 2.3

Schematic diagrams of a) the McPherson 5m normal incidence monochromator, and b) the toroidal grating monochromator.

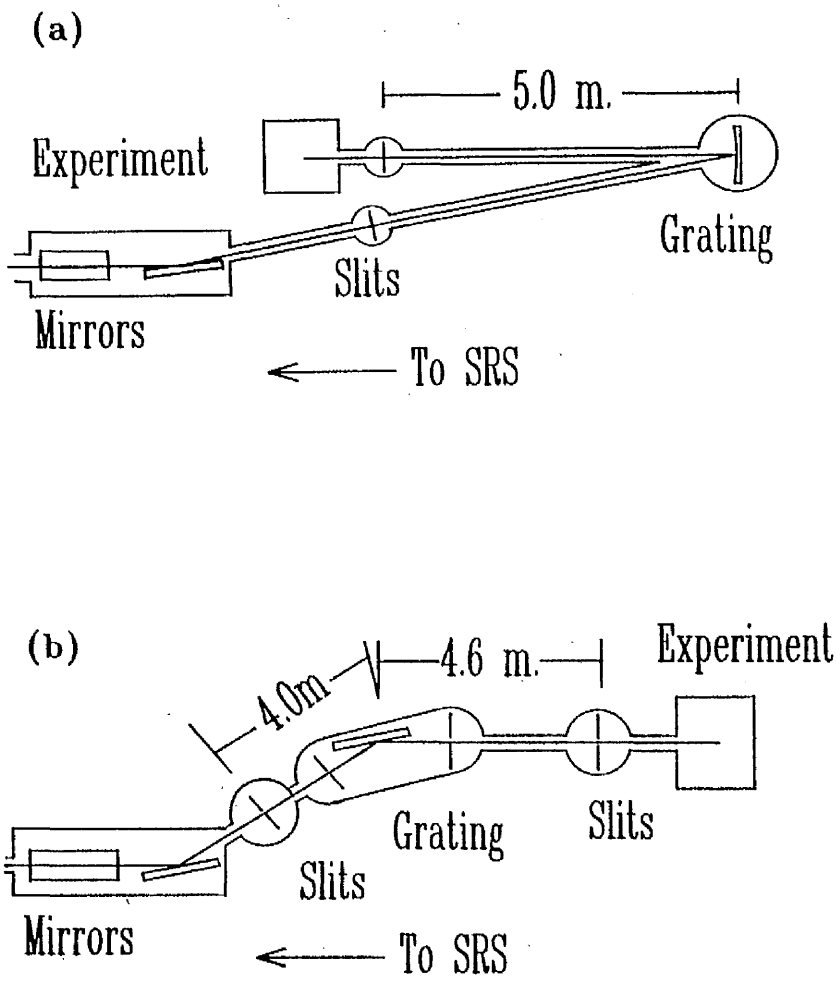

Figure 2.4

Light output from the McPherson 5m NIM. The measurements were obtained at the exit slit of the monochromator without a capillary light guide. There is therefore a reduction in intensity of about a factor of twenty at the target region of this experiment.

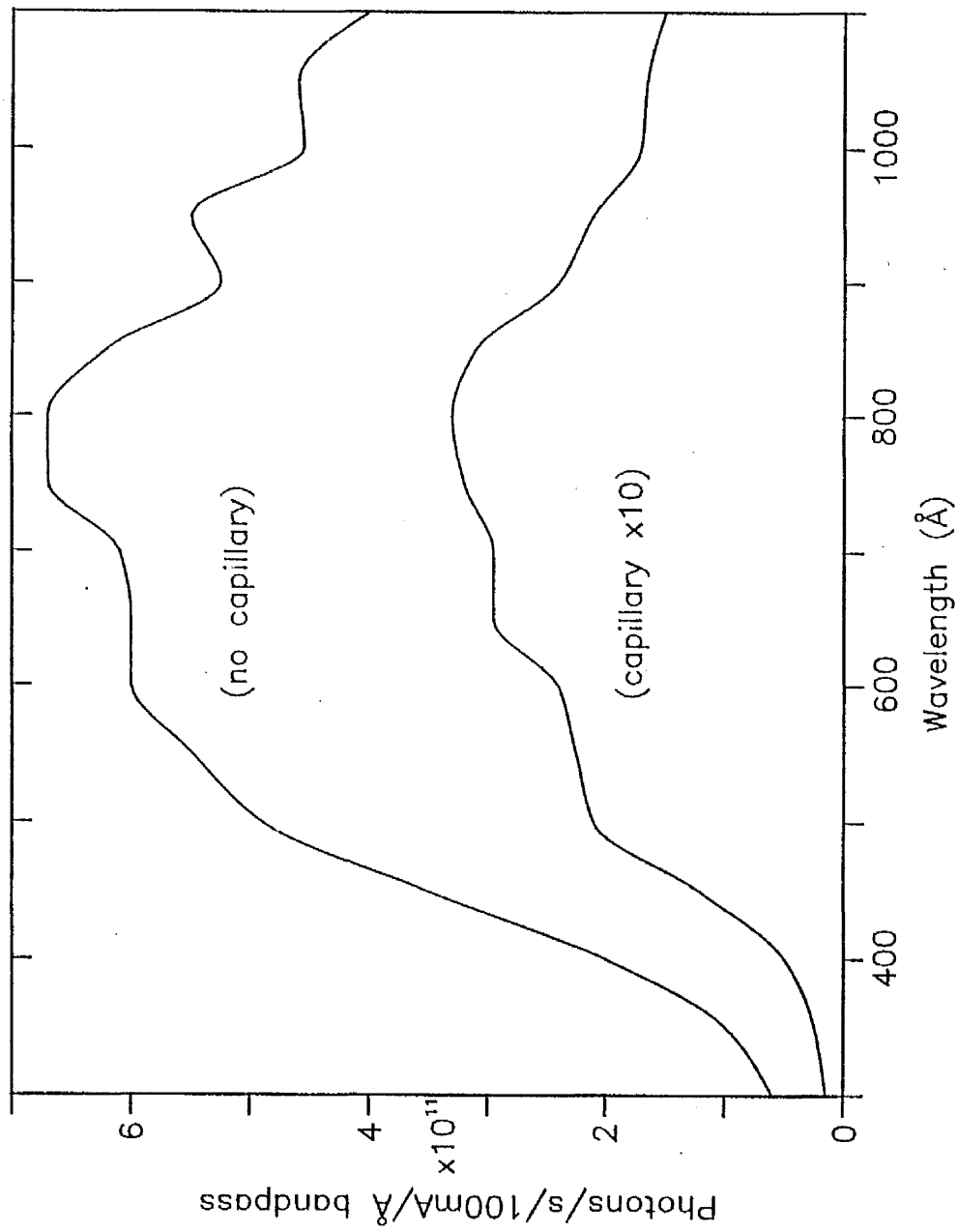

2.4.2 Toroidal Grating Monochromator(TGM)

The TGM is of the grazing incidence design and is shown schematically in figure 2.3(b). It covers the photon energy range 15 - 150eV (800 - 80Å), using two interchangeable gratings (710 and 2400 lines/mm), at a resolution of 50 - 100meV over this energy range. The performance of the gratings used for the present measurements is shown in figure 2.5.

2.5 Conclusion

The overall design and performance of the SRS, described above, creates the opportunity for advances in photoelectron spectroscopy. The effective use and control of this system with a photoelectron spectrometer will be described in chapter 5.

Figure 2.5

Light output from the two gratings of the TGM.

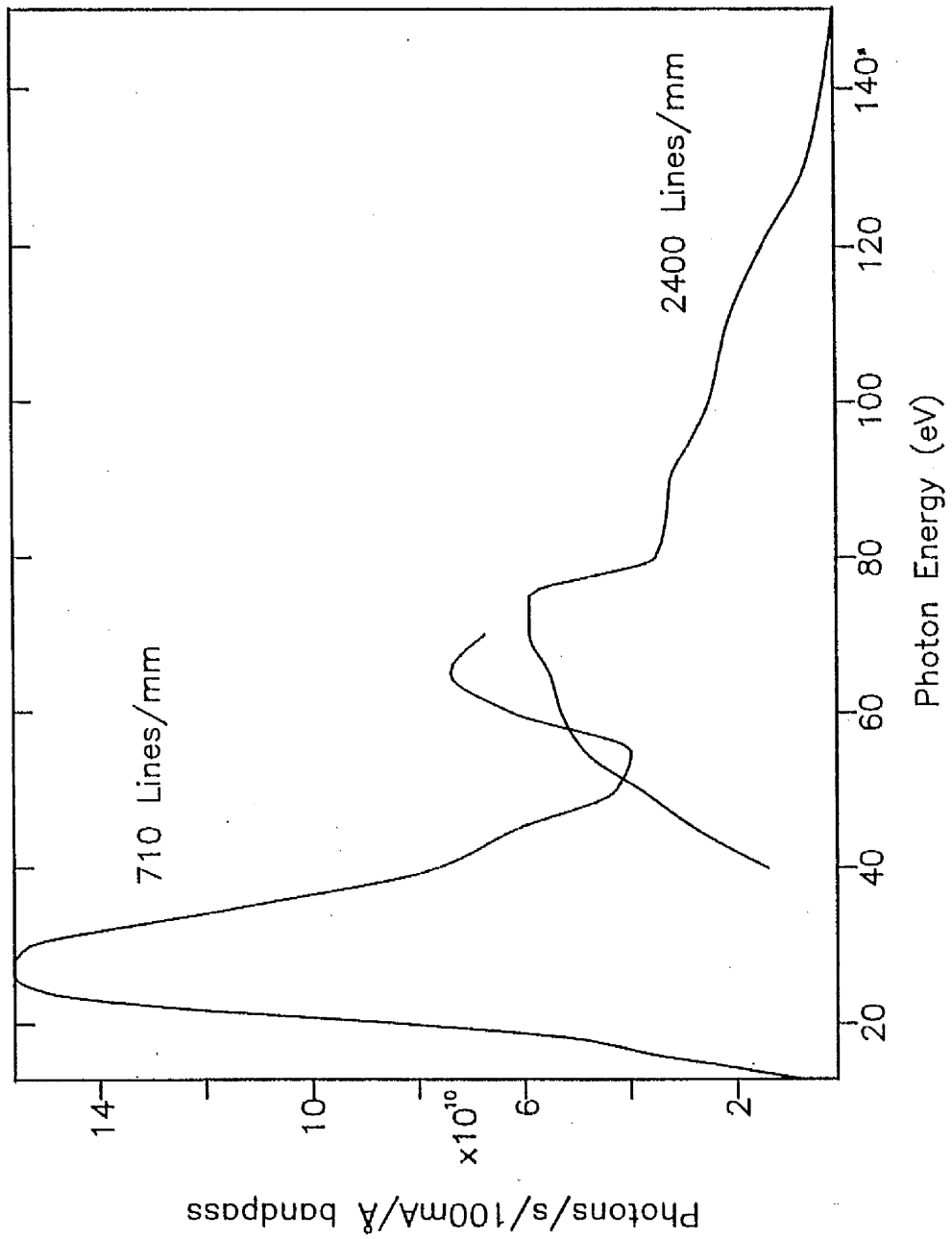

CHAPTER THREE

THE PHOTOELECTRON SPECTROMETER

3.1 Introduction

A schematic diagram of the photoelectron spectrometer is shown in figure 3.1. The photon beam enters the target region through a light guiding pyrex capillary, and is aligned at right angles to the flow of target gas from a hypodermic needle.

Ejected electrons from within a small solid angle are accepted by a three element lens and focused onto the entrance plane of a hemispherical energy analyser. A dispersed electron image is produced at the analyser exit, where position is a linear function of initial energy.

The intensity and positional information of this image is recorded by a new, one dimensional, position-sensitive detector.

3.2 The Target Region

The target region is enclosed in a metal housing to minimise stray electric fields in the interaction region. The end of the pyrex capillary is kept at the same potential as the housing by a copper shielding cap with electrical continuity to the hypodermic needle, figure 3.2(b).

Figure 3.1

Schematic diagram of the photoelectron spectrometer.

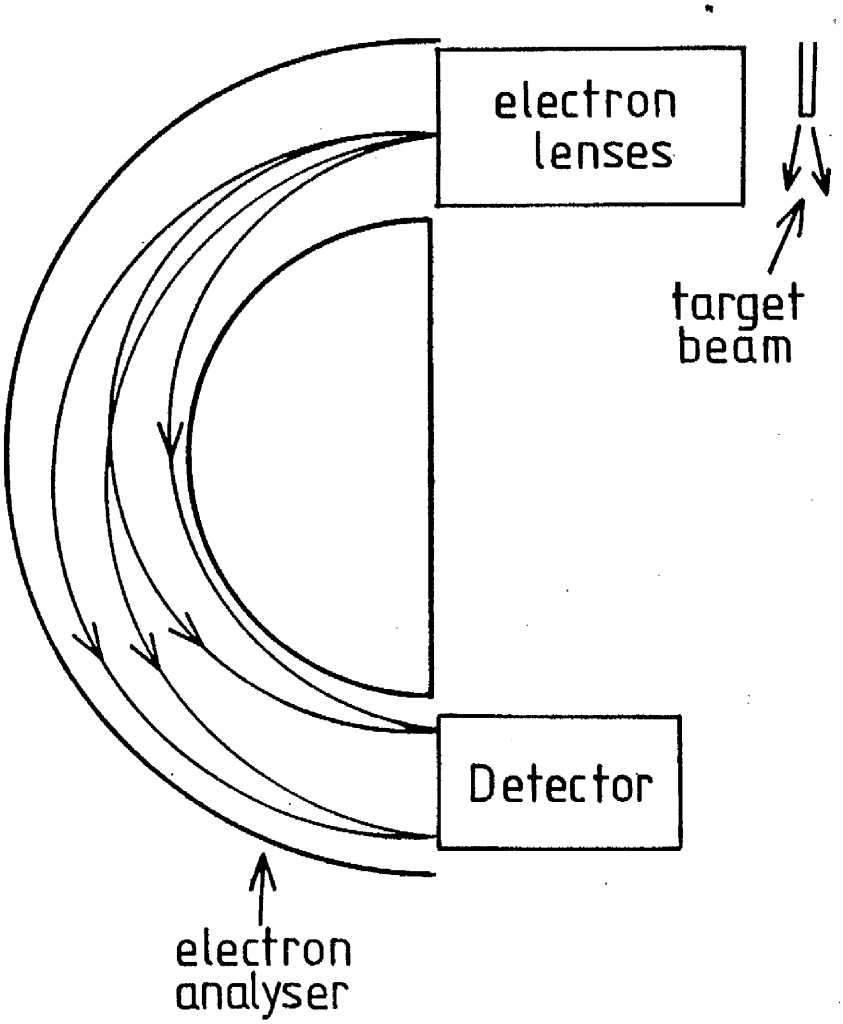

Figure 3.2

Schematic diagram of a) the orientation of the photon, gas and collected electron beams and b) the geometry of the capillary with respect to the needle.

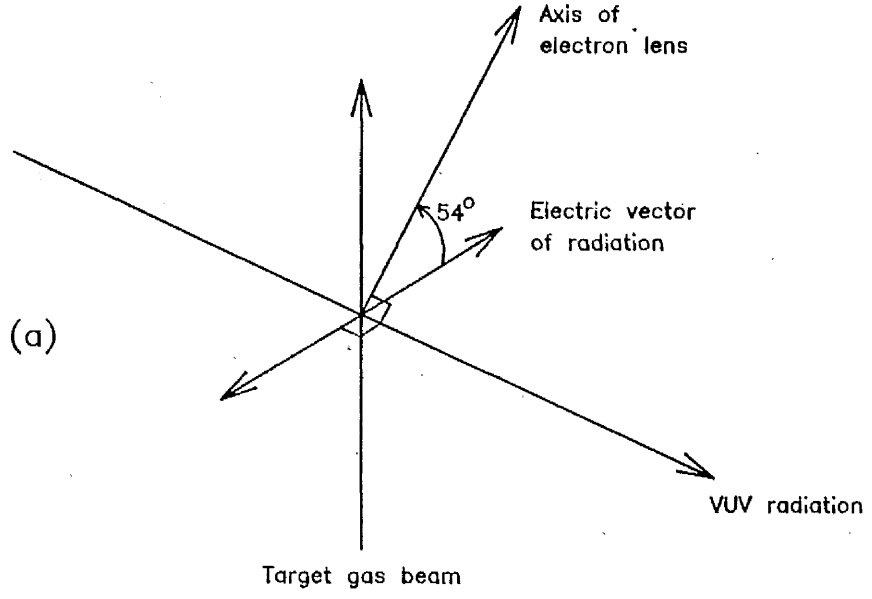

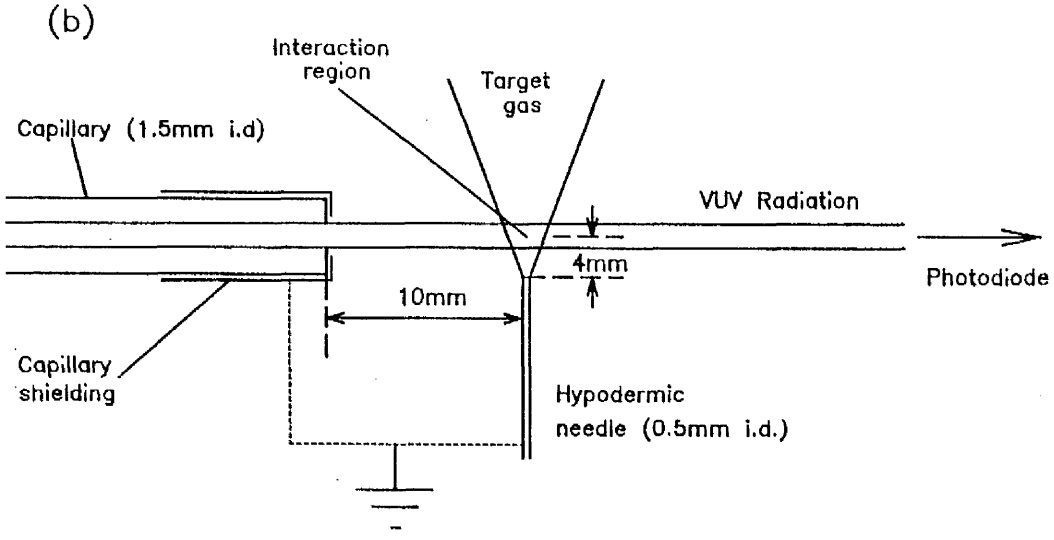

The photon beam, gas beam and electron optics have axes fixed relative to each other, shown schematically in figure 3.2(a).

The enclosure is pumped separately from the rest of the vacuum chamber. This allows the interaction region to be kept at a pressure typically 20 times greater than the main chamber. Photoelectron yield is correspondingly higher, while high voltages necessary for the detector can be used without damaging electrical discharges.

3.3 Electron Optics

The performance of the electron analyser depends on the pass energy, E_o. This is set to balance good resolution (low E_o) with high electron throughput (high E_o). The optimum pass energy can be employed for all photoelectrons by using the three element electron lens to accelerate/retard them.

The present lens design is shown in figure 3.3. This simple system was chosen since for varying electron collection energies the operating voltages do not vary rapidly. At low collection energies its operation is almost independent of electron energy.

With the hemispherical analyser set at the optimum pass energy, resolution depends mainly upon the size of the target image. This is governed predominately by the intersection of the gas beam with the photon beam, although it may be affected by stray fields.

Figure 3.3

Schematic diagram of the electron lens design.

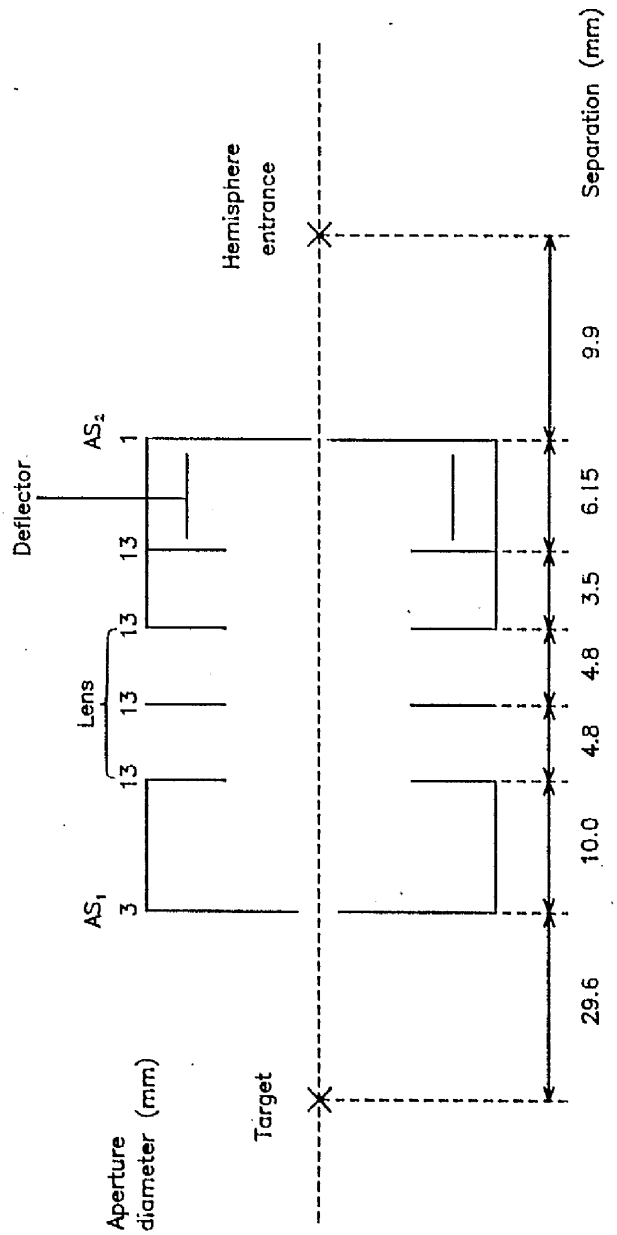

A limit on the image size accepted through the lens may be imposed by a low solid angle of acceptance. Angle stops AS_1 and AS_2 before and after the lens determine the angular acceptance over a wide range of collection energies (0.25 - 50eV). As the energy increases first AS_1 then AS_2 define the angle.

The variation of acceptance angle with energy is governed by the Helmholtz-Lagrange equation

$$r \sin\theta \, E^{1/2} = constant \quad ....3.1$$

where r is object radius, θ is the acceptance angle and E is electron energy. Hence it can be seen that electrons passing from a region of high potential to much lower potential across a given lens, will be subject to a large increase in angle Θ, bringing the second angle stop into action.

An advantage exists for multiple lens systems where extra apertures can better define angular acceptance,and therefore improve resolution.

Misalignments in the x-y position of the electron beam entering the analyser are rectified by a set of deflectors. Two pairs of orthogonal plates are electrically biassed symmetrically above and below the potential of the field free region in which they sit. Thus a force is exerted on the electrons, perpendicular to their motion.

As the electron collection energy decreases, difficult focusing is experienced followed by a cut off in transmission through the lens. This occurs due to surface potential variations becoming an increasing fraction of electron

energy, typically in the region 0.25-0.4eV.

3.4 Electron Energy Analyser

The electron energy analyser uses two concentric hemispherical deflectors, shown schematically in figure 3.4. Potentials applied to the hemispheres create an electric field between them that deflects and refocusses electrons with pass energy E_o, onto the centre of the analyser exit plane.

The pass energy of the analyser, E_o, is given by

$$E_o = \frac{e\,(V_2 - V_1)}{\left(\frac{R_2}{R_1} - \frac{R_1}{R_2}\right)} \quad \ldots . 3.2$$

where V_1 and V_2 are the voltages applied to the inner and outer hemispheres respectively. Electrons with energy $E > E_o$ are refocussed onto the exit plane closer to the outer hemisphere, while electrons with energy $E < E_o$ are refocussed closer to the inner hemisphere. For this type of analyser the dispersed image at the exit plane is linear in electron energy.

The full width at half maximum of the energy distribution of a hemispherical analyser is given by, [10],

$$\frac{\Delta E_{1/2}}{E_o} = \frac{1.7 r_a}{2R_o} + \frac{\alpha^2}{4} \quad \ldots . 3.3$$

Figure 3.4

Schematic diagram of the electron energy analyser. The annular hoops and resistive plates used to correct the electric field at the edge of the hemispheres are shown along with the path of electrons with energy E_o (pass energy), $E_o + \Delta E$ and $E_o - \Delta E$.

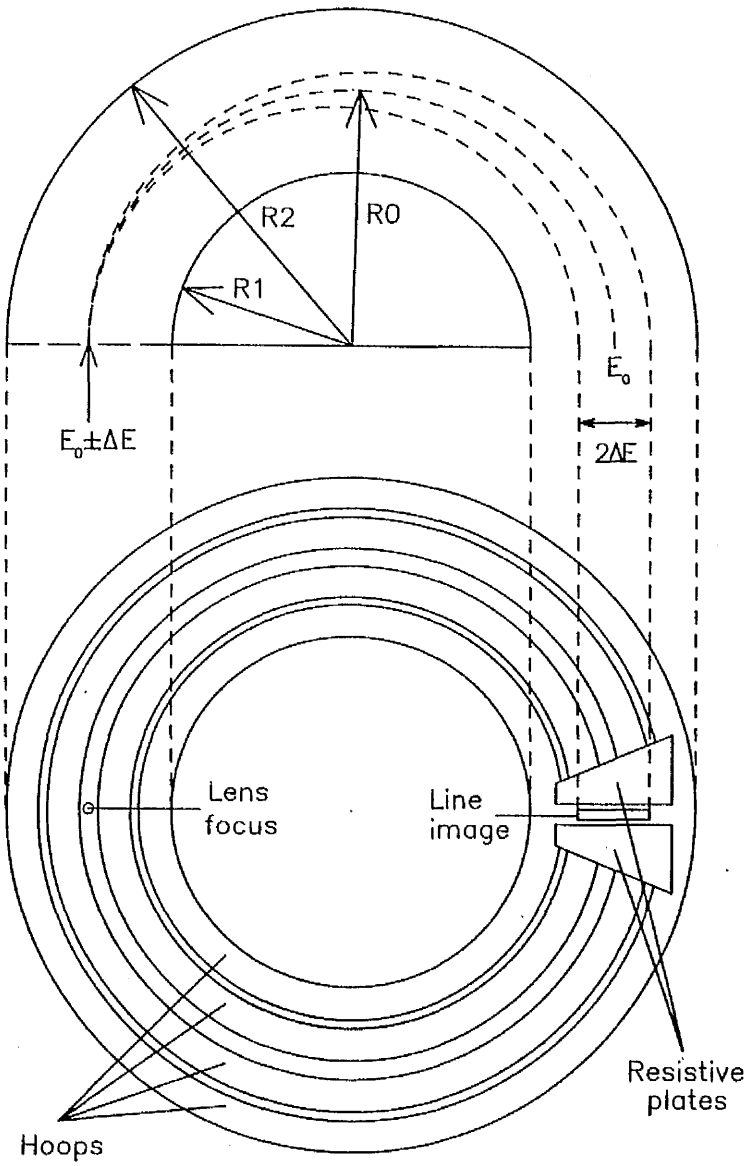

where α is the half angle of the beam at the entrance and r_a is the beam radius. The specifications of the analyser in the present spectrometer are given in table 3.4.

3.4.1 Field Edge Correction

For the electron energy analyser to perform as desired, the $1/r^2$ electric field created by the deflector potentials must exist where the deflectors end. To ensure termination of the potentials does not significantly perturb the electric field in this region, four annular hoops define discrete potentials around the gap between the hemisphere edges as shown in figure 3.4.

At the analyser exit, where a more precise field correction is required, the hoops are replaced by resistive plates. The plates used are made of a graphite coated ceramic sheet and are shaped so as to provide a smooth and continuous $1/r^2$ variation of the electric field in this region.

The theoretical voltages applied to the hoops and resistive plates to produce a $1/r^2$ field are given in table 3.4. These may be adjusted empirically to optimise the analyser performance.

3.5 Magnetic Fields

Local magnetic fields within the electron analyser will distort the linear image at the analyser exit. A set of external Helmholtz coils are used to cancel the vertical component of any dc fields, principally due to the Earth's magnetic field. The penetration of residual magnetic fields is reduced by a single layer of mu-metal within the vacuum

Table 3.4

Analyser specifications.

Image length = 20mm

Image width = 0.5mm

$$\frac{\text{Resolution}}{\text{Pass energy}} \propto \frac{1}{300}$$

	Mean radius (mm)	Theoretical voltage (V)
Inner hemisphere (R1)	64.5	19.5
Hoop 1	76.2	15.0
Hoop 2	89.0	11.4
hemisphere mid-point (R0)	95.2	10.0
Hoop 3	101.6	8.8
Hoop 4	114.3	6.7
Outer hemisphere (R2)	127.0	5.0
Resistive plates (inner)		13.0
Resistive plates (outer)		8.0

chamber.

3.6 Conclusion

The performance of the photoelectron spectrometer described above can be seen in the results of this study. The control of the spectrometer voltages is described in chapter 5. The detection of the energy analysed electrons produced will be described in the following chapter.

CHAPTER FOUR

POSITION SENSITIVE DETECTION

4.1 Introduction

Conventionally, the detection of low energy (typically <100eV) electrons following energy analysis involves projecting the image onto a narrow slit. A spectrum is accumulated by scanning the image across the slit, resolution being governed by slit width. To maintain a narrow passband with this system, a typical 1% of the available signal will be accepted through the slit at any instant. Clearly this is extremely inefficient in terms of sensitivity and data acquisition time.

Increasingly , position sensitive detectors (PSD's) are being used to utilise a much greater proportion of the dispersed image at the analyser exit. The growth of a variety of PSD's able to detect single low energy electrons and photons has been made possible by the development of multi-channel electron multipliers.

4.2 Microchannel Plate Electron Multipliers

Microchannel plates (MCP's) have been reviewed by Wiza [11], and more recently by Fraser [12].

The predecessor to the MCP is the channel electron multiplier (channeltron), a lead glass tube, about 1mm in diameter, with an internal resistive coating of high secondary emission coefficient. A potential difference

(typically 3kV) is applied between the ends of the tube, and a primary electron will collide with the walls of the channeltron on entry. A number of secondary electrons will be released from the wall to be accelerated down the tube, repeating the process in an avalanche effect, shown diagrammatically in figure 4.2.1. Eventually an output pulse of up to 10^8 electrons will result from the single electron event.

Most of the electrical properties of the channeltron are a function of the ratio of tube length to diameter, allowing an almost arbitrary scaling down. A complex manufacturing process whereby fine glass fibres are bunched, sliced and coated creates the 'honeycomb' wafer structure shown in figure 4.2.2. Millions of 10 - 25μm holes covering over 50% of the wafer act as individual channeltrons, making up the microchannel plate.

A potential difference of approximately 1kV is applied across the MCP to produce a typical gain of 10^4. A resistance of about $10^9\Omega$ between the faces of the MCP gives rise to a standing current of a few microamps, which replenishes electron emission. If the output current from the channel walls does not exceed 10% of this the gain will remain constant, otherwise saturation occurs. The resistivity of the plate also determines how quickly secondary emissions can be

replenished. This recovery time is effectively the dead time of the channels and is of the order of 10^{-2}s.

Positive ions, formed by ionisation of residual gases within the channels 'avalanche' region, can be accelerated back to the channel start where they produce unwanted additional pulses of secondary electrons. The effect of

Figure 4.2.1

Electron multiplication in a straight channel electron multiplier.

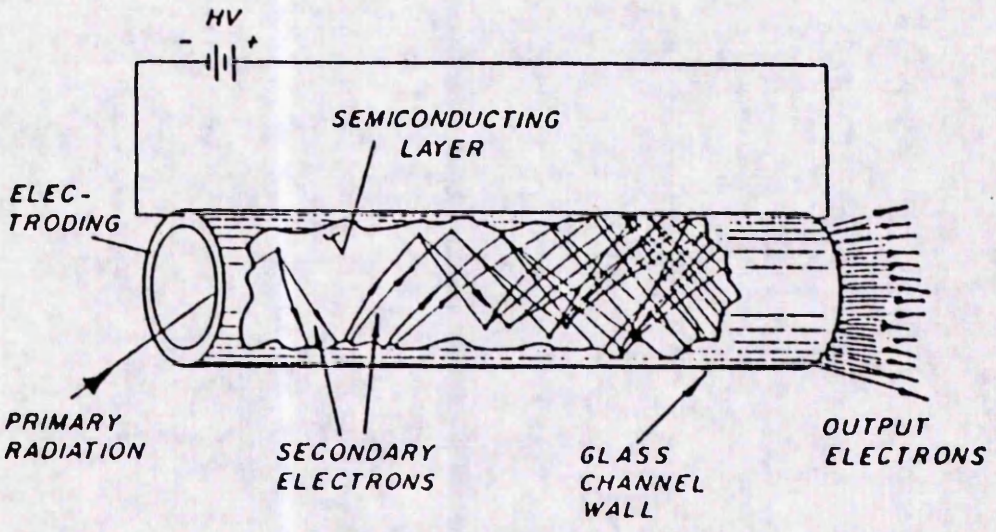

Figure 4.2.2

A microchannel plate electron multiplier.

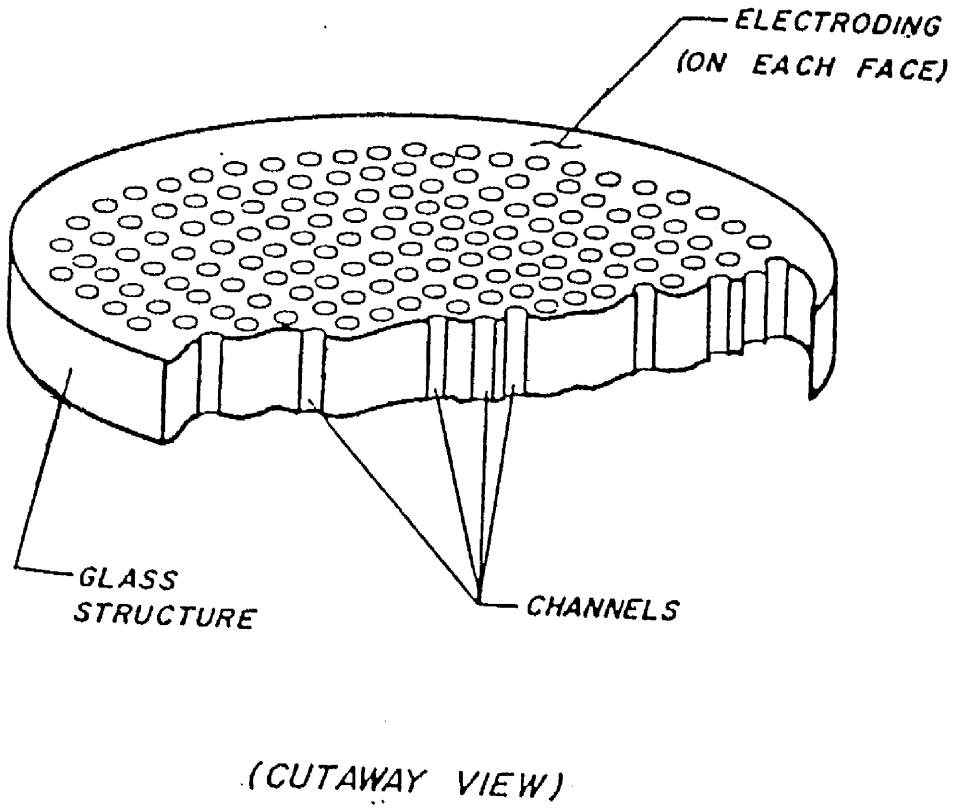

this 'ion-feedback' can be reduced by arranging two MCP's in chevron formation as shown in figure 4.2.3. This restricts feedback pulses to the gain of one plate only, by forcing returning ions into an early collision with the channel wall. Electron gain is at the same time increased to about 10^7, but spatial resolution is slightly reduced.

4.3 Review Of Position Sensitive Detection

Position sensitive detectors (PSD's) for low energy electrons and photons have been reviewed by Richter and Ho [13], and by Sigmund and Malina [14].

All PSD designs currently use microchannel plates (MCP's, cf sect.4.2) as an initial amplification stage, after which they fall into two main categories: (a) those which convert the electron output from the MCP into a light image for detection and (b) those which directly detect the electron image from the MCP.

4.3.1 Phosphor/Optoelectronic Image Detection

In this technique the electron output from the MCP is proximity focused onto a phosphor screen. The light image can then be projected by lenses or optical fibres to a position sensitive light detector, not necessarily within the vacuum system, see figure 4.3.1.

Phosphor Plate Viewed By Vidicon TV Camera

Vidicon TV cameras [15][16], use a silicon diode matrix to record the light image as an array of charge depleted areas. The extent of each diode's

Figure 4.2.3

Chevron operation of microchannel plates.

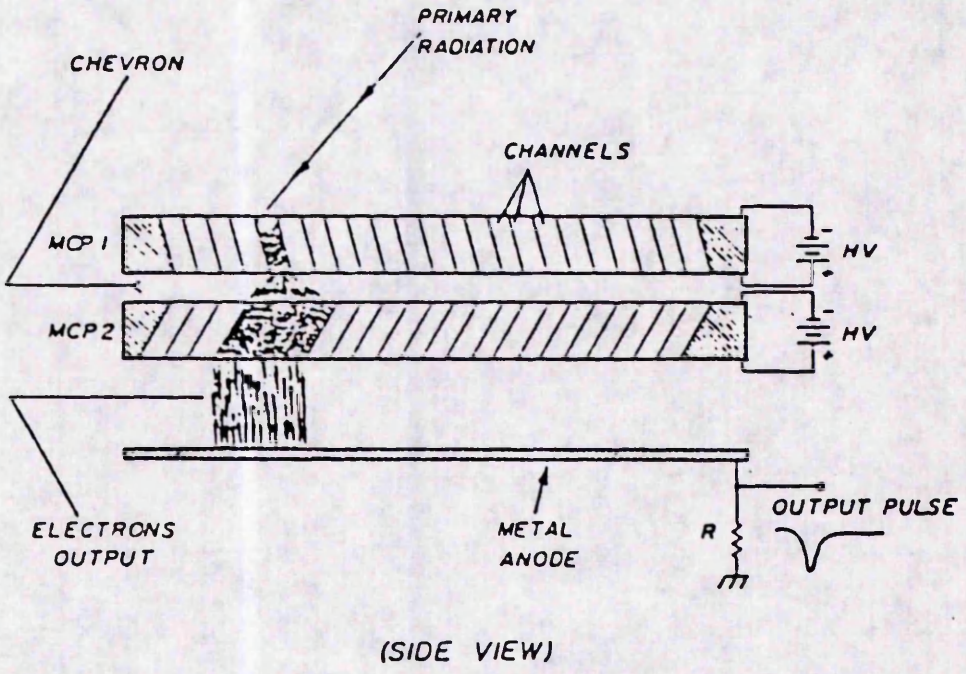

charge depletion is detected by measuring the replenishing current required by a scanning electron beam, figure 4.3.2.

This rather slow and bulky system is prone to a number of problems [17]. Distortion of the scanning electron beam causes image drifting and distortion. Leakage current on the diodes creates noise on the video output, and false images are formed when charging of interdiode silicon repels the replenishing beam, preventing complete diode recharging.

Self-Scanned Solid State Detector Arrays

The Vidicon camera can be replaced by either a self-scanned photodiode (SPD) array [18], or a charge coupled device (CCD) array [19][20]. Similarly to the Vidicon these solid state detectors record incident light as a change in the amount of charge held in depletion regions. Clock pulses are used to step the remaining charge packets sequentially onto a serial output to be amplified, digitised and stored.

SPD and CCD detectors are fast and have a small number of components, situated conveniently outside of the vacuum region. The fundamental disadvantage of all optoelectronic image detectors is that they are analogue. In regions of high local count rate, since the MCP gain is no longer linear, the change in stored charge on the detector surface is not directly proportional to the number of incident electrons.

It is, however, possible to operate both CCD's and SPD's in single electron counting mode. This is achieved by operating the channel plates and phosphor at a combined gain able to saturate a detector pixel with a single

Figure 4.3.1

General schematic of optoelectronic multidetector system.

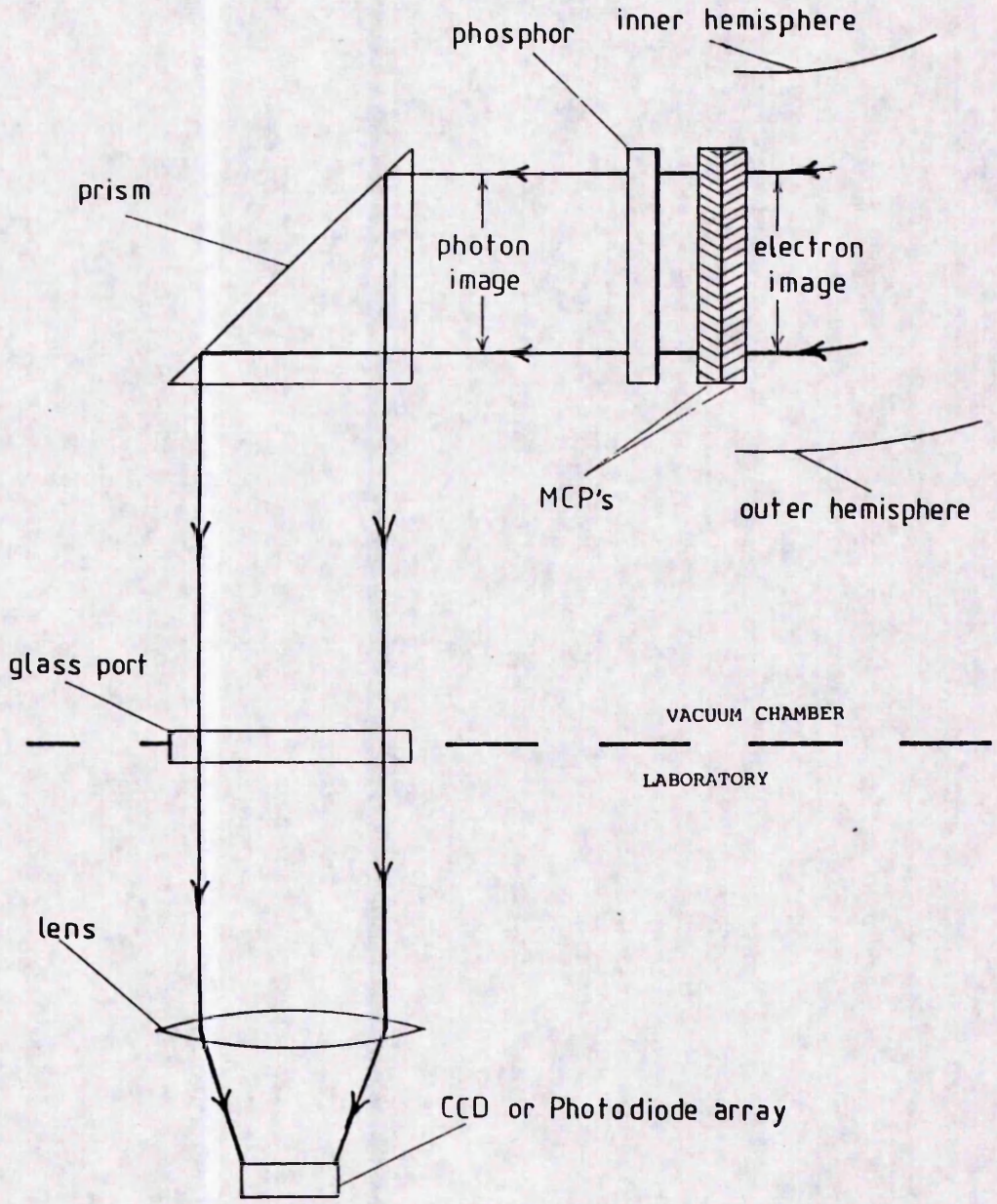

Figure 4.3.2

Vidicon tube using a silicon diode array.

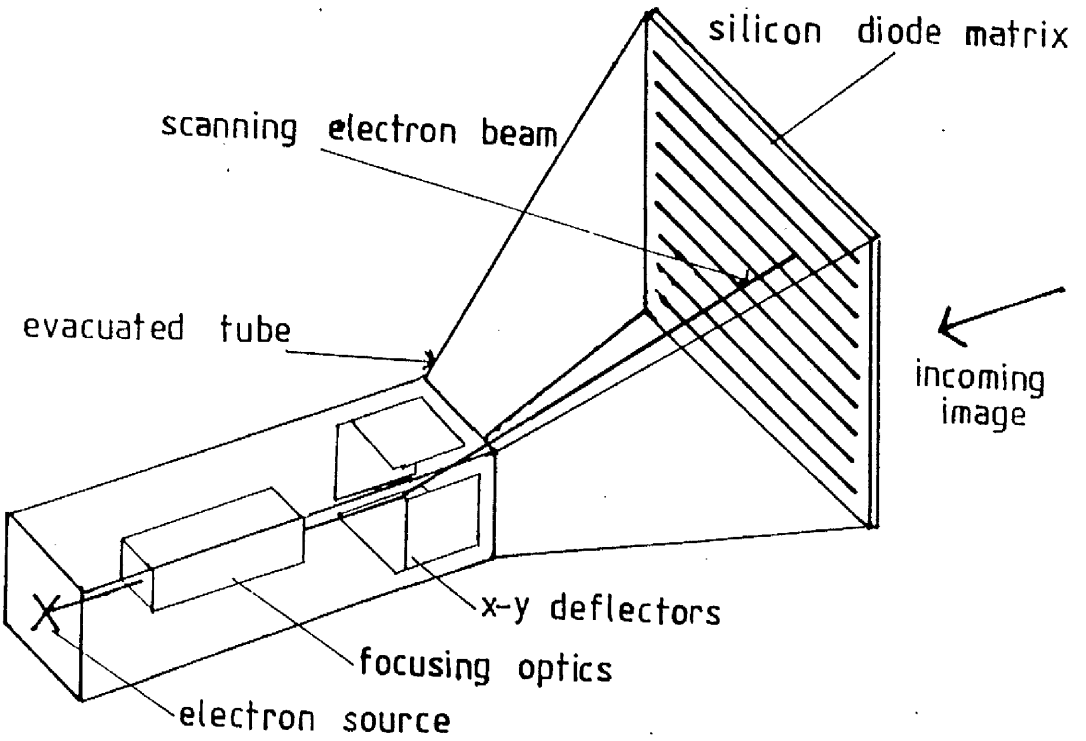

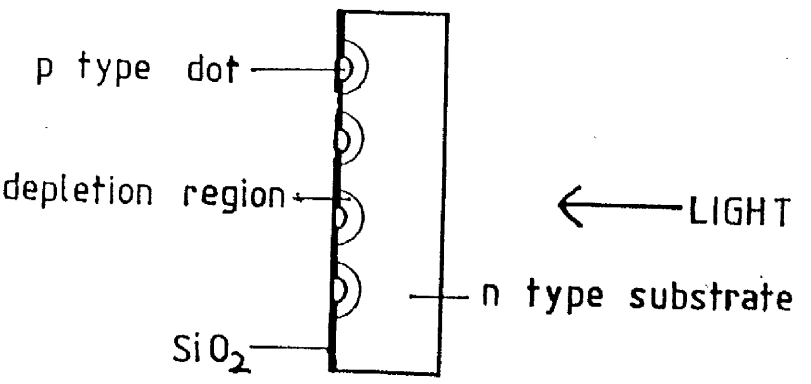

event. A simple discriminator then allows individual events to be pulse counted at the detector output. Unfortunately however, as it is not possible in this mode to accumulate data on chip, one is limited by the speed with which the array can be read.

4.3.2 Direct Detection Of Amplified Electron Image

Direct detection of the electron output from the MCP's has been achieved by a number of schemes. Ingenuity has often been shown in minimising the external component count. In general these detectors employ methods of *charge division*, or else use *multiple anodes*.

Charge Division

One of the most simple and successful techniques of position sensitive detection is the Resistive Anode Strip [21], figure 4.3.3. A continuous insulating strip having a high resistance (100KΩ) coating is positioned behind the MCP to accept electron pulses. Electronics at both ends of the strip measure differences in pulse amplitude or more commonly pulse development times (arrival times or pulse widths) to determine the position and size of the initial electron pulse.

Another charge division technique involves evenly spaced fine wires linked by equal capacitances [22][23], figure 4.3.4. Simplicity is again the main advantage, both techniques using only two amplifiers for a one dimensional detector. Simultaneous events cannot be detected by charge division and computational dead time limits the count rate. MCP gain reduction

Figure 4.3.3

Resistive strip detector.

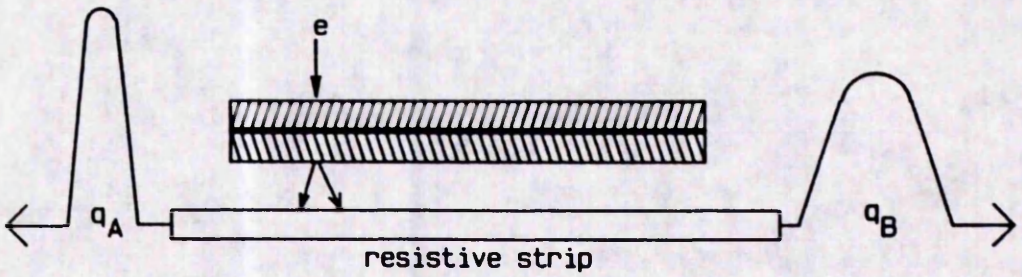

Figure 4.3.4

Schematic diagram of a capacitive network multidetector.

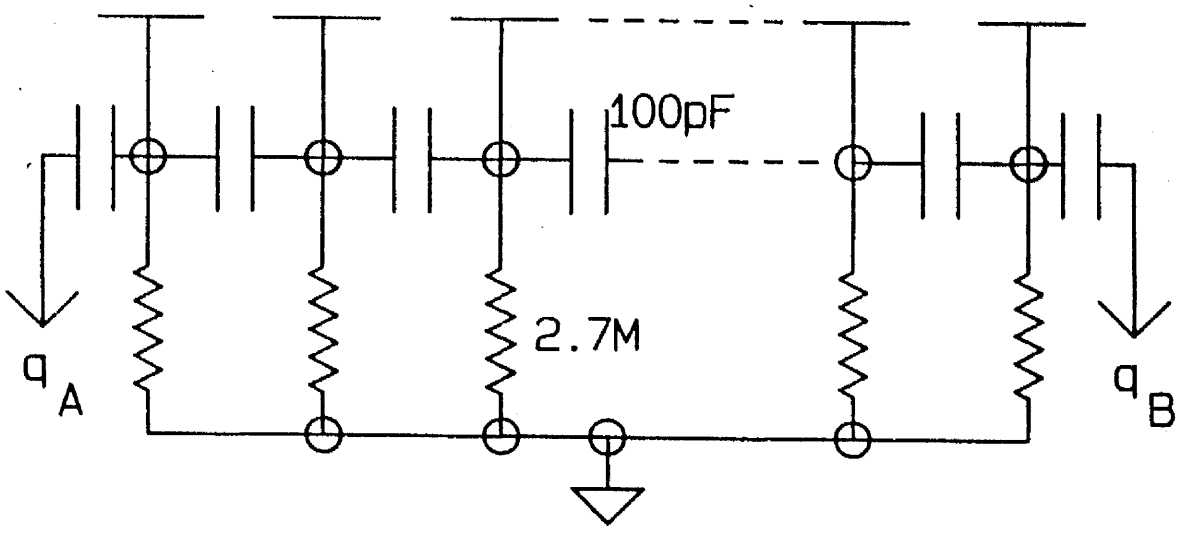

at high local count rate is also a potential problem.

Multiple Anode Detection Systems

These feature an array (1D or 2D) of metal anodes positioned near the output plane of the MCP's. Electrons collected on the anodes can be read out by a number of ingenious methods.

The Multi-anode Microchannel Plate Array (MAMA) [24], uses coincidence to decode n*m anodes with only n+m amplifiers. Anodes in different parts of the array are connected together in blocks allowing coarse and fine position encoding, figure 4.3.5. Finally, pulse amplitude analysis pin points arrival position.

The Coded Anode Converter (CODACON) [25], uses a coincidence array of anodes capacitively coupled to binary (Grey) code tracks, figure 4.3.6. The tracks register a different binary code for each anode, allowing n amplifiers to decode 2^n anodes.

The disadvantage of these read out systems is that they cannot detect simultaneous events in different parts of the detector. There is also a large dead time associated with the processing electronics, which limits the count rate across the array.

The most conceptually simple read out system has an array of electrically independent discrete anodes, figure 4.3.7. With each anode having its own amplifier, discriminator, and counting electronics, simultaneous events can be recorded at a rate limited only by the recovery time of the MCP's. Discrete anode systems [26][27][28], also feature excellent signal to noise ratio

Figure 4.3.5

Schematic diagram of a Multi-Anode Microchannel Array (MAMA).

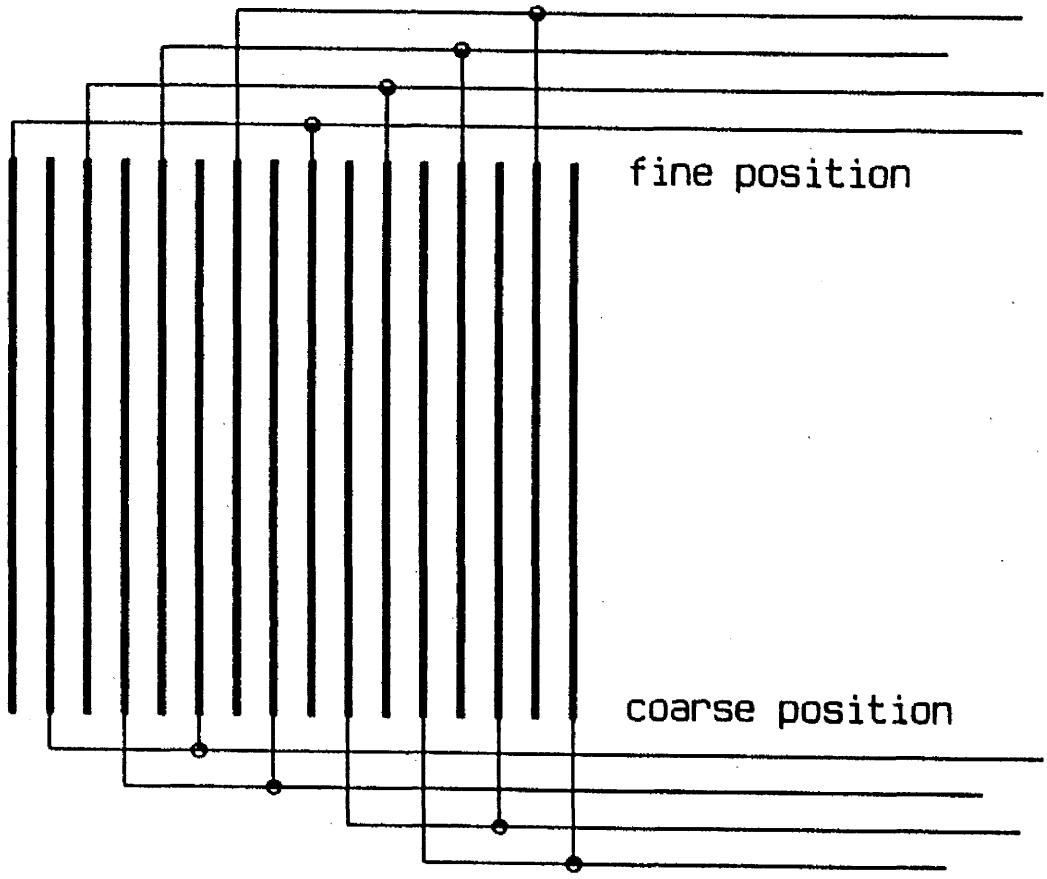

Figure 4.3.6

Schematic diagram of a coded anode converter (CODACON).

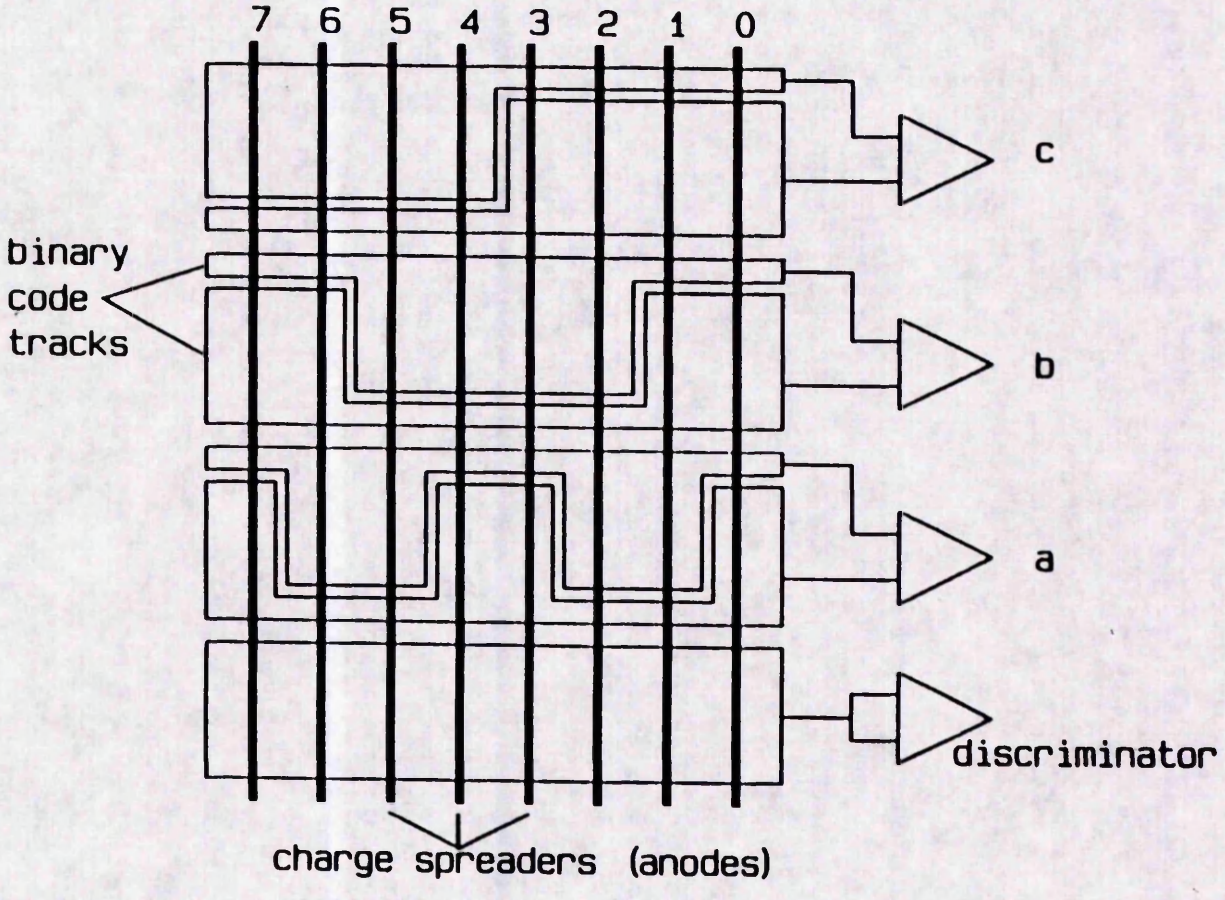

Figure 4.3.7

Schematic diagram of a discrete channel multidetector.

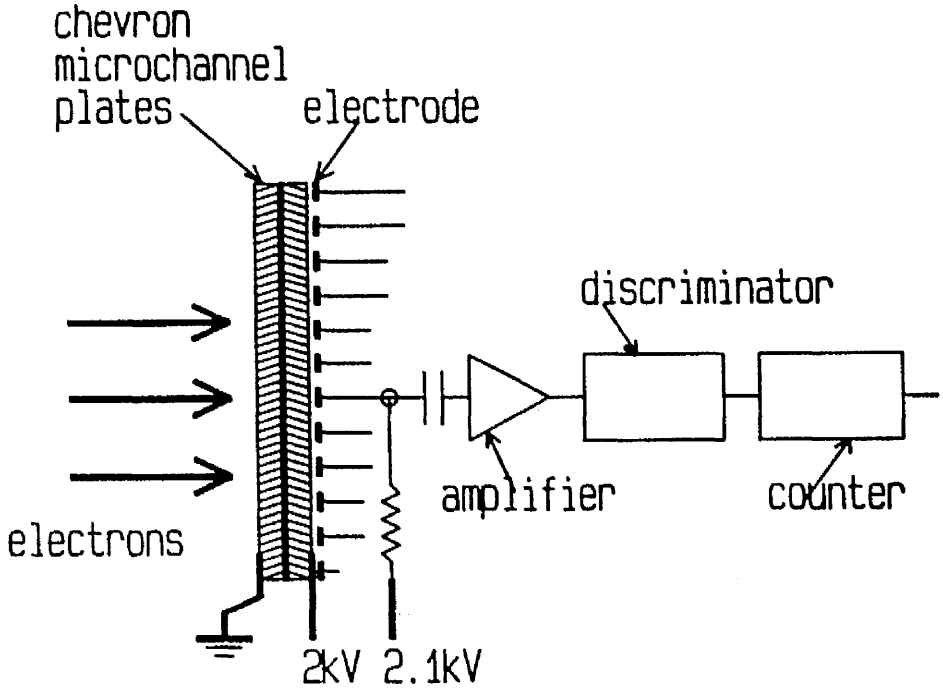

and, as fast pulse counters, are not effected by MCP gain reduction at high count rates.

Drawbacks associated with this simple scheme include a high external electronic component count. This is both unwieldy and prone to component failure. RF interference has also been a problem on bringing many small signals out of a vacuum enclosure. In practice, the factor most limiting the performance of discrete anode detectors has been found to be inter-channel cross-talk [26]. It would appear [26][28][29], that 2pF inter-channel capacitance is about the lowest
that can be achieved (including capacitance of
connectors, cables etc.), presenting only 80Ω impedance to 1ns pulses.

4.4 The Present Position Sensitive Detector

4.4.1 Introduction

The integrated circuit (IC) multidetector used in this study has been developed in Manchester by J.V.Hatfield, T.A.York and P.J.Hicks of the Department of Electrical Engineering at UMIST in co-operation with J.Comer of the Department of Physics at Manchester University [30]. Chip fabrication has been carried out at the Edinburgh Microfabrication Facility.

Although based on the discrete multiple anode concept, this detector overcomes the usually inherent disadvantages of this scheme, outlined in section 4.3.2. Integrating all necessary circuitry on a single chip, capped with the detecting electrodes, removes the need for a large amount of external processing electronics. With amplification and digitisation on chip, no small

signals are taken via long wires out of vacuum, eliminating RF interference. Cross-coupling also ceases to be a problem as inter-channel capacitance has become a very low, on chip, inter-electrode capacitance.

4.4.2 Electron Image Sensing Integrated Circuit

A single electron, leaving the analyser of the present spectrometer, initially undergoes amplification through a pair of microchannel plates (MCP's, cf sect. 4.2) mounted in chevron formation. A typical resultant pulse of 10^6 electrons over 1ns [14] is received by an array of electrodes. These are fabricated as an extra metallization layer on the surface of the chip, and placed in close proximity to the MCP output plane, figure 4.4.1.

The fundamental problem facing the development of the chip concerns the next stage, amplifying the incoming electron image. At first sight, amplification of a nanosecond pulse requires a bandwidth of the order of a gigahertz! Fortunately, the situation is made easier, given that to count pulses, only the presence or absence of charge has to be determined. This requirement is ideally fulfilled by a comparator with one input a discrimination potential. Thus a threshold level is set, above which a pulse is registered as having occurred by the generation of a logic level capable of driving a binary counter. This process effectively discriminates against noise, e.g. dark current in the MCP's. Furthermore, in the target instruments such as the present spectrometer, electron count rate is relatively low ($<10^6$ electrons/ cm^2 /second), offering a significant reduction in bandwidth. Thus the incoming charge can be integrated over one 'amplification' period and then

Figure 4.4.1

The Integrated Position Sensitive Detector.

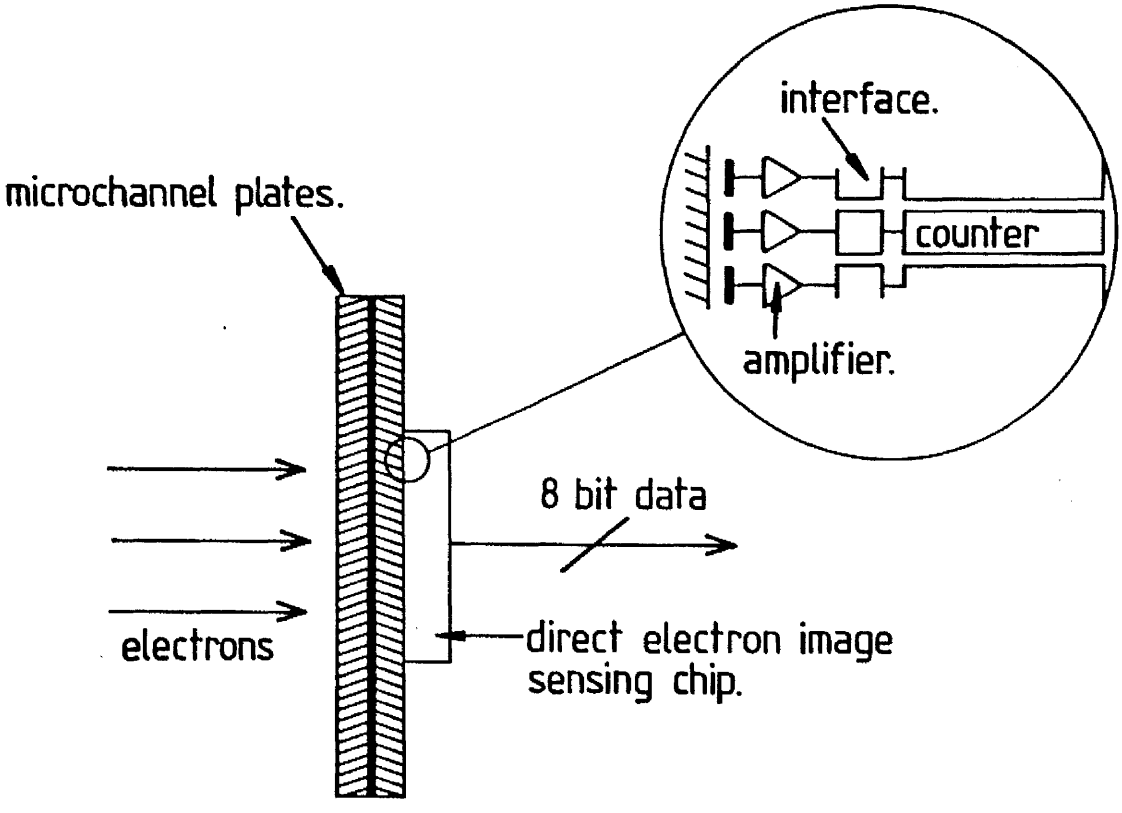

processed through the comparator during the next. The obvious drawback here is that two charge pulses impinging on a given electrode in the same sampling period, will be registered as a single event.

The architecture for the present IC is shown in figure 4.4.2. The best use of silicon area also simplifies the interconnect scheme by placing each channel of the device under its own electrode. Each electrode forms a direct vertical input by means of an interlayer via hole to a charge sensitive comparator. The comparator is interfaced in turn to an 8-bit counter, allowing single electron events to be recorded for up to 256 'sampling intervals'. Read out and clearing of the counters proceeds in a continuous self-scanning mode by means of a scanning shift register which multiplexes the output from the counters onto an 8-bit data bus. In the present application this allowed the detector to be interfaced for data acquisition to the same computer that controlled the experiment.

Further advantages due to the single event counting nature of this detector include good noise immunity, wide dynamic range and excellent linearity.

4.4.3 Electrode Input Structure

The detector used in this study has 32 electrodes of dimension 150μm x 2mm. A capacitance is created between the electrodes and the substrate below, and is given by

$$C_s = \frac{2.7\epsilon_r}{d} pF....4.1$$

Figure 4.4.2

The architecture of the new detector.

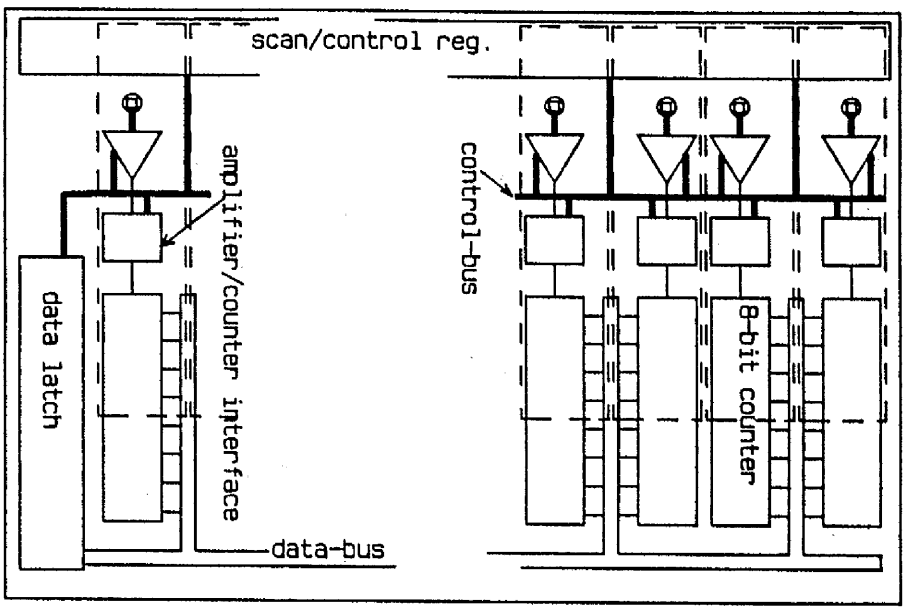

where ϵ_r is the dielectric constant and d the thickness, in microns, of the interlayer dielectric film.

Using conventional dielectric materials such as CVD[1] and plasma nitrides limits d to approximately 1μm and ϵ_r may be as high as 10, giving $C_s \approx 25$pF.

If 'n' electrons are captured by an electrode of capacitance to substrate C_s, its potential will fall by

$$V = \frac{1.6n}{C_s} \times 10^{-4}\, mV \ldots 4.2$$

For $n = 10^5$ and $C_s = 25$pF this is only 0.64mV.

In the present detector the situation has been made more favourable by using a spin on organic material, polyimide (PI) [31][32][33], for the interlayer dielectric. PI coatings have good planarisation properties, low dielectric constant ($\epsilon_r = 3.5$), and have been built up to a 7μm layer in this application. Electrode to substrate capacitance now becomes $C_s \approx 1.3$pF, giving rise to an easily detectable potential drop of 12mV on capturing a small pulse of 10^5 electrons.

4.4.4 Interelectrode Cross-Coupling

When n electrons are captured by an electrode of capacitance to substrate C_s (cf sect. 4.4.3), they lower its potential by V. Given an interelectrode capacitance of C_x, the potential of a neighbouring electrode is

[1] Chemical Vapour Deposition

lowered by

$$V' = V\frac{C_x}{(C_x + C_s)} \quad \text{....4.3}$$

Adjacent channels are therefore charge coupled by a factor

$$\frac{C_x}{C_x + C_s} \quad \text{....4.4}$$

which, for $C_s \gg C_x$, reduces to

$$\frac{C_x}{C_s} \quad \text{....4.5}$$

For conventional discrete multi-anode devices (cf sect. 4.3.2) such as that reported by Timothy and Bybee [26], $C_x \approx 2pF$ and $C_s \approx 30pF$ giving rise to some 7% charge coupling. Cascaded MCP's may be expected to produce charge pulses differing by two orders of magnitude, typically ranging from 10^5 to 10^7 electrons. With conventional detectors, strong signal pulses can therefore create cross-coupled pulses of the same magnitude as weak signal pulses, making discrimination impossible.

For an integrated circuit detector with the electrodes integrated onto the surface of the chip, inter-channel capacitance is the same as inter-electrode capacitance. In the present detector this has been limited to

$$C_x \approx 0.033pF.$$

With $C_s \approx 1.3pF$ this gives a value for C_x/C_s (eqn. 4.5) of approximately 0.025.

The calculated cross-coupling for the present detector is therefore

only 2.5%. A process of exposing alternate electrodes to signal, whilst masking the remainder,

has produced conclusive evidence that no significant cross-talk exists [30].

4.5 Conclusion

Progress made in position sensitive detection has been reviewed and the advantages of the system used in this study have been outlined. The ease of data acquisition with an integrated circuit detector of this type is described in the following chapter.

CHAPTER FIVE

EXPERIMENT CONTROL AND DATA ACQUISITION

5.1 Introduction

Overall control of the experiment is provided by a Zenith™ (80286) personal computer (PC). Experiment-computer interface is shown schematically in figure 5.1. Lengthy studies are defined by pre-set parameter files governing monochromator scanning and spectrometer voltages. Acquired data is displayed immediately for ongoing observation or tuning, and stored along with photodiode output.

5.2 Photon Energy

Scanning of the photon energy is achieved by stepping motors that drive the monochromator grating mounts. A module in the Camac crate moves the stepping motors and receives information on their position through an encoder. The PC is interfaced to the Camac module by a Rockwell™ 6522via[1] I/O board able to read encoder values and output required stepping motor movements.

An approximate calibration curve, relating encoder reading to photon energy, is incorporated within the PC software and provides the basis for the programme algorithm, figure 5.2. The final photon energy scale is more precisely calibrated on accurately known features in the spectra (sect.5.8).

---

[1] Versatile Interface Adapter

Figure 5.1

Schematic of experiment-computer interface.

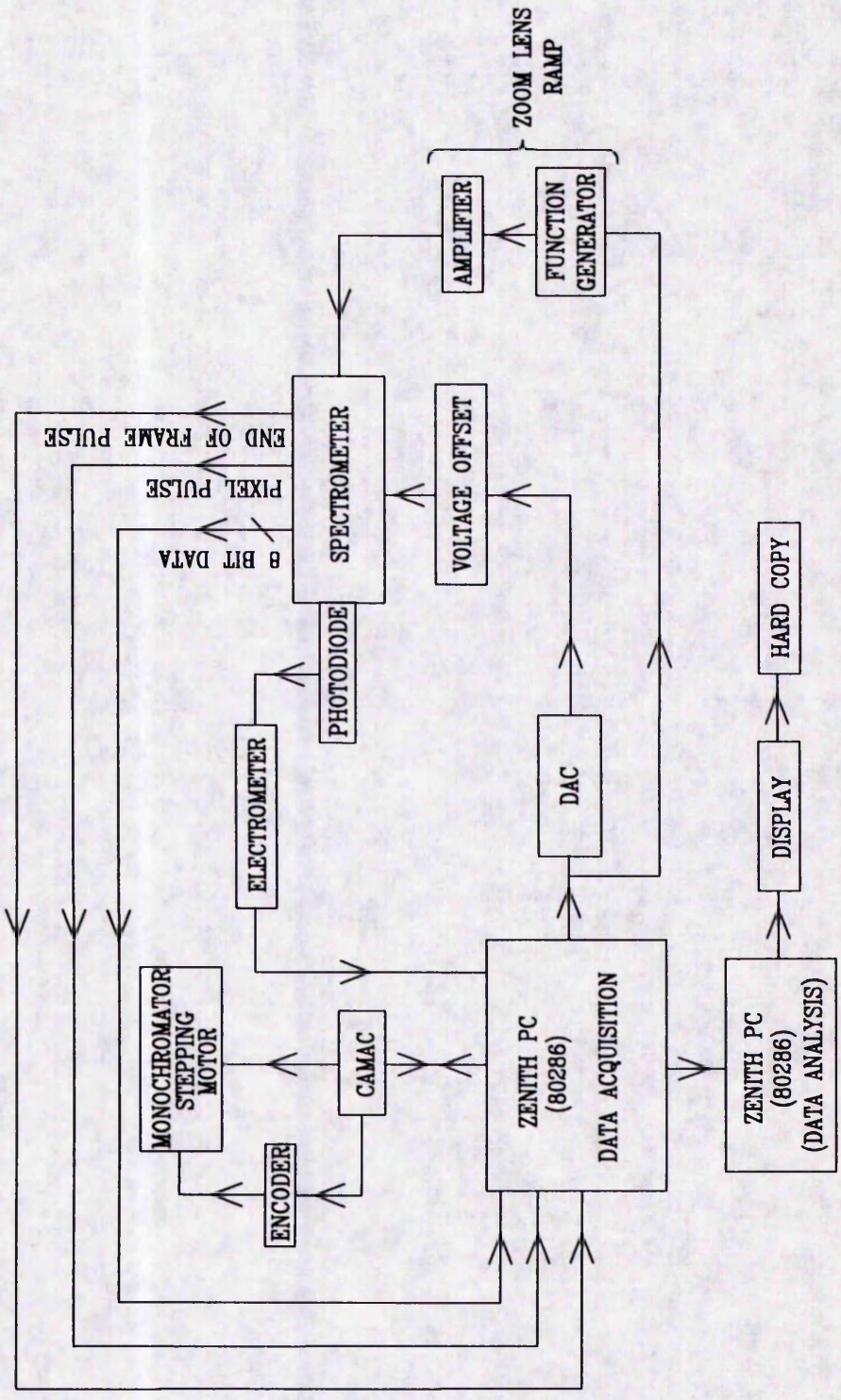

Figure 5.2

The steps followed by the computer software when changing photon energy.

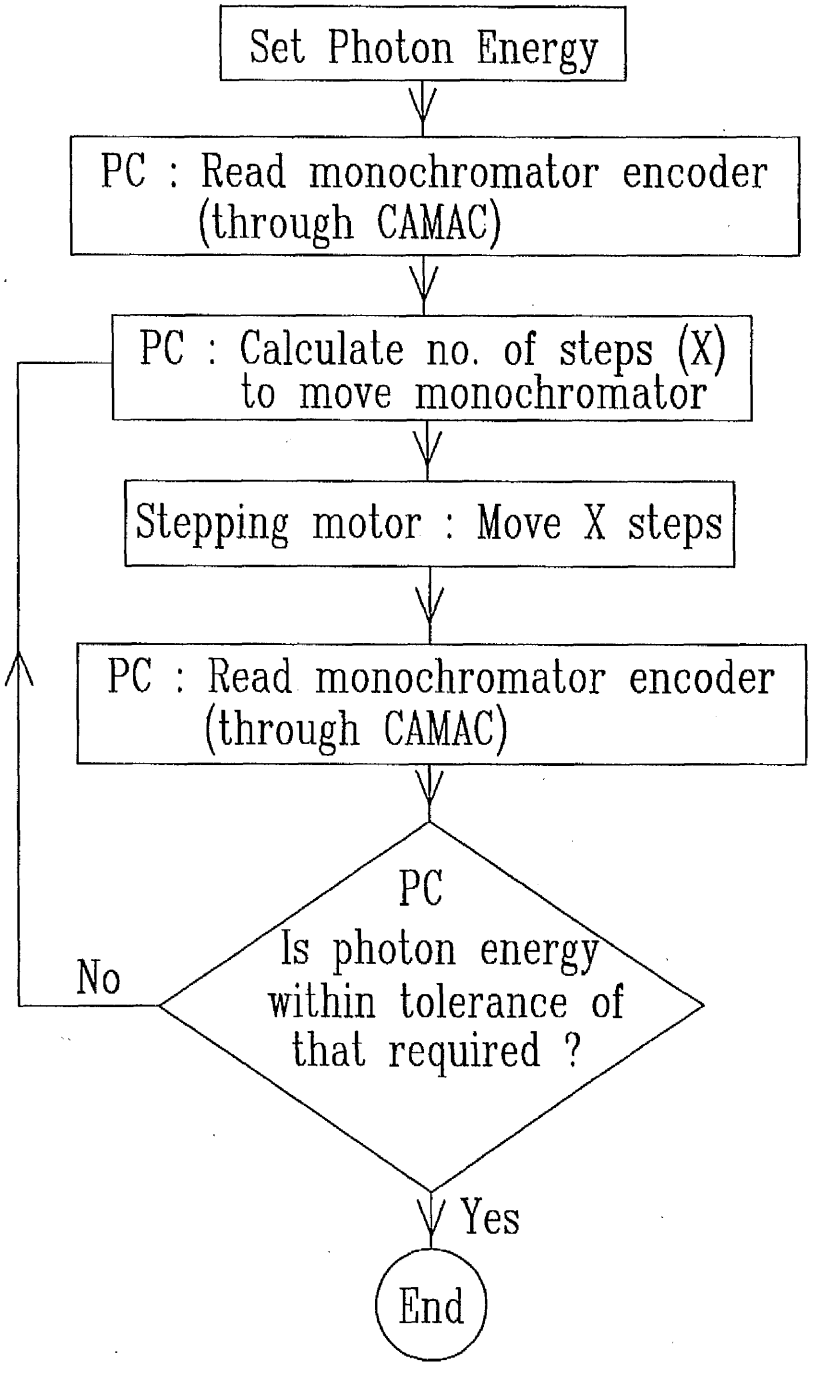

5.3 Spectrometer Voltages

The configuration of the power supplies used to set the potentials on the electron optical components, is shown schematically in figure 5.3. The potentials are defined relative to a virtual earth known as 'analyser earth', which represents the zero of electron kinetic energy. Collection energy is given by the difference between analyser earth and real earth (target region).

Scanning of electron collection energy is controlled by the PC via a 12 bit digital to analogue converter (DAC), figure 5.1. DAC output is amplified such that the collection energy can be stepped by an amount equal to the energy separation of adjacent channels on the detector. The significance of this is shown in section 5.6.1. The collection energy can thus be ramped in defined steps from 0 to 12 Volts.

5.3.1 Zoom Lens Function

With the first lens element set to a potential defined by the collection energy, and the third set by analyser pass energy, focus of the lens must be maintained by the central element potential. As collection energy is scanned, best focus can only be kept by changing the central potential. An electron lens operated in this way is often referred to as a 'zoom lens'.

The central element potentials required for best focus, over the possible range of collection energies, are found manually. At run time a function generator [34], referenced to the collection energy DAC (figure 5.1), reproduces the focus voltages from a pre-programmed fit.

Figure 5.3

Schematic of power supply configuration for electron optics.

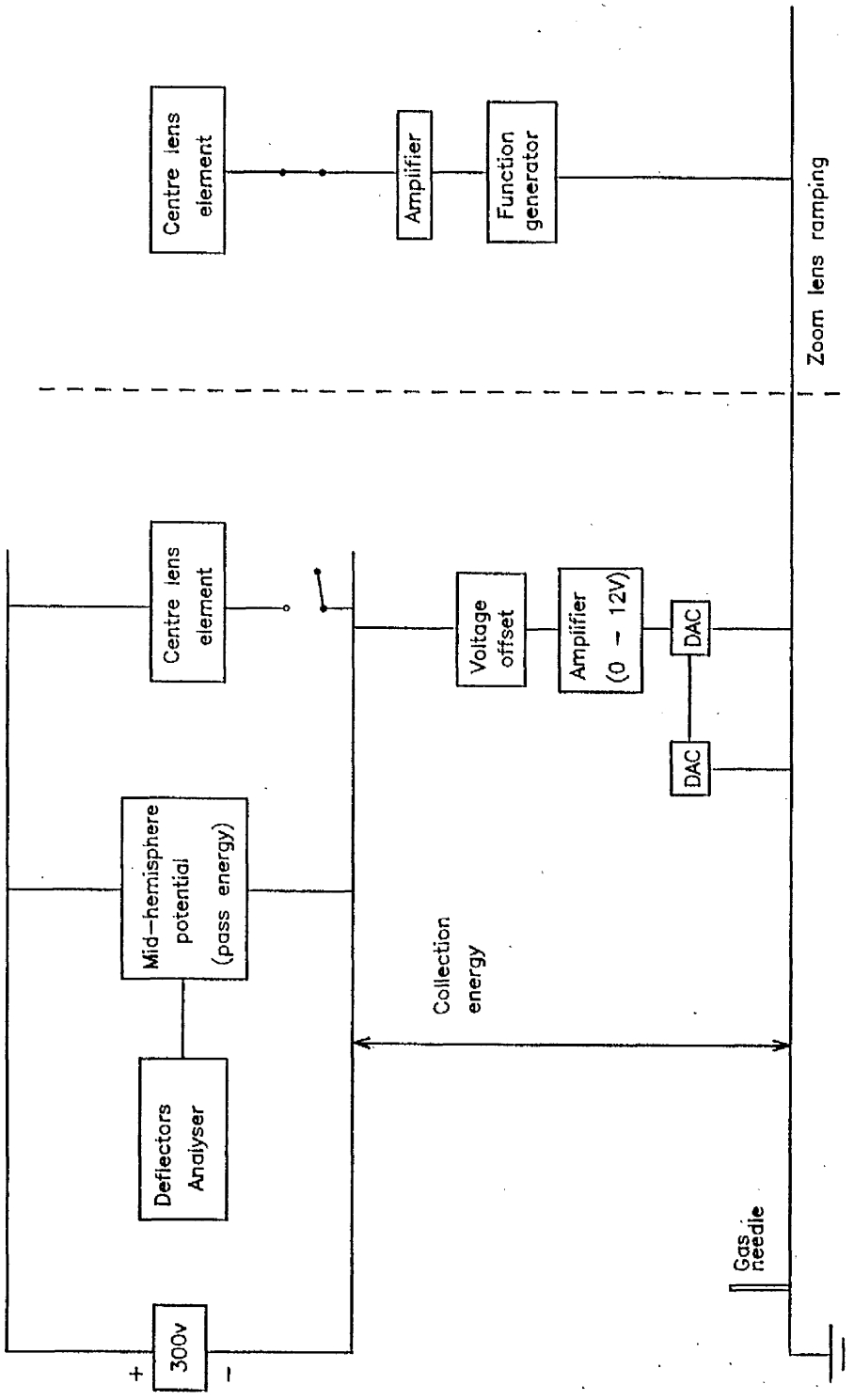

5.4 Detector Electronics

The Integrated Circuit (IC) detector (section 4.4) is mounted in close proximity to the exit of the microchannel plates (MCP's). The high voltage (2.5-3kV) applied to the MCP output plane must therefore become the virtual earth of the IC, shown schematically in figure 5.4. The 8 bit data output by the chip thus comprises logic levels of a few volts sitting on a high voltage 'table'. Opto-isolators are used to remove the high voltage so that the data may be transferred, by ribbon cable, to the PC.

End of frame (EOF) and pixel read (PR) timing pulses control the sequential output of data from the detector counters to a Singular si8255 digital I/O and counter card [35] within the PC.

The length of the sampling period, during which each electrode waits for a pulse, can be varied by a potentiometer on the detector controller board. Variable logic switches control the number of sampling periods per frame, up to a maximum of 255 for each channel. The EOF pulse is produced by a counting chip when the required number of sampling periods have been completed by every pixel.

In this study a sampling period of 300μs was chosen in consideration of the low count rate (section 4.4.2). 40 sampling periods were completed by each electrode in a single frame, producing a frame pulse every 12ms.

Figure 5.4

Schematic of the earth potential of the Integrated Chip detector.

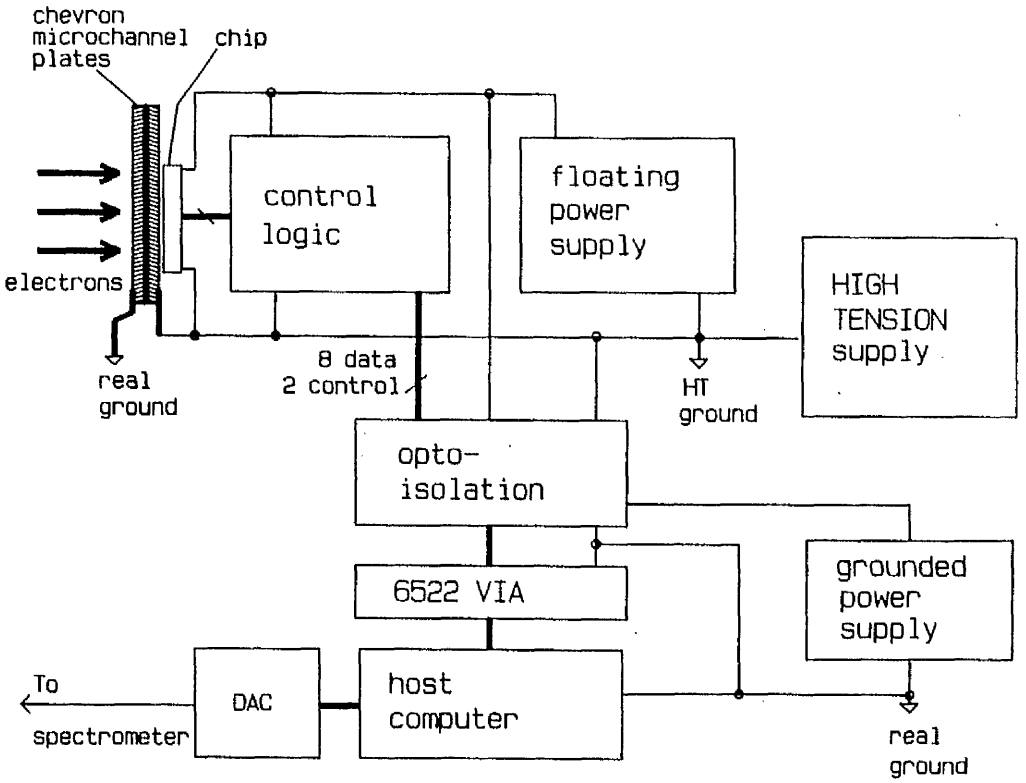

5.5 Tuning of the Spectrometer

The electron optics are tuned manually to obtain optimum peak size and shape. Peaks from strong ionisation lines (He : $1s(^2S)$ at 24.58eV, Ne : $2p^5(^2P)$ at 21.57eV or Ar : $3p^5(^2P)$ at 15.76eV) [36] are used over a range of collection energies greater than that needed by the study.

The ergonomics of spectrometer tuning, which can determine the quality of results obtained, has been improved by the new detector. Peak size and shape can now be displayed on the PC monitor, and refreshed at a rate of a few Hertz. Presently, the single integrated chip (IC) detector covers approximately 5mm of the image at the analyser exit. This corresponds to an energy range of about 0.2eV for 8eV pass energy, enough to view one or two peaks (typical resolution 40-60meV). Advances are being made towards a hybrid detector, made up of any number of IC detectors placed side by side. This will allow a small photoelectron spectrum to be observed during tuning.

5.6 Data Collection

The variety of ways in which data can be collected with this control system is described below. An understanding of the method of production of two dimensional spectra is important when trying to understand the features therein.

5.6.1 Photoelectron Spectra

To obtain a photoelectron spectrum (PES) the photon energy is

chosen, and fixed. The electron image is then scanned across the analyser exit over the required collection energy range.

To allow for variations in the sensitivity of different pixels across the detector it is necessary to ensure that each data point in a spectrum has had a contribution from every detector pixel. This is achieved by stepping the electron image across the detector in collection energy increments equal to the energy difference between two adjacent pixels, shown schematically in figure 5.6.1.

It follows that there will be data points at the beginning and end of a spectrum that have not had a contribution from every pixel. These data points are discarded so that only those which have been collected over the whole detector are included in the final spectrum.

The energy difference between adjacent pixels on the detector is governed by the pass energy of the analyser and is a measure of its dispersion. The dispersion is determined experimentally by measuring the collection energy change required to move a peak across the detector. For an 8eV pass energy, dispersion is approximately 6meV/Channel.

5.6.2. Two Dimensional Spectra

Collection energy scale 2D spectra

In this type of spectrum the electron yield is measured as a function of both collection energy and photon energy. The monochromator is set to an initial photon energy and a PES (sect. 5.6.1) recorded over the required collection energy range. The photon energy is then incremented and

Figure 5.6.1

A schematic of the scanning data collection technique.

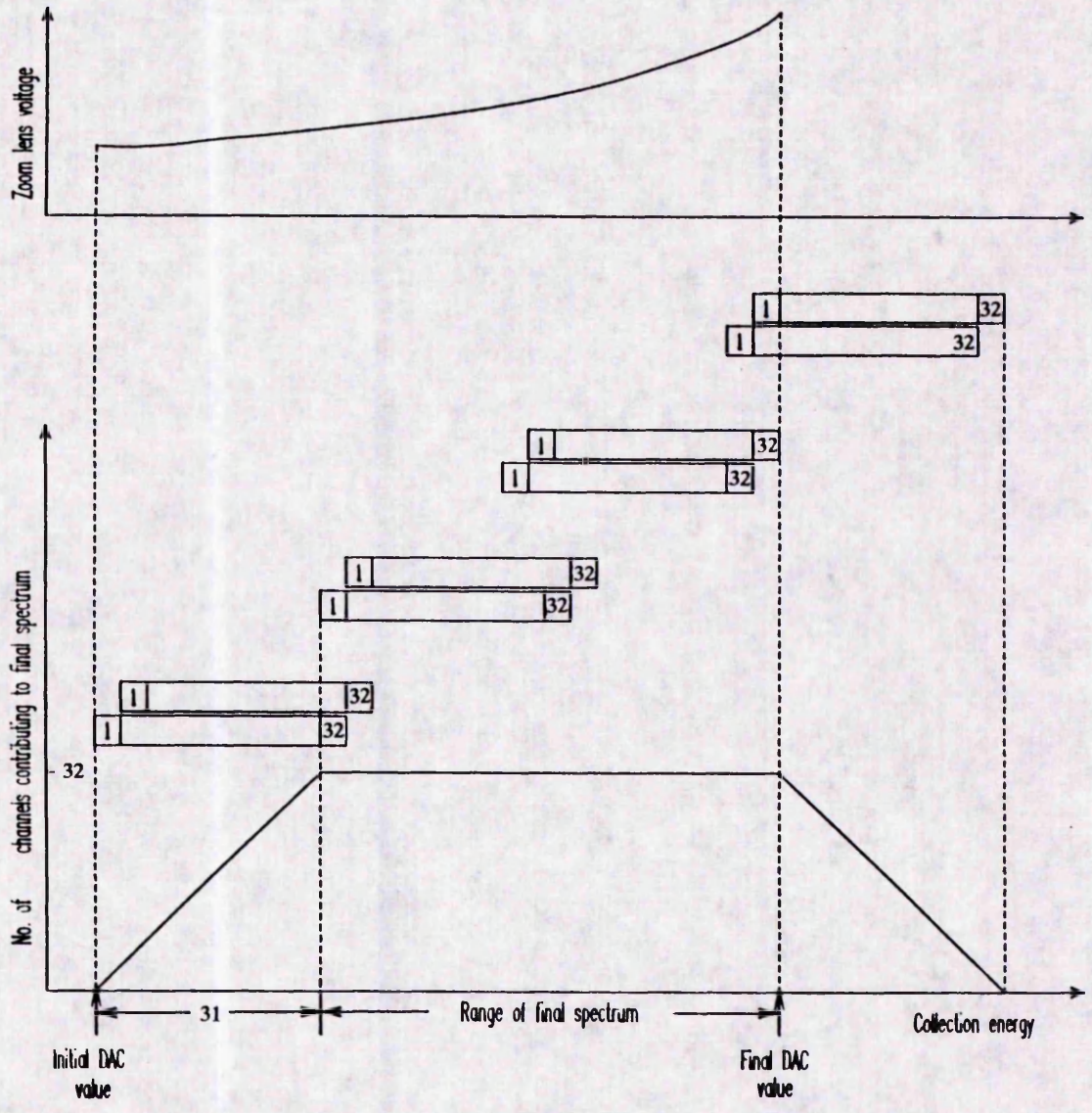

a second PES recorded over the same collection energy range. The PES's are then stacked to form the first and second lines of a two dimensional spectra, the axes of which are photon energy and collection (kinetic) energy. A schematic view of the spectra that can be extracted from this type of data set is shown in figure 5.6.2(a).

Binding energy scale 2D spectra

In this type of spectrum the monochromator is set to an initial photon energy, and a PES (sect. 5.6.1) recorded over a given collection energy range. The photon energy is then incremented by an integer multiple of the dispersion (sect. 5.6.1). The initial collection energy is also incremented, from that of the previous PES, by an amount equal to the photon energy step, and a second PES is recorded.

In this way a two dimensional spectra is built up with axes of photon energy ($h\nu$) and binding energy (B.E.), where collection energy

$$C.E. = h\upsilon - B.E.$$

A schematic view of the spectra which can be extracted from this type of 2D data set is shown in figure 5.6.2(b).

Figure 5.6.2(a)

A schematic view of a Collection Energy Range 2D spectrum showing the types of spectra that can be subsequently extracted. In each case either photon energy E_p, binding energy E_b or electron kinetic energy E_e is constant.

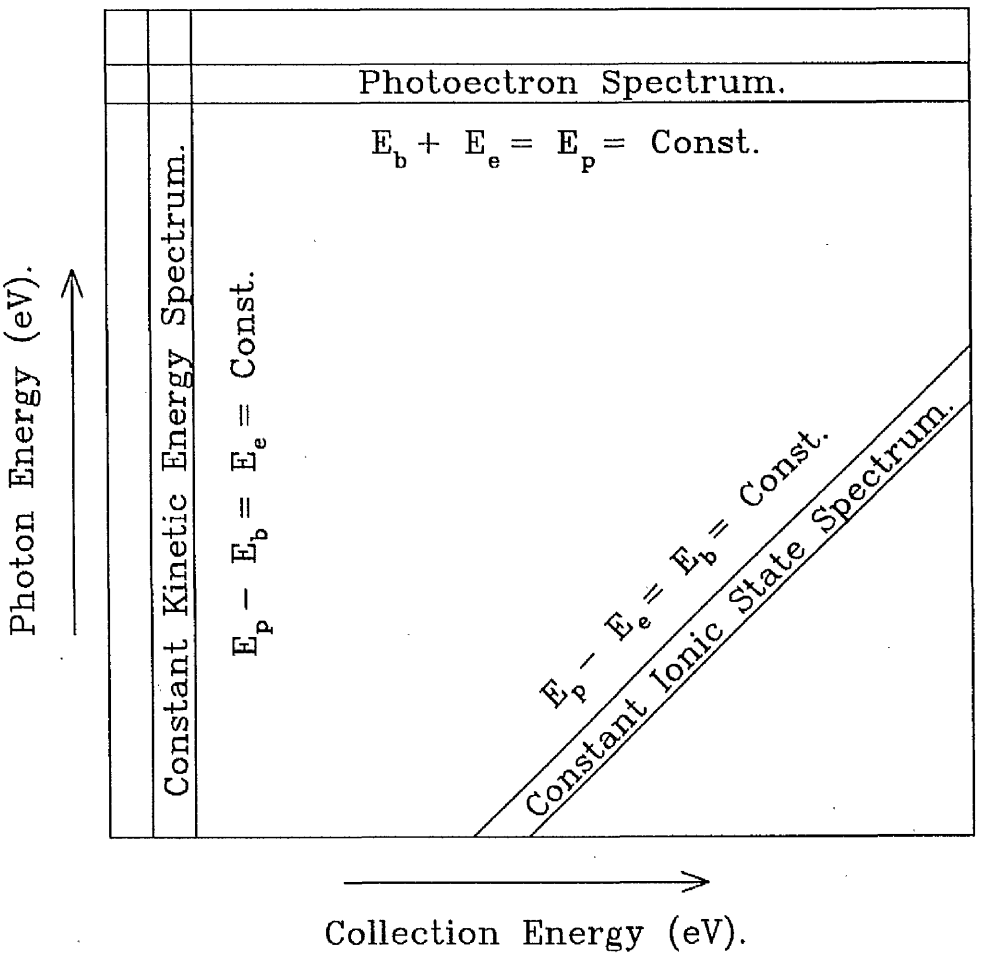

Figure 5.6.2(b)

A schematic of a Binding Energy Range 2D spectrum and how different types of spectra may be extracted from it.

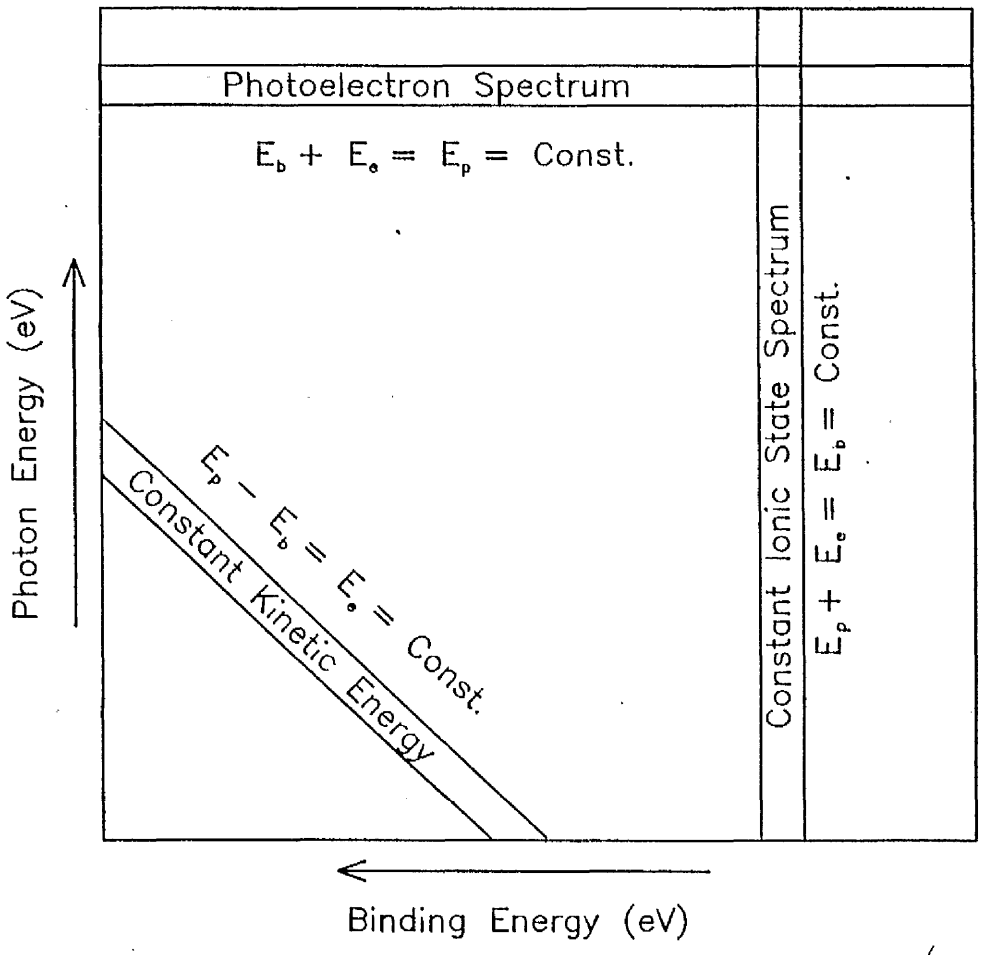

Odd shaped spectra

The use of pre-set parameter files to govern the studies performed through the PC allows for great versatility in the type of spectra taken. Two dimensional spectra of either type described above can be taken in any region of photon and collection energy allowed by the experiment. Gradual expansion, diminution, or jumps in the energy range of spectra are possible, giving the concept of odd shaped spectra, designed to cover only the energy regions of interest. Furthermore, multiple studies can be edited together onto one parameter file, to be performed consecutively. Beam time can therefore be used to its optimum and an automatic record is kept of all studies.

5.7 Corrections applied to the data

5.7.1 Correction for variation in light intensity

During the accumulation of a spectrum, the intensity of the photon beam may vary due to the decay of the electron beam (lifetime ≈ 24hrs) in the storage

ring. Light intensity is also a function of photon energy due to monochromator characteristics (section 2.3).

Monitoring of light intensity variations is achieved using a photodiode positioned at the end of the target region, figure 3.1. Photodiode output is taken by co-axial cable to an electrometer adapted to give a frequency output. A measure of the frequency is taken automatically, before every accumulated line of data, by the 8255 singular I/O card [35] within the

PC. Corrections can then be made to the data such that variations in the electron yield can be seen independently of variations in light intensity.

5.7.2 Correction for analyser transmission function

The throughput, or transmission of the electron lens varies with collection energy, imposing a machine dependent variation on electron yield. This function is obtained by measuring the intensity of photoelectrons, produced by ionisation of the outer valence levels of one of the rare gases, as a function of photon energy. The absolute cross sections for photoionisation of the rare gases are tabulated by Marr and West [36] for a wide range of photon energies.

The spectrum is obtained as a constant ionic state spectrum, figure 5.6.2(b), and is first corrected for light intensity variations (section 5.7.1). Comparison with the absolute cross sections taken from Marr and West then provides a correction function to apply to the data as a yield multiplication factor dependent on energy of collection.

5.8 Calibrations applied to the data

Photon energy has been calibrated by recording spectra of the well known first ionisation potential of Argon (Ar : $^2P_{3/2}$). Electron energy has then been calibrated using well known photoelectron peaks [37][38][39] within the spectra.

CHAPTER SIX

PHOTOIONISATION THEORY

6.1 Introduction

Recent theoretical studies have been an invaluable aid in the analysis of the photoelectron spectra presented in the following chapters. In this chapter an attempt has been made to clarify the theory qualitatively, explanations of the methods used in the calculations being kept brief.

6.2 The Independent Particle Model

An extremely useful concept used to rationalise ionisation spectra is the single particle picture or shell model. In this approximation electrons are independent and the features in the ionisation spectrum of a molecule can be associated with a molecular orbital.

The sudden ejection of an electron from the molecular orbital ϕ_q in the initial molecular state $|\psi^N{}_0\rangle$ results in a pseudo-state $a_q|\psi^N{}_0\rangle$, where a_q is the corresponding annihilation operator.

The probability of finding the final ionic state $|\psi^{N-1}{}_n\rangle$ in this pseudo state is the absolute square of the transition amplitude [40]

$$\chi^{(n)}{}_q = \langle\psi^{N-1}{}_n|a_q|\psi^N{}_0\rangle \quad \ldots.6.1$$

This probability $|\chi^{(n)}{}_q|^2$ is the pole strength or spectroscopic

factor and is related to the partial-channel ionisation cross-section σ_n. Unlike σ_n, pole strengths are independent of experimental conditions such as ejected electron kinetic energy, scattering angle and the polarisation of the incident light.

The ionisation process would be particularly simple if the electrons were truly independent. In this case the only non-vanishing transition amplitude $\chi^{(n)}_q$ would be the one for which the ionic configuration differs from the initial neutral molecular configuration only by the occupation of the molecular orbital ϕ_q.

Thus in the independent particle picture an ionisation spectrum would consist of discrete lines, each attributable to the ejection of an electron from a single molecular orbital, leaving the ion with a *hole* in that orbital. This model often allows the identification of *main lines* within the spectra that are said to be due to one hole (1h) configurations and will be strong as long as electron-electron interaction is weak.

6.3 Configuration Interactions

Corrections to the independent particle model arise due to electron correlation causing extra bands to appear in the ionisation spectra. These so called *satellite lines* correspond to excitation processes accompanying the ionisation.

The origin of the phenomena lies in the quasi-degeneracy of the single-hole (1h) ionic configuration with two-hole one-particle (2h-1p) and higher excited configurations of the ion. In the independent particle model

there is no access to 2h-1p or higher excited ionic configurations, the transition amplitude $\chi^{(n)}_q$ vanishes for these states. The interaction of these quasi-degenerate configurations via electron-electron interaction leads to a redistribution of the intensity previously associated with the inner valence orbital.

If the interactions are weak, ionic states of 1h configuration are much more probable than other states and the main lines will dominate the spectrum. In this context satellite lines are said to *borrow* intensity from one or several orbitals to become visible in the spectrum.

If the interactions are strong, the intensity may be distributed over several lines making the main lines impossible to distinguish from satellite lines. This effect is termed the breakdown of the molecular orbital picture of ionisation.

6.4 Calculations

In the theoretical analysis of these phenomena the favoured mathematical model uses the molecular ground state Hartree-Fock (HF) particles to introduce an independent particle basis to the picture. This particular choice of independent particle model has the advantage that a given ionic state $|\psi^{N-1}{}_n\rangle$ is only accessible in first order perturbation theory due to ionisation from a single molecular orbital ϕ_q. Hence, with the use of ground state HF orbitals, each calculated line may be attributed to exactly one occupied orbital, ($\chi^{(n)}_q \neq 0$ for only one orbital ϕ_q).

The molecular and ionic wavefunctions of equation 6.1 are now

represented by ground state HF orbitals. In order to extend the analysis to include the calculation of pole strengths for satellite lines, the molecular and ionic wavefunctions are expanded in terms of electron configurations constructed from the ground state HF orbitals as a basis.

The neutral molecular wavefunction thus comprises the HF ground state configuration as well as singly-excited, doubly-excited and so on configurations. These may be called one-particle-one-hole (1p-1h), two-particle-two-hole and so on configurations. Similarly, the ionic wavefunction is expanded to become a superposition of single-hole (1h) two-hole-one-particle (2h-1p) and higher excited electron configurations.

It is the interaction of the 1h with 2h-1p or higher configurations that cause the appearance of satellite lines in the spectra. The inclusion of such configurations in the mathematical model has produced successful predictions of experimental results.

There are essentially two approaches to the computation of energies and pole-strengths. In the more obvious approach the energies and wavefunctions of the neutral molecular and the final ionic states are computed separately, and the desired quantities subsequently calculated. This is the approach of the various Configuration Interaction methods [41][42][43]. In the second approach, energies and pole-strengths are calculated directly, as the eigenvalues and eigenvector components of a single matrix. An example of this approach is the Green's Functions method.

Variations of the Green's functions method to be referred to later are;

the Algebraic Diagrammatic Construction of the one particle Green's function extended to fourth order (ADC(4)) [44],

the Extended two-particle-hole Tamm-Dancoff Approximation (Ext.2phTDA) (which is essentially an ADC(3) calculation) [45],

and the Multiconfigurational Electron Propogator (MCEP) calculations [46].

The interested reader is directed to the above cited references for further discussion of these methods and to a comprehensive review article [47] for technical details of the computations.

6.5 Classification

Where intense satellite lines are found the majority show a single dominating pole strength $|\chi^{(n)}{}_q|^2$. This indicates a single dominating process has made the lines visible in the spectrum and allows for some classification of the lines.

If the 2h-1p configuration is denoted by $m^{-1}n^{-1}t$ and the ionisation takes place out of orbital ϕ_q, where q is equal to either m or n ,the satellite line mainly originates from the relaxation of the molecular orbitals after creation of a hole in orbital ϕ_q. The final state can be seen as a 1h-1p excitation on top of the 1h configuration from which its intensity has been borrowed. These cases are often called *shake up* satellites and are prevalent in the ionisation of spatially localised orbitals, such as core orbitals where relaxation effects are

substantial.

Alternatively, final state correlation effects can produce satellites for which neither m nor n are equal to q. Such states are called *correlation* satellites.

Finally, a third kind of satellite has been observed which could not appear without ground state correlation. For example, without considering electron correlation effects in the molecular ground state of N_2, since there is no occupied π_g orbital, the $^2\Pi_g$ states in N_2^+ cannot appear in the spectrum. Including electron correlation effects in the molecular ground state allows $a_q|\psi^N{}_0\rangle$ to be non zero for any virtual orbital ϕ_q, making states like the $^2\Pi_g$ states of N_2^+ accessible. The corresponding lines are called *initial-state correlation* satellites.

6.6 The Shape of Spectra

Since the 2h-1p and higher excited configurations are generally found at higher binding energies than the outer-valence orbitals, the lower binding energy side of a typical ionisation spectra will produce main lines only. In the higher binding energy range of small molecules the density of 2h-1p configurations is low and spectra exhibit a few satellite lines which have borrowed their intensity from the outer valence orbitals. An example to be seen in the results of the following chapter is the $C^2\Sigma_u^+$ correlation satellite state of N_2^+. This state, observed at about 25eV binding energy, has borrowed its intensity from the outer-valence $2\sigma_u$ orbital, and is well characterised by the $(3\sigma_g)^{-1}(1\pi_u)^{-1}(1\pi_g)$ configuration.

At higher binding energies, in the range of the inner-valence orbitals, the density of 2h-1p configurations increases. In this region satellite lines may have contributions from several configurations rendering the above classification scheme (sect.6.5) inappropriate. Furthermore, several 2h-1p configurations may lie energetically close to the q^{-1} configurations of the inner-valence orbitals ϕ_q. In this case the interaction between the 1h and 2h-1p configurations may be stronger and the intensity distributed more efficiently over many satellite lines.

The conceptual significance of main lines could be said to reduce with their intensity, their distinction over the many satellite lines having less significance in explaining the spectra. It is at this stage that the breakdown of the molecular orbital picture is said to be complete.

6.7 Conclusion

A theory has been presented above that explains the overall shape of the photoionisation spectra presented in this study. Relevant calculations derived by various authors from this theory will be presented with the results of this work, and conclusions drawn from any quantitative agreement.

CHAPTER SEVEN

PHOTOELECTRON STUDY OF MOLECULAR NITROGEN

7.1 Introduction

Previous photoelectron studies of the valence ionisation of Nitrogen have employed X-ray photons [48][49][50], He II photons at 40.81eV [51], and synchrotron radiation [52][53]. Electron impact techniques [54][55] have provided further insight into the ionisation process. The complexity of this process is due to electron correlation effects which can cause single, or multiple excitation to accompany the ionisation.

These correlation effects have attracted intense theoretical interest [40] including studies using both Configuration Interaction [43] and Green's function methods [44]. They are also the main subject of the present investigation into the photoionisation of Nitrogen.

7.2 Experimental

In this study, a collection energy range 2D spectrum (sect.5.6.2) has been taken using the Toroidal Grating Monochromator (TGM sect.2.3.2). A fixed electron energy range from 0.2 to 2eV was accepted for photon energies stepped by 6meV from 23 to 43eV.

A section of this 2D spectrum, shown in figure 7.1, illustrates how this scanning method detects and differentiates electrons due to molecular states from those due to the autoionisation of excited states of atomic nitrogen,

Figure 7.1

The Collection Energy Range 2D Spectrum of N_2. Photoelectron yield is represented by colour with the highest intensity in black. The diagonal lines are due to molecular photoionisation and the vertical lines due to atomic autoionisation.

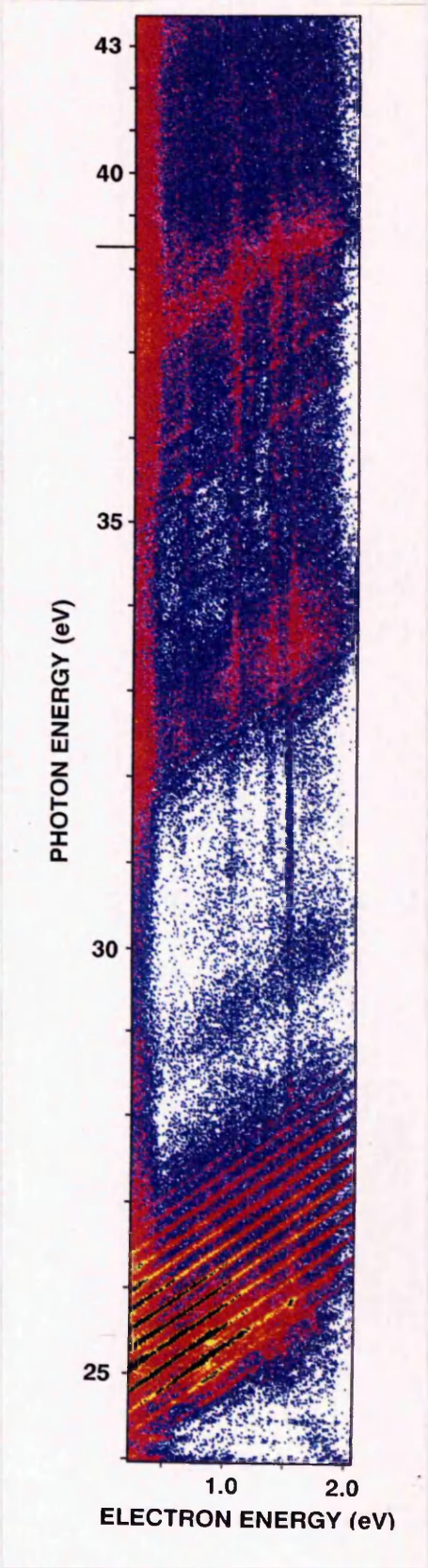

Note:-
All colour plots contained in this work are presented on a logarithmic scale with colour change levels chosen to best highlight the peaks

produced by neutral photodissociation of N_2.

After the necessary data corrections and calibrations have been completed (sects.5.7 & 5.8), the 2D spectrum can be used to construct a single photoelectron spectrum. With reference to the spectrum in figure 7.1 one can mask the vertical atomic lines and compress the surface along the diagonal molecular lines to produce a single binding energy range spectrum. Each point in this spectrum has contributions from an extended range of photon (and hence photoelectron) energies, in this case about 1.8eV.

The final spectrum derived in this way has been compared with photoelectron spectra taken at a variety of fixed photon energies. Figure 7.2 shows the compressed near threshold photoelectron spectra (NTPES) along with a PES taken at 50eV photon energy. The resolution (60meV) has not been degraded by the compression process whilst statistical quality has obviously improved.

An advantage of this two dimensional data collection technique for producing binding energy range PES's comes from the fact that the states have been excited near to their thresholds. The photon energies used have thus been kept low, and since photon bandwidth scales with energy this is the region of highest photon resolution for each state.

Significant improvements to photon resolution and electron detection efficiency have enabled many vibrational features to be seen in this energy region of the N_2 spectrum for the first time. However, there is a disadvantage to working near threshold. As the plane wave approximation is not applicable to electrons leaving the ion core with such relatively low

Figure 7.2
The Near Threshold photoelectron spectrum (NTPES) of N_2 shown with a photoelectron spectrum taken at 50eV photon energy.

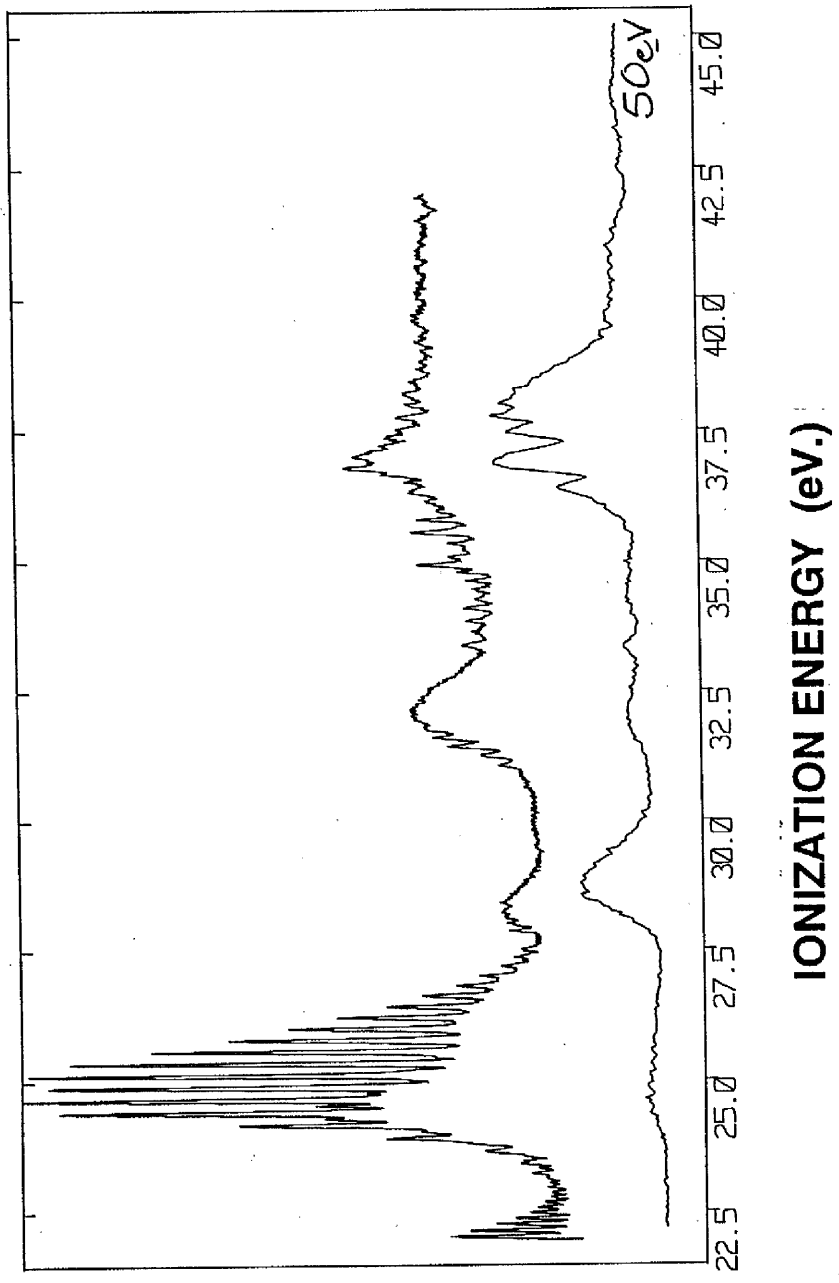

velocities, comparison with theoretical studies is made more difficult. This is particularly true when considering the relative intensities of features. Figures 7.3 and 7.4 show how the intensities of features vary as a function of photon energy.

7.3 The Satellite Spectrum of Molecular Nitrogen

7.3.1 Introduction

The ground state configuration of N_2 can be expressed, using the LS coupling scheme as;

$$(1\sigma_g)^2(1\sigma_u^*)^2(2\sigma_g)^2(2\sigma_u^*)^2(1\pi_u)^4(3\sigma_g)^2 \quad {}^1\Sigma_g^+$$

The three lowest energy states of N_2^+ can be considered in the independent particle model as ionisation from the ($3\sigma_g$), ($1\pi_u$) and ($2\sigma_u$) molecular orbitals. They are assigned as $X^2\Sigma_g^+$ (at 15.581 eV), $A^2\Pi^+$ (at 16.699eV) and $B^2\Sigma_u^+$ (at 18.751eV) respectively.

As has been discussed above (chapt.6) electron correlation effects can cause excitation processes to accompany the ionisation. This phenomenon results in additional weaker bands appearing in the spectrum. These so called satellite bands are characterised by the excited electron configuration of the ion that produced them (sect.6.5).

An example is the $C^2\Sigma_u^+$ state of N_2^+ at about 25eV binding energy. This state is due to the 2h-1p excited electron configuration of the ion

Figure 7.3
Photoelectron spectra of N_2 taken at successively increased photon energies to show the variation in dominance of spectral features.

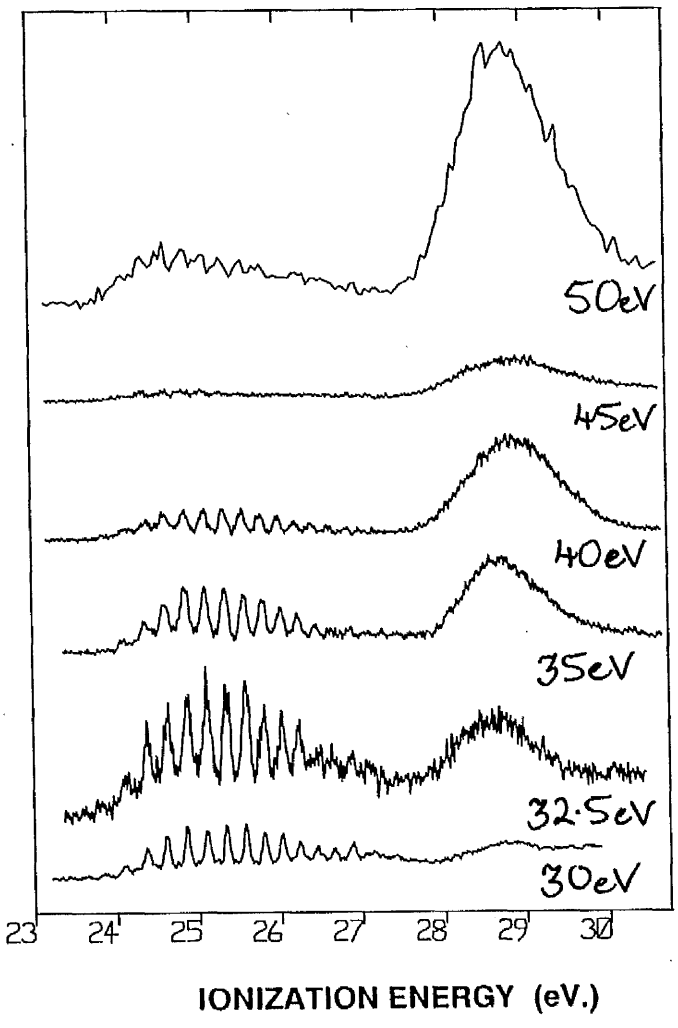

Figure 7.4
Photoelectron spectra of N_2 taken at successively increased photon energies to show the variation in dominance of spectral features.

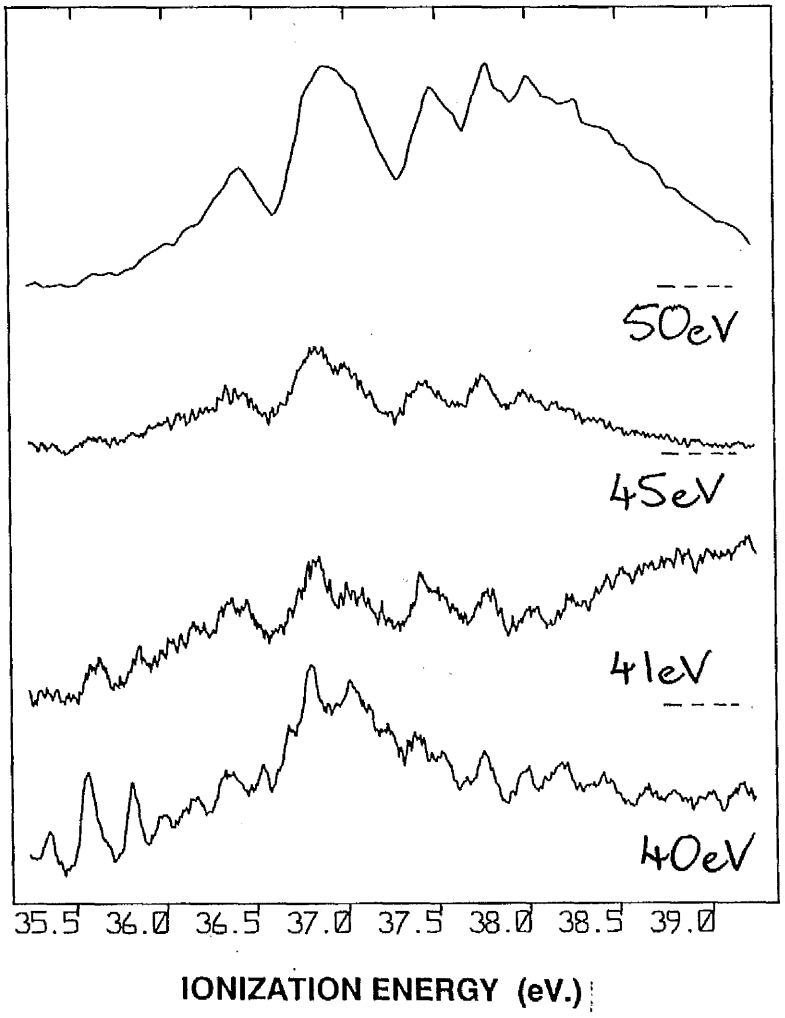

$(3\sigma_g)^{-1}(1\pi_u)^{-1}(1\pi_g)$. It is the quasi-degeneracy of this state with the 1h main-line state of equal symmetry ($^2\Sigma_u^+$) that enables the satellite bands to borrow their intensity from the main line.

It should be noted that in the 1h picture of N_2, a state of $^2\Sigma_u^+$ symmetry is due to removal of an electron from the $2\sigma_u$ orbital. This is a different orbital from either of the two holes [$(3\sigma_g)^{-1}$, $(1\pi_u)^{-1}$] in the $C^2\Sigma_u^+$ state configuration. The $C^2\Sigma_u^+$ state can therefore be said to have become visible in the spectrum due to final-state correlation effects and is classified (sect.6.5) as a correlation satellite.

At higher binding energies, where deeper valence orbitals are energetically close to a higher density of excited electron configurations of the ion, the situation is more complex. This is the case in the 35-45eV region for ionisation of the inner-valence electron from the $2\sigma_g$ orbital. The intensity of lines in this region is so well distributed that it is impossible to distinguish the main line from the satellite lines. It is at this point that there is said to have been a severe breakdown of the molecular orbital picture of ionisation, (sect.6.6).

7.3.2 Calculations

The Configuration-Interaction study of Langhoff et al [43] considers contributions from both 2h-1p, and a limited set of higher 3h-2p excited configurations of the ion. The results have been presented in table 7(a) where 2h-1p contributions are denoted as single-excited CI (SECI) and 3h-2p contributions are denoted as polarisation CI (POLCI).

Table 7a: Configuration Interaction (CI) Calculations[#] of N_2^+.

Symmetry	SECI[1] Energy (eV)	SECI[1] SHSI* $2\sigma_g$	SECI[1] SHSI* $3\sigma_g$	POLCI[2] Energy (eV)	POLCI[2] SHSI* $2\sigma_g$	POLCI[2] SHSI* $3\sigma_g$
	15.58	0.001	0.898	15.58	0.012	0.836
				29.50	0.088	0.026
	30.95	0.157	0.014			
				35.34	0.078	..
				37.02	0.054	0.014
$^2\Sigma_g^+$	38.32	0.207	0.004			
	38.40	0.293	..			
				39.37	0.528	0.001
				39.56	0.014	..
	40.97	0.030	0.003	41.15	..	0.005
	41.25	0.003	..			
	41.72	0.020	0.001			
	42.21	0.006	..	42.24	0.022	..
	42.43	0.125	0.013			
	43.16	0.021	0.001	43.22	0.007	0.002
				43.80	0.014	..
		$1\pi_u$			$1\pi_u$	
	16.93	0.948		16.93	0.892	
$^2\Pi_u$				33.21	0.007	
	37.64	0.003				
		$2\sigma_u$			$2\sigma_u$	
	18.75	0.836		18.75	0.763	
				25.42	0.066	
	27.17	0.034				
$^2\Sigma_u^+$				34.03	0.035	
	37.88	0.036				
	38.84	0.006		38.74	0.009	
				42.43	0.003	

* Only single-hole-strength intensities (SHSI) - or pole strengths -greater than 0.003 are shown.

1 SECI : Single-Excitation Configuration Interaction calculations (see text).

2 POLCI : Polarisation Configuration Interaction calculations (see text).

Results from Langhoff et al [43]. The calculated energies have been normalised to the experimental energies of the vertical transitions for each symmetry, as the CI studies only confidently give such relative energies. Since vertical transitions are required, the calculations have been normalised at $X^2\Sigma_g^+$ v=0 (at 15.581eV), $A^2\Pi_u^+$ v=1 (at 16.932eV), $B^2\Sigma_u^+$ v=0 (at 18.751eV), which are approximately at the respective peaks of the Franck-Condon overlaps.

As CI studies only confidently give relative energies for states, the calculated values have been normalised to the experimental energies. The calculations have been normalised at $X^2\Sigma_g^+$ v=0 (15.581eV), $A^2\Pi^+$ v=1 (16.932eV) and $B^2\Sigma_u^+$ v=0 (18.751eV). This satisfies the requirement of normalisation at vertical transitions for each symmetry, since these energies correspond approximately to the peaks of the Franck-Condon overlaps.

It should be noted that since the POLCI calculations were obtained by considering an occupied $^1\pi_g$ orbital in neutral N_2, the differences between SECI and POLCI results provides an insight into the role of initial-state correlation effects in the photoionisation spectrum of N_2.

In addition to the CI energies of table 7(a), there have been several Green's functions calculations [43][44][45] on molecular Nitrogen. In these studies no normalisation is necessary as the excitation energies are determined directly from the neutral ground state. Initial state correlation is also generally included in these calculations. The advantages of the various approaches have been discussed by their authors and in review articles [40][56]. The results of three recent studies [44][45][46] are presented in table 7(b).

When referring to the pole-strengths in tables 7(a) and (b) it must be noted that they are only directly proportional to the cross-section when the spectral feature at a certain energy is dominated by one particular transition. If the feature has become visible through contributions from several electron configurations, these contributions must be summed to find the total cross-section at a specific energy.

Table 7b: Green's Function Calculations of N_2^+.

Symmetry	ADC(4)[1] Energy (eV)	Pole Strengths $2\sigma_g$	Pole Strengths $3\sigma_g$	Ext. 2ph TDA[2] Energy (eV)	Pole Strengths $2\sigma_g$	Pole Strengths $3\sigma_g$
	16.01	..	0.888	15.70	..	0.91
	28.45	0.070	0.017	29.20	0.10	..
	34.87	0.046	0.004			
	35.83	0.007	0.001			
	36.06	0.002	0.003			
$^2\Sigma_g^+$	36.85	0.001	0.002			
	37.14	0.002	0.001	37.43	0.30	
	37.76	0.133	..	37.56	0.10	
	38.85	0.342	..	38.97	0.14	
	38.93	0.236	..	39.25	0.04	
				39.94	0.15	
				40.62	0.06	
		$1\pi_u$			$1\pi_u$	
	17.41	0.904		16.85	0.92	
$^2\Pi_u$	31.94	0.007		28.63	<0.01	
	38.90	0.003		35.57	<0.01	
		$2\sigma_u$			$2\sigma_u$	
	19.07	0.780		18.96	0.82	
	24.67	0.089		25.13	0.07	
$^2\Sigma_u^+$	33.05	0.035				
				35.34	0.002	
	39.15	0.003				
				41.28	0.003	
				44.13	0.001	
				44.87	0.002	

1 ADC(4): Algebraic Diagrammatic Construction of the one particle Green's function extended to fourth order (Tomasello [44]).

2 Ext. 2ph TDA: Extended two-particle-hole Tamm-Dancoff Approximation, which is essentially an ADC(3) calculation (Schirmer and Walter [45]).

3 MCEP: Multiconfigurational Electron Propagator (MCEP) calculations (Nichols et al [46]).

Table7*b*: Cont.

	MCEP[3]	
Energy (eV)	Pole Strengths $2\sigma_g$	$3\sigma_g$
15.52	0.237	0.702
29.78	0.116	0.001
35.24	0.033	0.001
39.10	0.187	0.016
40.12	0.112	0.038
41.28	0.246	0.171
45.11	0.058	0.059
	$1\pi_u$	
17.24	0.957	
34.13	0.006	
	$2\sigma_u$	
18.56	0.848	
26.31	0.059	
37.17	0.065	
39.11	0.011	

In addition, for low energy photoelectron spectroscopy, the reaction dynamics must be considered when relating pole-strengths to intensities (sect.6.2). However, a better understanding of the complex satellite spectrum can still be found from these predicted energies and symmetries at low, as well as high photon energies.

7.3.3 The 23-33eV Binding Energy Range

With reference to the near threshold PES (NTPES) of figure 7.2, the low energy end of the spectrum shows the high vibrational levels of the $A^2\Pi^+$ state, followed by a strong vibrational series around 25eV. Figure 7.3 shows how the broad feature at around 29eV grows more prominent at higher photon energies, becoming the dominant feature in this binding energy range above about 35eV photon energy. The experimental energies and assignments of the features in this region are listed in table 7(c).

The band centred around 25eV is mentioned above as due to the $C^2\Sigma_u^+$ state, and is assigned as $(3\sigma_g)^{-1}(1\pi_u)^{-1}(1\pi_g)\ ^2\Sigma_u^+$. Previous observations of this state in photoemission to the $X^2\Sigma_g^+$ state [57] has revealed vibrational levels up to v=11. This has been extended up to v=18 in the present work.

The observed energy of the centre of this band (24.8eV, v=7) shows good agreement with both the POLCI calculations of Langhoff et al, which places the vertical ionisation potential (after calibration) at 25.42eV, and the Green's functions calculations which places it at 25.13eV (Ext.2phTDA) and 24.67eV (ADC(4)). Both the MCEP and SECI calculations are 1-2eV too

Table 7a:

Experimental Energies of the N_2^+ Satellite States Between 23-33eV.

Energies (eV) From NTPES		Assignments and leading configurations	Energies from 50eV PES
23.480 v = 0 23.748 v = 1 23.959 v = 2 24.219 v = 3 24.466 v = 4 24.701 v = 5 24.961 v = 6 25.158 v = 7 25.396 v = 8 25.672 v = 9	T_o = 23.290eV ω_e = 0.276eV $\omega_e x_e$ = 2.92meV	$^2\Pi_g$?	
23.580 v = 0 23.833 v = 1 24.094 v = 2 24.335 v = 3 24.583 v = 4 24.822 v = 5 25.056 v = 6 25.287 v = 7 25.513 v = 8 25.732 v = 9 25.947 v = 10 26.157 v = 11 26.362 v = 12 26.567 v = 13 26.760 v = 14 26.944 v = 15 27.127 v = 16 27.304 v = 17 27.444 v = 18	T_o = 23.454eV ω_e = 0.266eV $\omega_e x_e$ = 2.25meV	$^2\Sigma_u^+$ $(3\sigma_g)^{-1}(1\pi_u)^{-1}(1\pi_g)$	Broad band Vibrational structure not observed -
27.810 v = 0 27.951 v = 1 28.090 v = 2 28.190 v = 3	T_o = 27.732eV ω_e = 0.180eV $\omega_e x_e$ = 13.5meV		Broad band centred at 28.75eV $^2\Sigma_g^+$ $(2\sigma_u)^{-1}(1\pi_u)^{-1}(1\pi_g)$
31.016 v = 0 31.209 v = 1 31.388 v = 2 31.561 v = 3 31.778 v = 4	T_o = 30.934eV ω_e = 0.195eV $\omega_e x_e$ = 3.57meV		Broad band centred at 32.00eV $^2\Pi_u$ $(2\sigma_u)^{-1}(3\sigma_g)^{-1}(1\pi_g)$

high.

The high resolution in the present work has revealed a second weaker vibrational series in this region. This state has been listed in table 7(c) with v=0 at 23.480eV. The vibrational spacings indicate that the two series do perturb each other, as one might expect. The presence of the weaker state is identified here for the first time, and no second state of significant intensity has been predicted in this region by any of the theories. However, Schirmer and Walter (Ext.2phTDA) have predicted weak transitions at about 24.5eV due to a $(1\pi_u)^{-2}(1\pi_g)\ ^2\Pi_g$ or $(3\sigma_g)^{-2}(1\pi_g)\ ^2\Pi_g$ state which may correspond to the observed series.

The growth in prominence of the broad band centred around 28.75eV, with increasing photon energy, is accompanied by a shift of the peak position of the envelope. This indicates that there could be more than one electronic state in this energy region. The NTPES shows vibrational structure, beginning at 27.849eV, which appears to predissociate at about 28.8eV. This vibrational structure is not discernable at higher photon energies where the band becomes broad and featureless, with slight indications of structure at 28.50 and 29.40eV. Threshold photoelectron spectroscopy (TPES) (King et al: private communication) shows vibrational structure in this feature more clearly, with a lowest line at 27.85eV. The theoretical studies show one strong feature in this energy range which is characterised by $(2\sigma_u)^{-1}(1\pi_u)^{-1}(1\pi_g)$ as the leading configuration with $^2\Sigma_g^+$ symmetry. The dominant pole-strength comes from the $2\sigma_g$ orbital with varying contributions from the $3\sigma_g$ orbital.

The broad feature centred at 32.00eV is best predicted by the

ADC(4) study which gives a significant $1\pi_u$ pole-strength at an energy of 31.94eV. The state is characterised by the $(2\sigma_u)^{-1}(3\sigma_g)^{-1}(1\pi_g)$ configuration with $^2\Pi_u$ symmetry. As vibrational structure clearly visible in the NTPES has a spacing of 180meV, it could be resolved in the 50eV PES where it is not visible.

7.3.4 The 33-45eV Binding Energy Range

The only 1h state in this energy region is the $(2\sigma_g)^{-1}$ state with $^2\Sigma_g^+$ symmetry. The most prominent features in this energy region are therefore expected to be due to configurations with the same symmetry, since only these can borrow intensity from the $2\sigma_g$ orbital. The experimental measurements of figure 7.5 do however support the theoretical predictions of a severe breakdown of the molecular orbital picture in this region. The intensity being efficiently spread over a large number of ion states.

A number of theoretical studies [43][45][56][58][59] predict two-hole Rydberg states with parent configurations $(3\sigma_g)^{-1}(1\pi_u)^{-1}$ and $(3\sigma_g)^{-2}$. Above about 37eV there are also two-hole states predicted involving the $2\sigma_u$ orbital.

The 50eV PES in the present work shows broad bands similar to those found in previous experimental work carried out at photon energies of 1487eV [60] and 50.3eV [61]. At lower photon energies, however , the NTPES (figure 7.5) has revealed complex structure with a number of overlapping vibrational bands. Tentative assignments have been made of seven such bands, marked on figure 7.5 and listed in table 7(d).

Some support can be found for these assignments in work by

Figure 7.5
The high Binding Energy region of the Near Threshold Photoelectron spectra of N_2 (33-42eV) with the suggested assignments a to g.

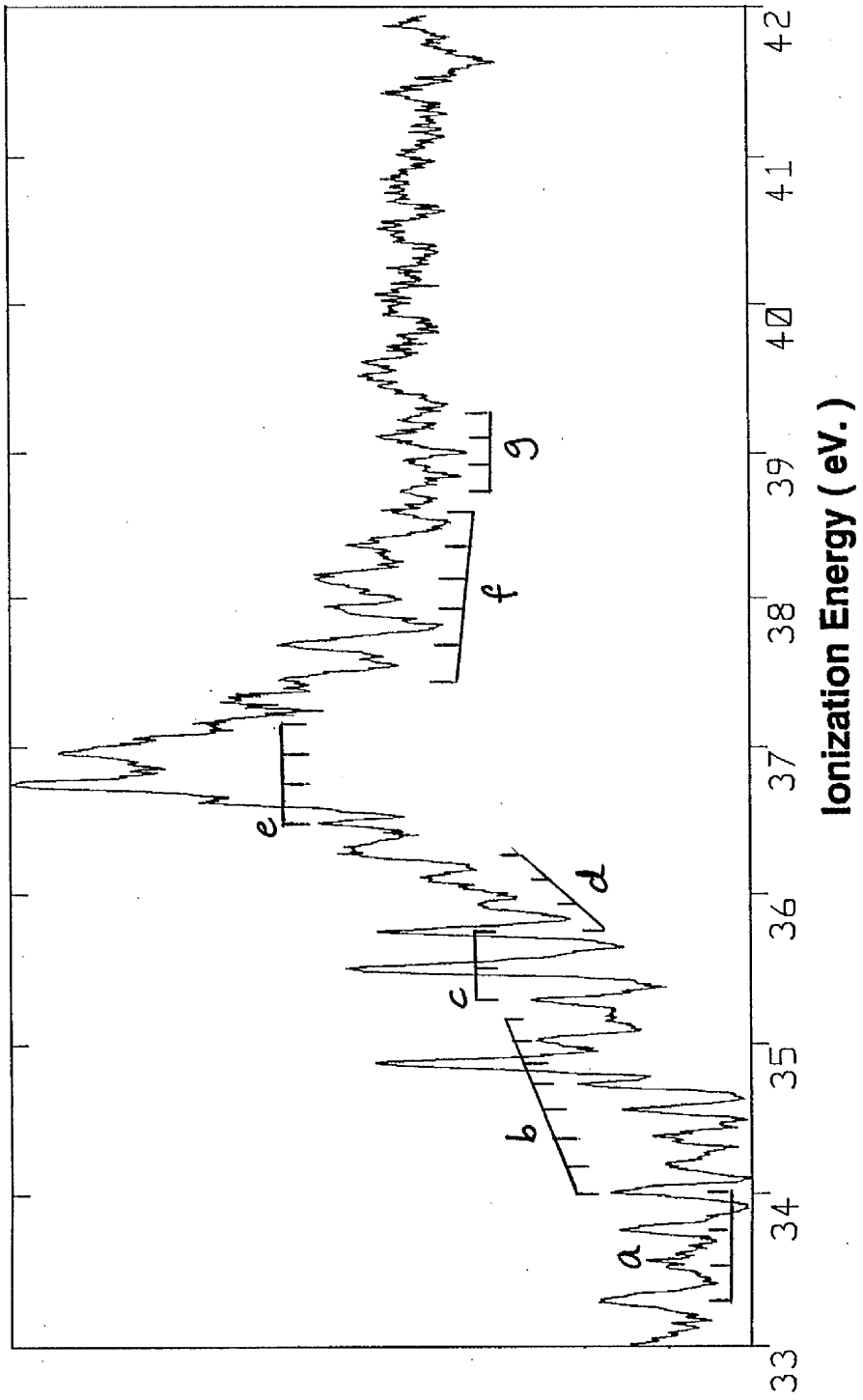

Table 7(d) Experimental energies of the N_2^+ Satellite States between 33-40eV.

Energies (eV) from NTPES	**label**	**Predicted Energies from Sambe & Ramaker [59] (eV)**	**Energies from PES taken at 50eV.**
33.303	a	33.6	33.292
33.567	a		
33.769	a		
34.023	a,b	34.2	
34.190	b		
34.260			
34.375	b		Broad weak band
34.562	b		34-35.5eV
34.730	b		
34.876	b		
35.026	b		
35.175	b		
35.299	c		
35.506	c		
35.757	c,d	36.0	
35.934	d		
36.105	d		
36.296	d		
36.482	e	36.7	Strong band with
36.628			structure at:
36.747	e		36.362
37.965	e		36.892
37.164	e		37.442
37.326			37.755
37.460	f	37.2	37.985
37.693	f		(38.214)
37.923	f		
38.128	f		
38.284			
38.373	f		
38.591	f		
38.737	g	38.5	Broad Shoulder
38.937	g		39-42eV
39.107	g		
39.227	g		

Sambe and Ramaker [59]. By considering a variety of atomic systems, Sambe and Ramaker have used the binding energies of Rydberg electrons (with both singly and doubly ionised cores) to predict the Rydberg energies of molecular N_2^+ states. Six of the bands shown in figure 7.5 have been identified with states predicted by Sambe and Ramaker, and this is shown in table 7(d).

Further support for these assignments can be found by considering the ω_e values of the states . Four of the states have values of ω_e in the range 227-240meV and three in the range 163-180meV. In the predictions of Sambe and Ramaker the cores are $(3\sigma_g)^{-1}(1\pi_u)^{-1}$ for the b, d and g series, $(3\sigma_g)^{-2}$ for a and e, and $(2\sigma_u)^{-1}(3\sigma_g)^{-1}$ for f. The 1h states of N_2^+ include the $A^2\Pi_u$ state corresponding to the removal of a $1\pi_u$ electron, which has a significantly smaller value of ω_e than the $X^2\Sigma_g^+$ and $B^2\Sigma_u^+$ states which correspond to removal of an electron from the $3\sigma_g$ and $2\sigma_u$ orbitals respectively.

The conclusion is that states which have a core $(3\sigma_g)^{-1}(1\pi_u)^{-1}$ should, like the 1h state from which they gain their intensity, have smaller values of ω_e than those with cores $(3\sigma_g)^{-2}$ and $(2\sigma_u)^{-1}(3\sigma_g)^{-1}$. This is indeed true for the six series a,b,d,e,f and g under discussion which are presented in table 7(e) to clarify the argument.

Any attempt at identification of the states observed in the present work with the states proposed in this energy region on the basis of CI and Green's function calculations would be very speculative. Further theoretical studies including vibrational information would be necessary before they could significantly clarify the spectrum.

Table 7(e)

Clarification of the argument for assignment of states a,b,d,e,f and g.

	low ω_e	high ω_e	
core configuration	$(3\sigma_g)^{-1}(1\pi_u)^{-1}$	$(3\sigma_g)^{-2}$	$(2\sigma_u)^{-1}(3\sigma_g)^{-1}$
symmetry	$^2\Pi^+$	$^2\Sigma^+_g$	$^2\Sigma^+_u$
corresponding 1h orbital	$(1\pi_u)$	$(3\sigma_g)$	$(2\sigma_u)$
series	b,d,g	a,e	f

7.4 Atomic Autoionisation following Photodissociation of N_2

In addition to molecular photoionisation, it is possible for electrons to be produced by neutral photodissociation of N_2 followed by fragment autoionisation

$$h\nu + N_2 \rightarrow N_2^* \rightarrow N + N^*$$
$$\downarrow$$
$$N^+ + e$$

Unlike electrons emitted by molecular photoionisation, the energy of which depends on photon energy, electrons produced in this way will have fixed energies.

The energetics of the process can be described by [62]

$$h\nu = D_0 + I + E_k + E_e$$

where $h\nu$ is the photon energy, D_0 is the dissociation energy of the molecular ground state, I is an ionisation potential of the fragment, E_k is the kinetic energy of the fragment atom and ion and E_e is the energy of the electron emitted following photodissociation.

As mentioned above several features of constant kinetic energy have been easily distinguished from the molecular photoelectron lines in the two dimensional spectrum, figure 7.1. A spectrum of these lines has been obtained from the two dimensional data and is shown in figure 7.6. This is

Figure 7.6
The constant kinetic energy spectrum of N_2. Obtained from summation of the CE2D spectrum (figure 7.1).

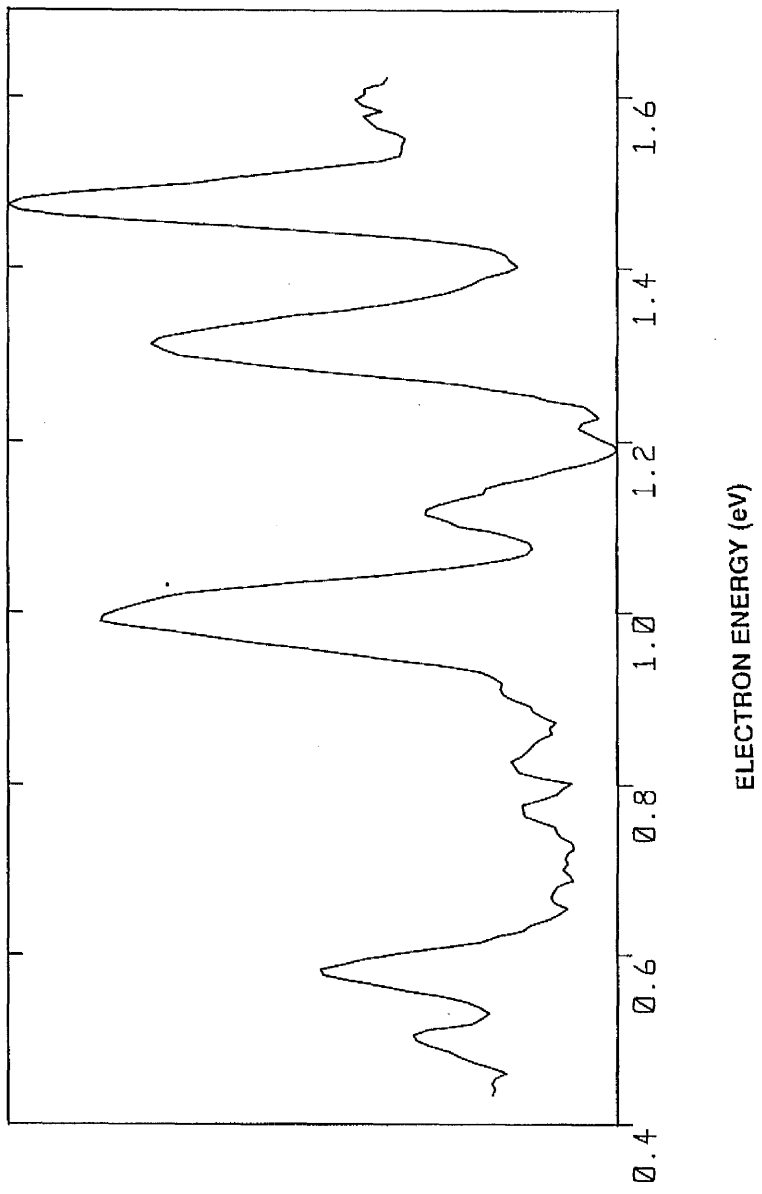

achieved by summing all electron intensities measured at the same kinetic energy, over the complete range of photon energies. The structure due to molecular photoelectron lines can be masked prior to summation, but in the data presented here it has conveniently averaged out to reveal the features with constant kinetic energy.

A detailed analysis of autoionisation processes has been performed through photoelectron studies of O_2 at the Daresbury synchrotron [62][63]. Electron emission from autoionising levels of atomic nitrogen has been observed in collision of fast neutral 1^1S Helium with N_2, NO and N_2O molecules [64]. Although peaks due to molecular ionisation by He metastables covered all but two autoionising levels in the case of N_2, the results from NO and N_2O were unobscured and well resolved. Peaks due to autoionisation of oxygen atoms were recognised from previous studies of O_2 by the same author [65]. More recently, several autoionising levels have been observed in collision of atomic Nitrogen with rare gases [66].

The lowest lying levels of N^+ have a configuration $2s^22p^2$ with the ground state ^3P at 14.549eV and excited ^1D and ^1S states at 16.44 and 18.59eV with respect to the ground state of N. The autoionising states giving electron emission peaks observed in the present work are Rydberg states converging on ^1D.

The energies and assignments are summarised in table 7(f) where they are seen to be in good agreement with the energies from the other authors discussed above.

Table 7(f)

Electron energies and state assignments for the structure due to atomic autoionisation in figure 7.6. The state energies can be obtained by adding the ground state ionisation potential (14.549eV) to the electron energies. The energies under Moore[1] are extrapolated from the Rydberg states of lower n. All energies are in eV.

Present work	Assignment	Cermák	Boumsellek and Esaulov	Moore[1]
0.503	$2s2p^4\ ^2D$			0.493
0.581	$^1D4p\ ^2D$	0.58	0.599	(0.677)
0.994	$^1D5s\ ^2D$	0.96	0.986	(0.990)
1.016	$^1D4d\ ^2F$	1.01	1.017	(1.021)
1.116	$^1D5p\ ^2D$	1.12	1.155	(1.132)
1.312	$^1D6s\ ^2D$	1.31	1.327	(1.325)
1.473	$^1D7s\ ^2D$	1.49	1.485	(1.495)

[1]Moore C, **1974** Atomic Energy Levels NBS circular **476**
(Washington DC: US Govt. Printing Office)

7.5 Conclusion

In this study the near threshold PES has been compared to spectra taken at fixed photon energies. The intensities, as expected, were found to be significantly different. The high resolution of the near threshold PES, obtained with the two-dimensional scanning technique, has revealed many new vibrational bands and created a new challenge for more detailed theoretical studies. The predicted energies of the recent ADC(4) study of Tomasello [44] have, however, shown an encouraging general consistency with the experimental results of this study.

Tentative assignments have been made of several vibrational bands in the higher binding energy region of the spectrum, where there is a breakdown of the molecular orbital picture of ionisation. Although some support for these assignments has been found in work by Sambe and Ramaker [59], it is in this region that more detail including vibrational information is most needed from future theoretical studies.

CHAPTER EIGHT

PHOTOELECTRON STUDY OF CARBON MONOXIDE

8.1 Introduction

Previous photoelectron studies of Carbon Monoxide have used X-ray photons [48], He II photons at 40.18eV [51][38] and synchrotron radiation [67]. The recent electron momentum spectroscopy (binary (e,2e)) study of French et al [68] has provided extra information on the ionisation process. The complexity of this process is due to electron correlation effects which can cause single or multiple excitations to accompany the ionisation.

These correlation effects have stimulated a variety of theoretical studies using both Configuration Interaction (CI) [43][69][70] and Green's function methods [45][56][71]. They are also the main subject of the present investigation into the photoionisation of Carbon Monoxide.

8.2 Experimental

In this study the same method of data collection has been employed as for the N_2 study above. The Toroidal Grating Monochromator (TGM sect.2.3.2) was used to obtain a collection energy range 2D spectrum (sect.5.6.2) with electrons of 0.2 to 2.0eV being accepted over photon energies stepped by 6meV from 23 to 43eV.

In the section of this 2D spectrum shown in figure 8.1 the vertical lines indicate that some atomic autoionisation has taken place along with the

Figure 8.1
The Collection Energy Range 2D spectrum of CO. Photoelectron yield is represented by colour with the highest intensity black. The diagonal lines are due to molecular photoionisation and the vertical lines due to atomic autoionisation.

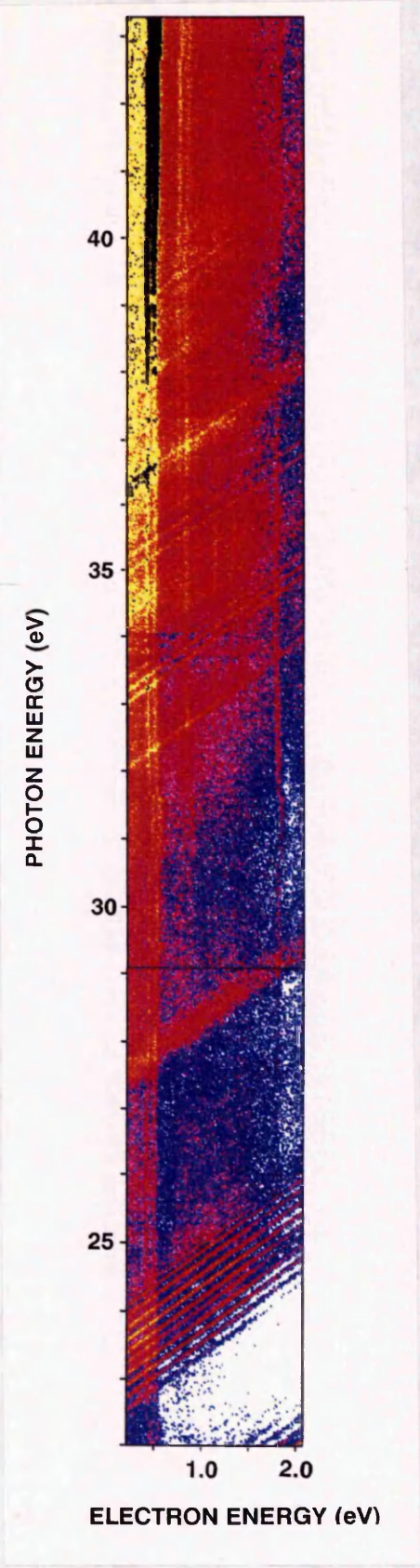

molecular photoionisation.

After the necessary corrections and calibrations (sects. 5.7 & 5.8) have been applied to the data a near threshold photoelectron spectrum (NTPES) and a kinetic energy spectrum have been obtained. The method used to produce these spectra has been described above in the case of nitrogen (sect.7.2). The NTPES has 60meV resolution and is shown in figure 8.2 along with a PES taken at a fixed photon energy of 45eV. The features of atomic autoionisation are shown in the kinetic energy spectrum of figure 8.3.

Several PES's were taken at fixed photon energies, some of which are presented in figures 8.4 and 8.5 to show how the relative intensities of features vary as a function of photon energy.

8.3 The Satellite Spectrum of Carbon Monoxide

8.3.1 Introduction

The ground state configuration of CO can be expressed, using the LS coupling scheme, as

$$(1\sigma)^2(2\sigma)^2(3\sigma)^2(4\sigma)^2(1\pi)^4(5\sigma)^2 \quad {}^1\Sigma^+$$

The three lowest energy states of CO^+ can be considered in the independent particle model as ionisation from the 5σ, 1π and 4σ molecular orbitals. They are assigned as $X^2\Sigma^+$ (at 14.018eV), $A^2\Pi$ (at 16.536eV) and $B^2\Sigma^+$ (at 19.688eV) respectively.

Figure 8.2
The Near Threshold Photoelectron spectrum of CO shown with a photoelectron spectrum taken at 45eV photon energy.

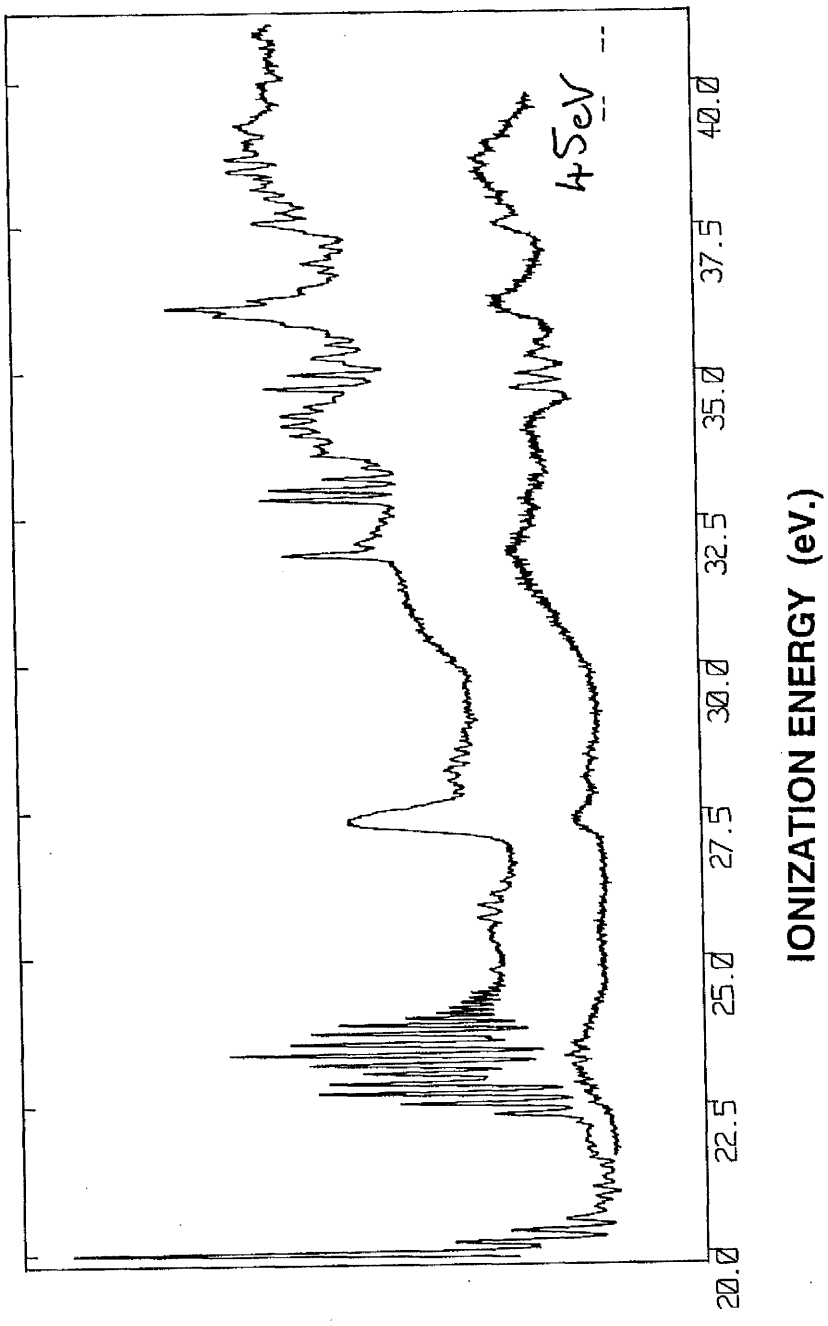

Figure 8.3
The constant kinetic energy spectrum of CO. Obtained fom the summation of the CE2D spectrum (figure 8.1).

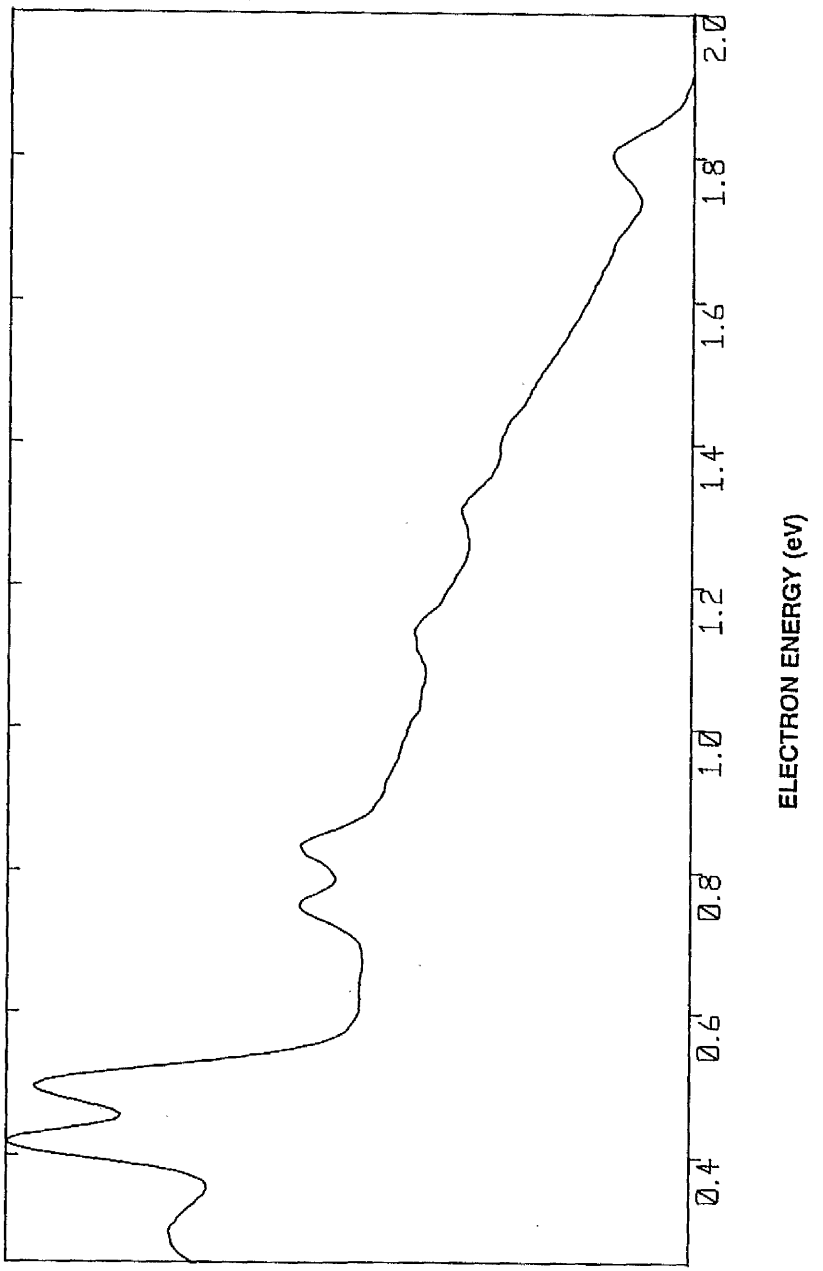

Figure 8.4
Photoelectron spectra of CO taken at successively increased photon energies to show the variation in dominance of spectral features.

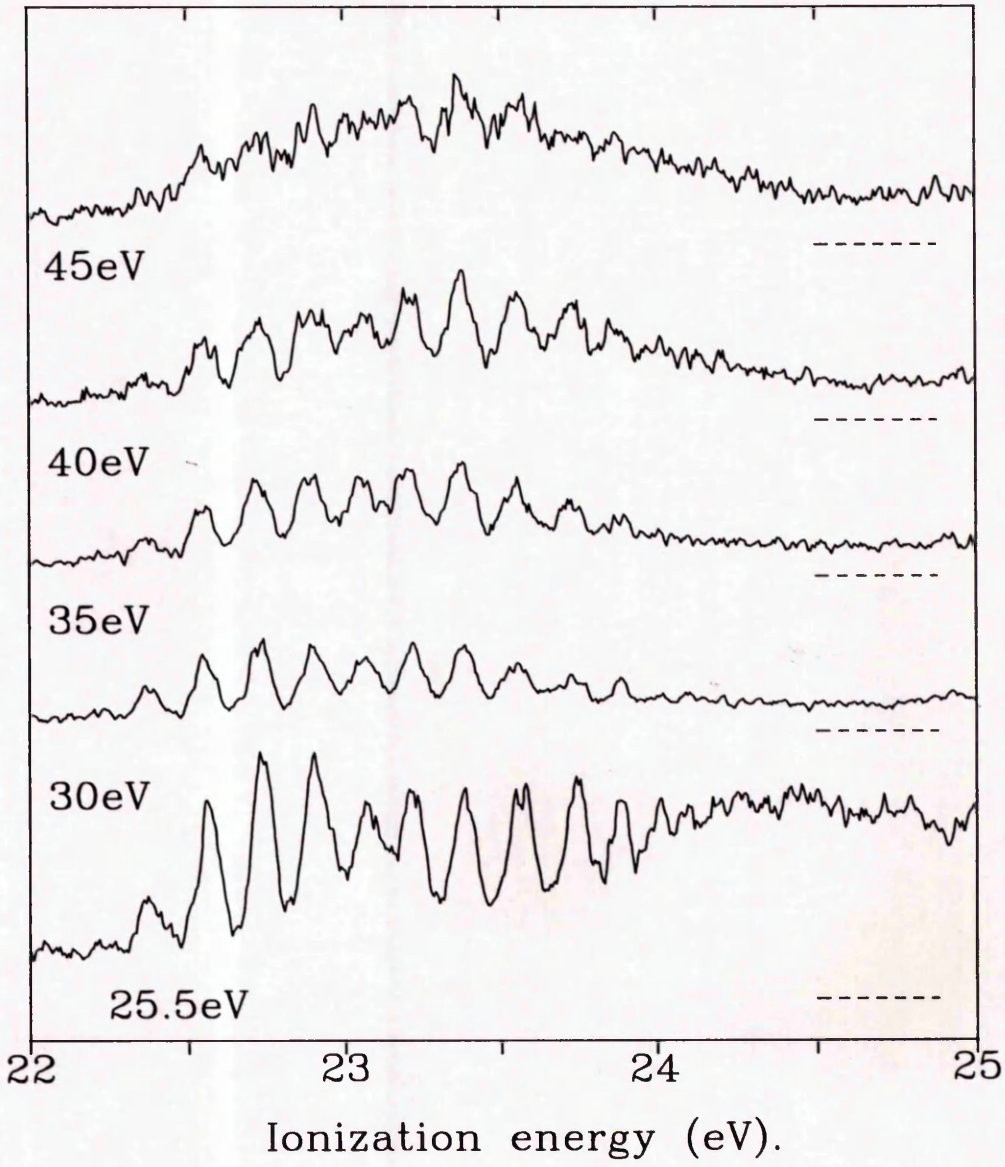

Figure 8.5
Photoelectron spectra of CO taken at successively increased photon energies to show the variation in dominance of spectral features.

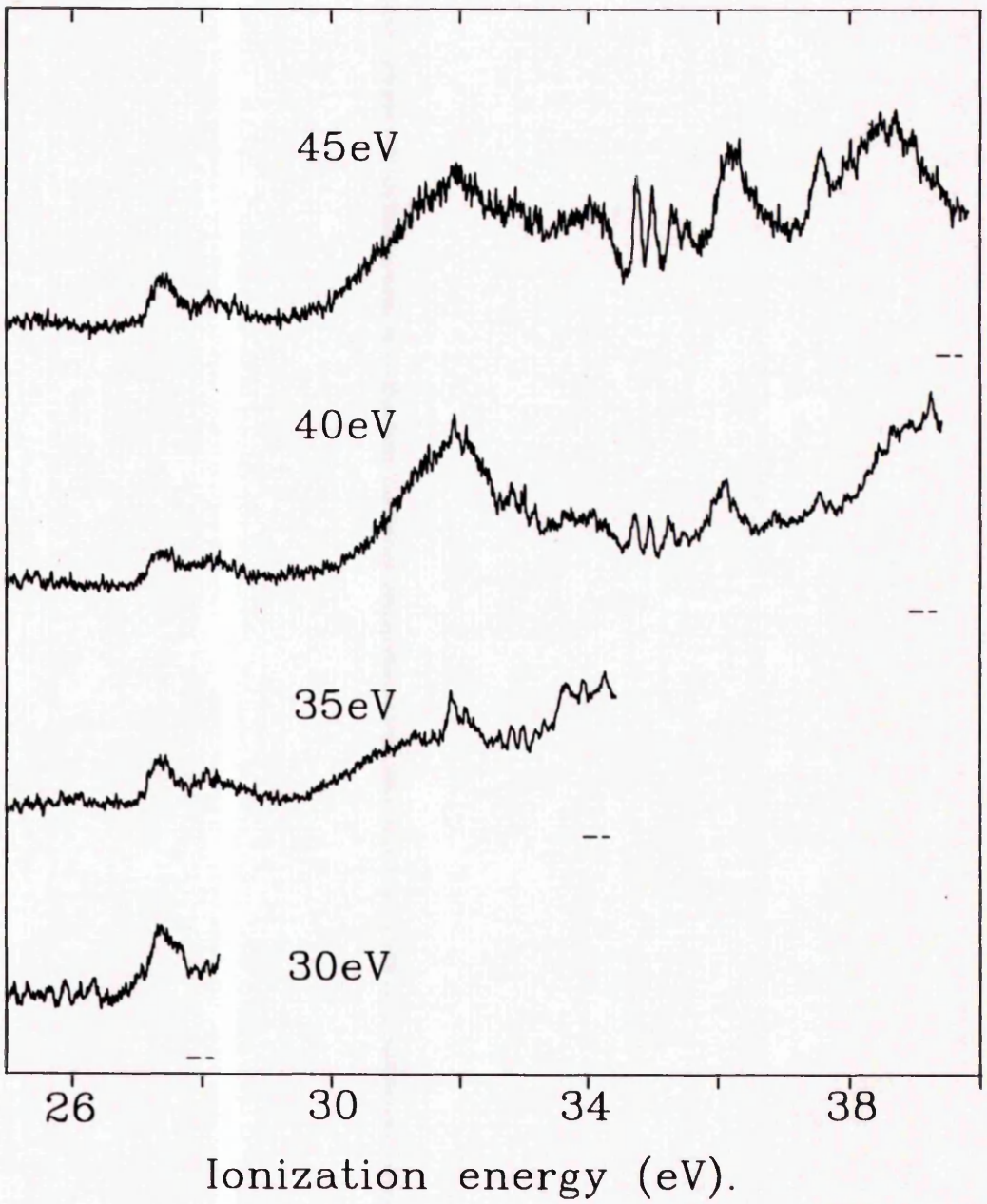

As in the nitrogen case, this simple picture of ionisation is disrupted by electron correlation effects. Excitations of the ion accompany electron emission and produce satellite lines in the spectra. Below about 30eV these lines can be easily classified by the excited electron configurations of the ion that produced them. At higher binding energies, where ionisation of deeper valence orbitals allows access to a higher number of excited configurations of the ion, the spectrum is more complex. This is the situation for ionisation of the inner valence electron from the 3σ orbital in the 30-45eV energy region of the CO spectrum. The intensity of lines in this region is so well distributed that it is impossible to distinguish main from satellite lines and there is said to have been a severe breakdown of the molecular orbital picture of ionisation.

Assignment of the ion states of Carbon Monoxide is more complicated than for many other molecules because three of the four valence orbitals, the 3σ, 4σ and 5σ, are of the same symmetry and mixing may occur.

Photoionisation spectra have been obtained by Krummacher et al [67] using monochromatic synchrotron radiation at the Laboratoire pour Utilisation du Rayonnement Electromagnetique (LURE) in Orsay, France. After comparison with the Green's functions calculations of Langhoff et al [43] and Schirmer and Walter [45], Krummacher et al concluded that the structure between 22-25eV was due mostly to 4σ and 5σ ionisation, the features between 25-30eV were predominantly from the $(1\pi)^{-1}$ process and the structure above 30eV was attributed mainly to the $(3\sigma)^{-1}$ ionisation process.

8.3.2 Calculations.

There has been considerable theoretical interest in CO because of its small size, linear geometry and heteronuclear character. In addition, CO has attracted interest due to the sign of its small dipole moment, which is only correctly predicted to be negative on the carbon end when electron correlation is included in the calculations.

The Configuration Interaction (CI) study of Langhoff et al [43] has provided a comparison with the experimental energies for CO. The energies used for normalisation are at the vertical transitions $X^2\Sigma^+$ v=0 (14.018eV) and $A^2\Pi$ v=2 (16.910eV) corresponding to the respective peaks of the Franck-Condon distributions. The 3h-2p configurations in the POLCI calculations were obtained by considering an occupied 2π orbital in the neutral molecule, thereby including initial state correlation. Both SECI and POLCI results are presented in table 8(a).

There have been a number of Green's Functions calculations [43][45][58][71] of the satellite states of CO. French et al [68] have made a detailed comparison of these, and CI calculations, with their own electron momentum spectroscopy (binary (e, 2e)) results. Although most calculated peak positions required a shift of 2-4eV towards lower binding energy, the Green's functions calculations of Schirmer and Walter [45] best described the (e, 2e) work and their results have been presented here in table 8(b).

Table 8(a) Vertical-electronic ionisation energies and pole-strengths* from the configuration interaction results of Langhoff et al [43]. SECI results are positioned above POLCI results in each row.

Symmetry	$^2\Sigma^+$			$^2\Pi$
Energy(eV)	$3\sigma^{-1}$	$4\sigma^{-1}$	$5\sigma^{-1}$	$1\pi^{-1}$
14.02 14.02		0.004	0.899 0.878	
16.91 16.91				0.920 0.849
18.89 $ 20.20		0.853 0.774		
24.46 25.37	0.011 0.004	0.028 0.039	0.021 0.016	
26.35				0.004
28.72				0.003
31.19 31.18				0.006 0.005
31.72 32.36	0.006 0.037	0.008 0.004	0.013 0.017	
34.28 33.76	0.065	0.018	0.008	
33.87				0.010
34.98	0.008			
35.08	0.204	0.005		
35.99				0.003
36.05 36.29	0.020		0.008	

$ The experimental value for the $^2\Sigma^+$ v=0 state is 19.688eV.

*Only pole strengths greater than 0.003 are shown. **....continued**

Table 8(a) continued

Symmetry	$^2\Sigma^+$			$^2\Pi$
Energy(eV)	$3\sigma^{-1}$	$4\sigma^{-1}$	$5\sigma^{-1}$	$1\pi^{-1}$
36.81				0.004
36.88 37.32	0.005 0.005			
37.08 37.38				0.003 0.010
37.97 38.06	0.094	0.015		
38.15	0.104			
38.33 38.30				0.010 0.008
38.77 38.63	0.116			
39.12 39.41	0.241 0.004		0.007	
39.53 39.64	0.013 0.090			
39.74	0.043			
40.34	0.029			
40.64 40.44	0.032 0.124	0.016		
41.12 41.15	0.010 0.025	0.003		
41.32 41.41	0.025 0.178		0.004	

Table 8(b) (Ext.2pTDA) Greens Function calculations of CO^+ [45].
[1]also has contribution from 3σ. [2]also has contribution from 4σ.
[3]may arise due to initial state correlation.

Symmetry	Orbital	Energy(eV)	Pole Strengths	Leading config's
$^2\Sigma^+$	5σ	13.97	0.89	$5\sigma^{-1}$
$^2\Pi$	1π	16.99	0.90	$1\pi^{-1}$
		22.98	<0.01	$5\sigma^{-2}2\pi$
		28.75	0.01	$4\sigma^{-1}5\sigma^{-1}2\pi$
$^2\Sigma^+$	4σ	20.11	0.79	$4\sigma^{-1}$
		22.99	0.11[1]	$5\sigma^{-1}1\pi^{-1}2\pi$
		29.81	<0.01	
	3σ	33.82	0.06[2]	$5\sigma^{-2}6\sigma$
		34.08	0.08[2]	$4\sigma^{-1}5\sigma^{-1}6\sigma$
		35.12	0.01	$3\sigma^{-1}$
		37.75	0.02	
		38.34	0.01	
		38.57	0.04	$5\sigma^{-2}n\sigma$
		39.01	0.18	$4\sigma^{-1}5\sigma^{-1}n\sigma$
		39.23	0.01	$5\sigma^{-1}1\pi^{-1}n\pi$
		39.44	0.28	$3\sigma^{-1}$
		39.89	0.05	
		40.13	0.03	
		40.26	0.02	
		40.42	0.01	
		40.83	0.02	
		41.67	0.01	
		41.76	0.02	
$^1\Delta$	1δ[3]	21.91	<0.01	$5\sigma^{-1}1\pi^{-1}2\pi$
		24.57	<0.01	$5\sigma^{-1}1\pi^{-1}2\pi$

8.3.3 The 20-30eV Binding Energy Range

This part of the NTPES, shown in figure 8.6, is dominated by a strong vibrational progression at around 23.5eV and a broad featureless state centred at 27.35eV. The experimental assignments and energies of the spectral features in this binding energy region have been listed in table 8(c).

Previous observation of the vibrational series at around 23.5eV by Asbrink et al [38] using He II photons revealed 13 peaks. The vibrational intensity distribution, spacings and peak asymmetries suggest that there are two states in this energy region. These have been assigned by Asbrink et al as vibrational levels of the $D^2\Pi$ (22.73eV) and $C^2\Sigma^+$ (23.38eV) states.

In the present work 19 peaks have been observed, with considerable anharmonicity for the higher vibrations (see table 8(c)). The features at 22.945eV and 23.640eV (figure 8.7) support the alternative assignment that this is a single vibrational series being perturbed by a much weaker state between 22.9 and 23.7eV. The calculated pole strengths of Schirmer and Walter [45] (table 8(b)) lend further support to this argument with the only significant contribution at 23.99eV from the 4σ orbital, and a much weaker pole-strength at a similar energy associated with the 1π orbital. The assignments of these states are $(5\sigma)^{-1}(1\pi)^{-1}(2\pi)\ ^2\Sigma^+$ and $(5\sigma)^{-2}(2\pi)\ ^2\Pi$, and they are associated with the 4σ and 1π orbitals respectively.

The CI results of table 8(a) seem to be 1-2eV too high as there is no significant intensity observed between 25 and 26.5eV in the spectra of low or high photon energies.

The band between 24.75 and 26.75eV was also observed by

Figure 8.6
The 20-30eV region of the Near Threshold Photoelectron Spectrum (NTPES) of CO.

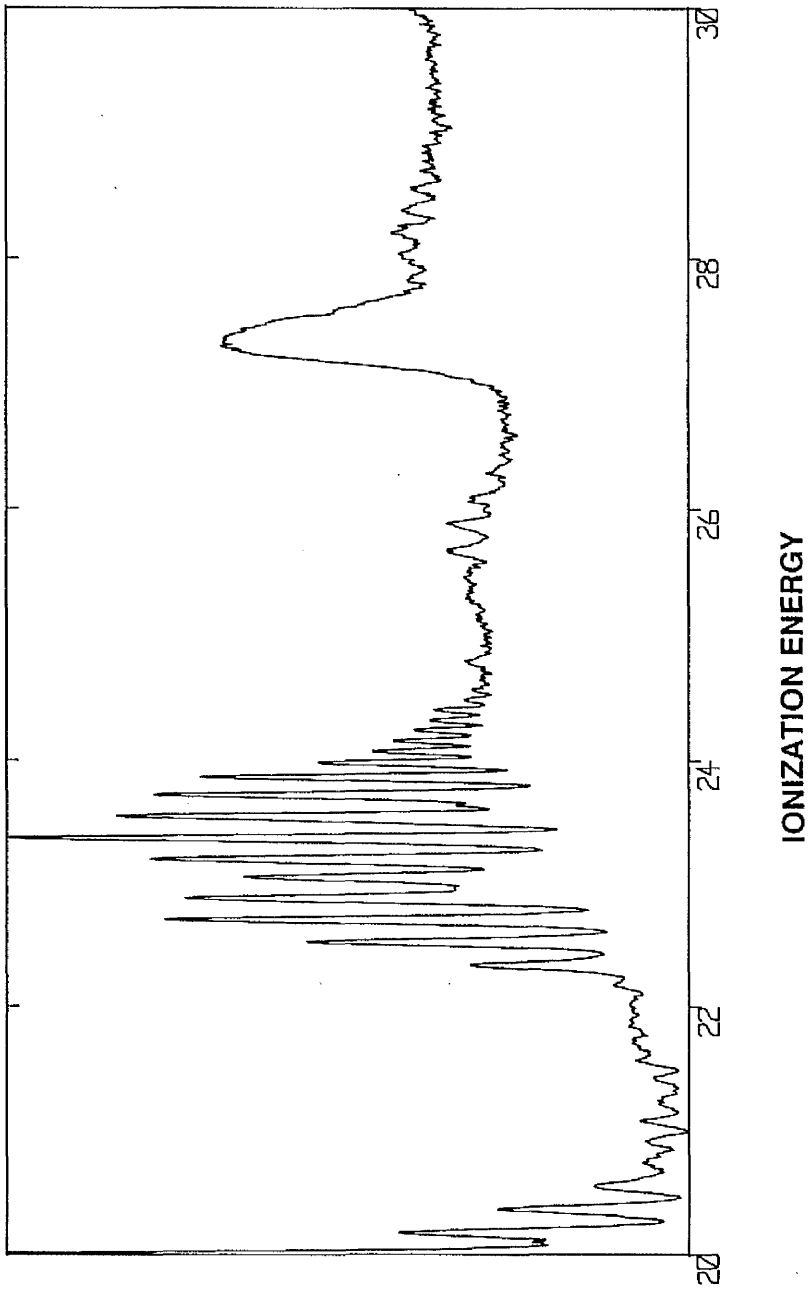

Table 8c:

Experimental Energies of the CO^+ Satellite States

Energies (eV) From NTPES	Assignments/* orbital/ configurations
22.182 v=1#	$D^2\Pi$?
22.335 v=2	1π orbital
22.522 v=3	$(5\sigma)^{-2}(2\pi)$
22.698 v=4	
22.871 v=5	
23.041 v=6	
23.188 v=0	
23.360 v=1	
23.544 v=2	
23.722 v=3	
23.868 v=4	
24.076 v=5	$C^2\Sigma^+$?
24.161 v=6	4σ orbital
24.244 v=7	$(5\sigma)^{-1}(1\pi)^{-1}(2\pi)$
24.323 v=8	
24.404 v=9	
24.483 v=10	
24.563 v=11	
22.945	
23.085	
23.225	
23.363	
23.501	
23.640	
24.784 v=0	$E^2\Sigma^+$? [1]
24.964 v=1	
25.144 v=2	$^2\Pi$? [2]
25.308 v=3	
25.472 v=4	$^1\Delta$? [3]
25.671 v=5	
25.887 v=6	
26.091 v=7	
26.317 v=8	
26.521 v=9	
27.35 (broad peak 27.15-27.65)	$^2\Pi$
27.843	$^2\Sigma^+$
28.030	4σ orbital
28.214	
28.394	
28.566	
29.80 (repulsive state)	$^2\Pi$

Refer to page 139 for footnotes.

Figure 8.7
The 22-25eV region of the Near Threshold Photoelectron Spectrum (NTPES) of CO. Note the features at 22.945 and 23.640eV.

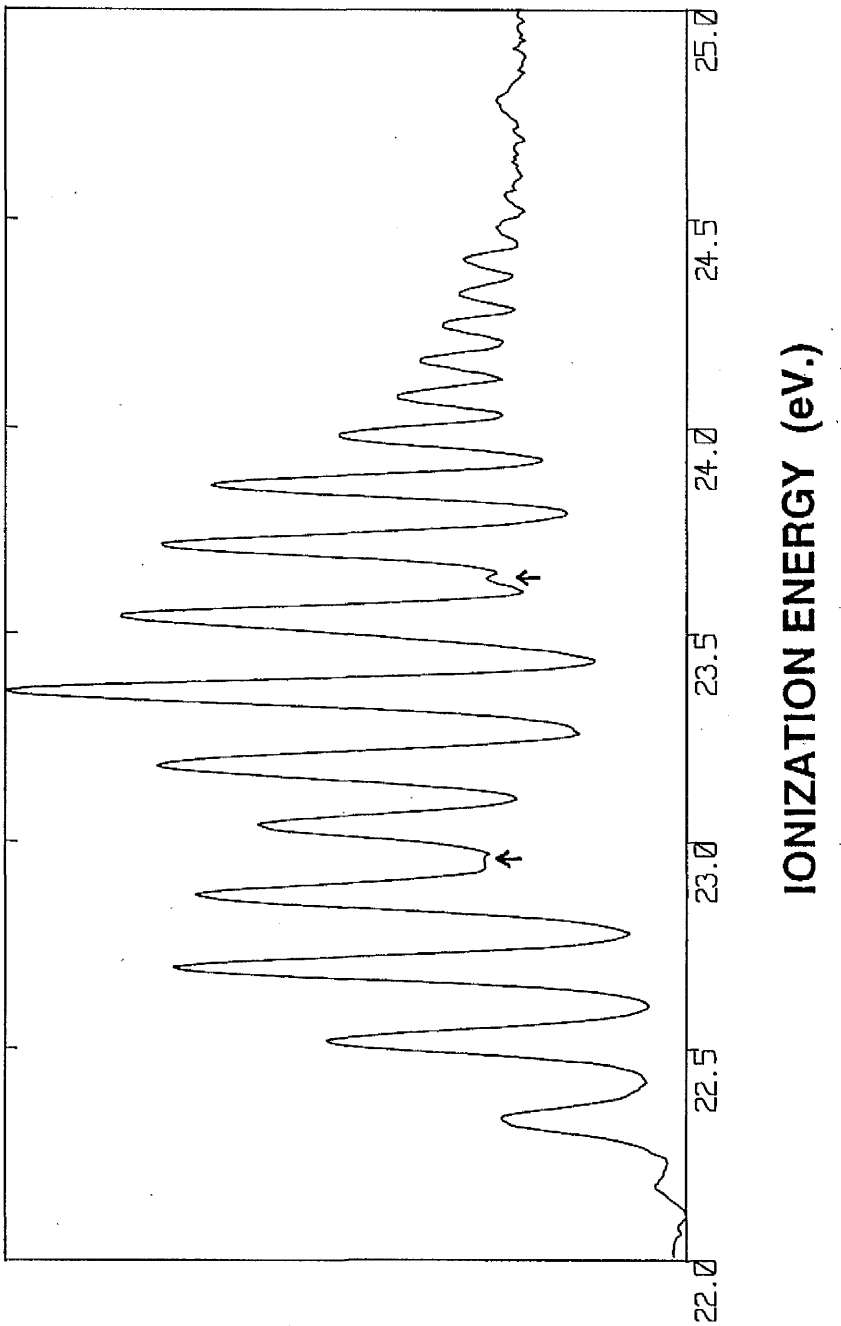

Asbrink et al [38] and assigned by them as $E^2\Sigma^+$. The broad features between 25 and 25.5eV suggest predissociation of this vibrational progression which cannot be easily assigned from the theoretical studies. The 2ph-TDA study of Schirmer and Walter gives a $^1\Delta$ state at 24.57eV as a consequence of initial state correlation, whereas the POLCI calculation suggests a $^2\Pi$ state at 26.35eV. Although there is no real consensus in the theoretical studies for this state, the analysis of Yousif et al [72] also suggests a $^2\Pi$ assignment.

The broad feature centred at 27.35eV is about 0.5eV wide, although there is some indication of a shoulder on the high energy side. Following this feature is a vibrational progression centred around 28.25eV and extending up to 28.75eV. In the analysis of Yousif et al [72] these are two separate states with a repulsive $^2\Pi$ state at 27.4eV and a $^2\Sigma^+$ state at 27.9eV. The CI and Green's functions results of tables 8(a) and (b) only show weak pole-strengths for a $^2\Pi$ state at 28.7eV. French et al [68] have indicated in their (e, 2e) work that the states in this energy region can only be due to 4σ and 1π orbitals. The vibrational spacing of the 28.25eV state has been found in the present work to be similar to that of the 23.5eV $^2\Sigma^+$, which lends support to the assignments of Yousif et al.

Clearly, if the theory is to resolve these assignments, more detailed calculations with vibrational spacings as well as vertical transition energies are required. In addition, from this study and those of French et al [68] and Krummacher et al [67] it is clear that all the theories predict too little pole-strength in the region 25-29eV.

8.3.4 The 30-41eV Binding Energy Range

Figure 8.8 shows the NTPES over this binding energy range. At 29.80eV there is an apparent onset to a repulsive state which the CI results suggest is associated with the 1π orbital.A further state is observed at 31.862eV for which the CI study suggests $^2\Sigma^+$ symmetry, with contributions from the 3σ, 4σ and 5σ orbitals. The vibrational spacing of this state is similar to that of the state around 25.5eV, which, although the Franck-Condon distributions of the states are very different, lends support to the $^2\Sigma^+$ assignment of the lower energy state by Asbrink et al [38].

The strong vibrational series starting at 32.828eV in the NTPES is not present in the 50eV PES. There is no indication of this state in the theories of tables 8(a) and (b), but it has a similar vibrational spacing to the 23.5eV $^2\Sigma^+$ state which is also intense at NTPES conditions. It is therefore possible that this higher binding energy state is also due to the 4σ orbital, with $^2\Sigma^+$ symmetry. This state merges into another, with a similar vibrational spacing, extending from 33.5-34.5eV. The theoretical studies show some consensus on the assignment of this state as having $^2\Sigma^+$ symmetry mainly associated with the 3σ orbital, with some contribution from 4σ.

The intense series at 34.731eV can be seen in both the NTPES and the 50eV PES. The vibrational spacing (230meV) is significantly larger than previously discussed states. It is expected that this part of the spectrum will be dominated by the 3σ orbital with $^2\Sigma^+$ symmetry. However it is only the SECI results of Langhoff et al [43] which predict significant pole-strength in this energy region.

Figure 8.8
The high energy 30-41eV region of the Near Threshold Photoelectron Spectrum (NTPES) of CO.

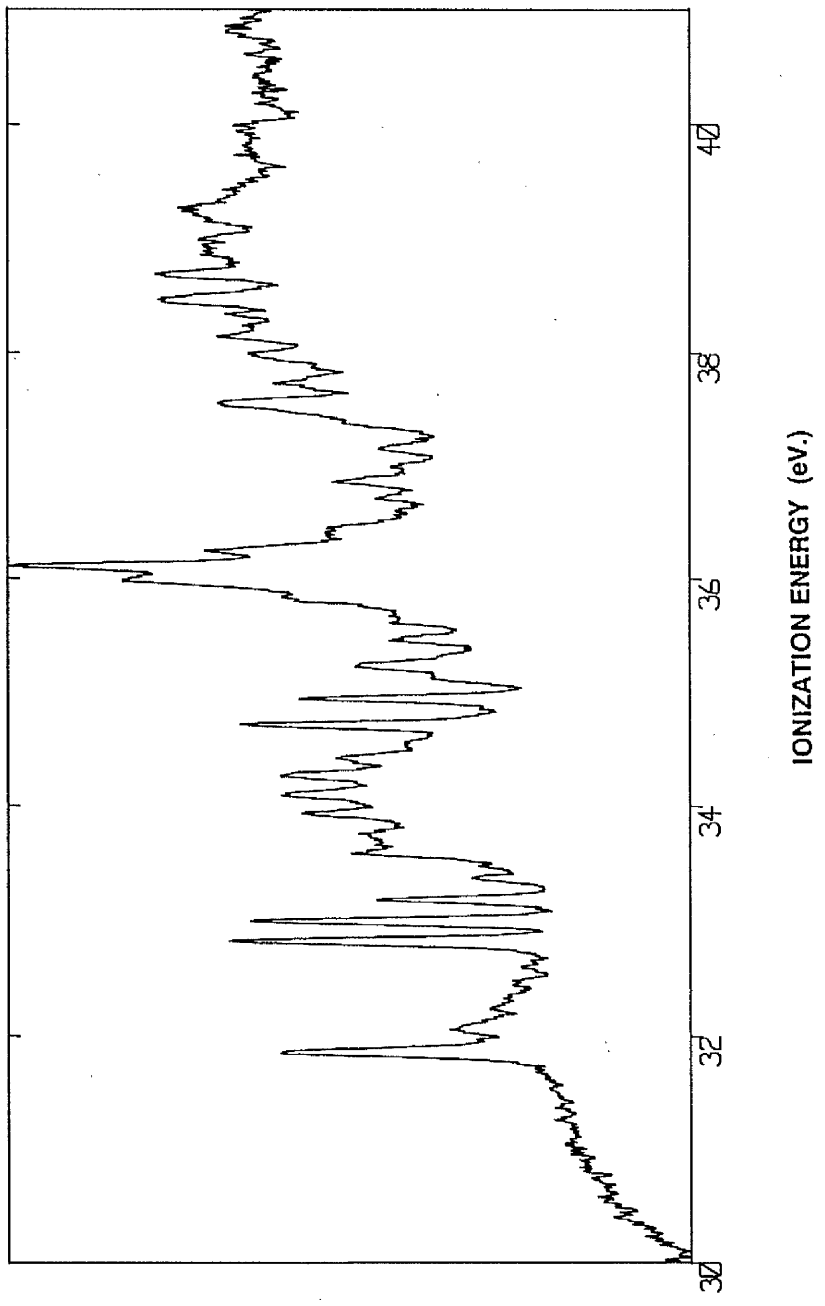

The remainder of the near threshold inner-valence photoionisation spectrum presents many well resolved satellite lines. Both CI and Greens function calculations suggest that these lines gain their intensity predominantly from $3\sigma^{-1}$ ionisation. Although any assignment of states would be entirely speculative, six vibrational bands have been suggested whose members have a similar spacing. These bands are shown in figure 8.9 and have been highlighted in table 8(d).

8.4 Atomic Autoionisation following Photodissociation of CO

The spectrum of constant kinetic energy features shown in figure 8.3 has been derived from the collection energy range 2D spectrum of figure 8.1. The origin of these features is the atomic autoionisation of excited oxygen following neutral photodissociation of CO:

$$h\nu + CO \rightarrow CO^* \rightarrow C + O^*$$

$$\downarrow$$

$$O^+ + e$$

The process of atomic autoionisation of oxygen has been thoroughly investigated previously by A.A.Wills et al [62] from the photodissociation of O_2. The results are presented in table 8(e) along with those from the present study.

8.5 Conclusion

In this study significant differences in intensity have been shown,

Figure 8.9
The high energy 32.5-38.5eV Binding Energy of the Near Threshold Photoelectron Spectrum (NTPES) of CO showing tentative assignments based on vibrational spacing.

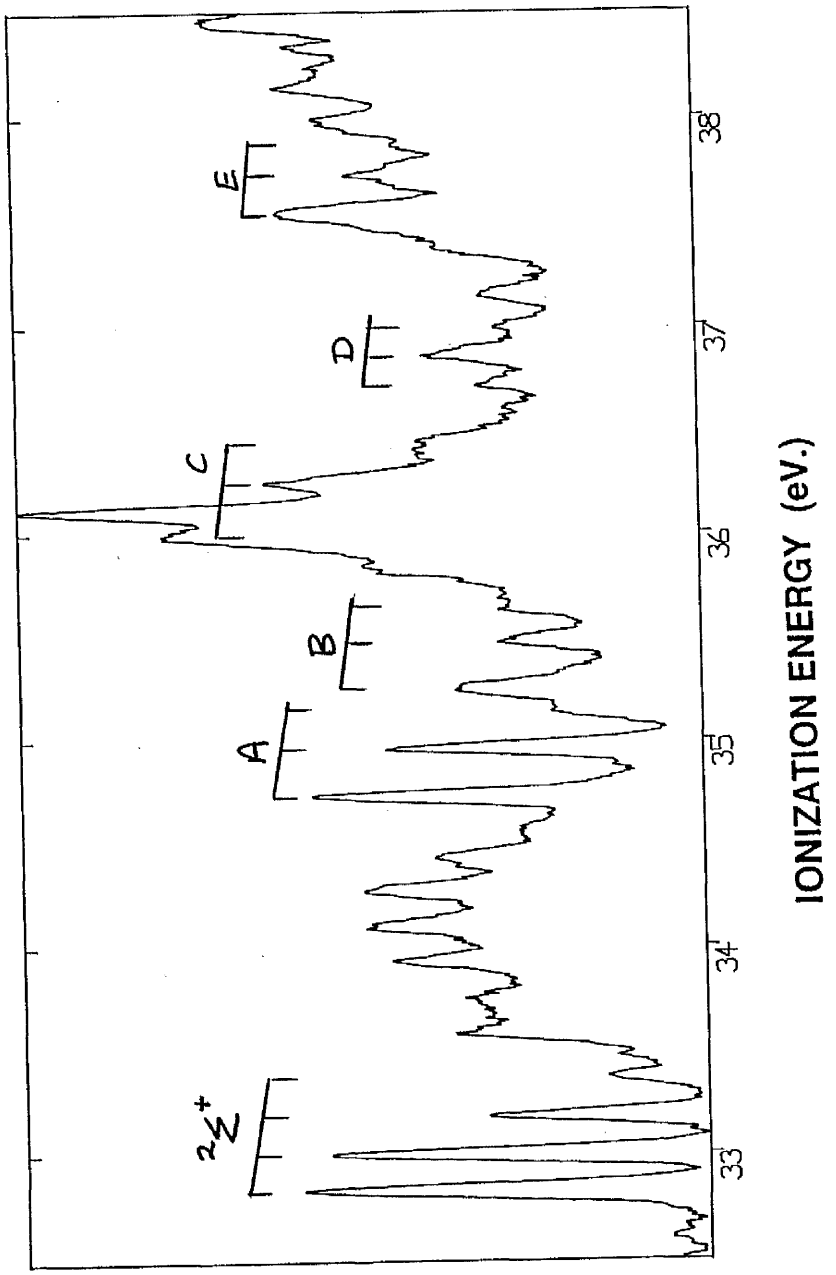

Table 8d:

Experimental Energies of the CO^+ Satellite States

29.80 (repulsive state)		$^2\Pi$
31.862	v=0	$^2\Sigma^+$
32.063	v=1	3σ/4σ/5σ mixing
32.263	v=2	
32.464	v=3	
32.828	v=0	$^2\Sigma^+$
33.003	v=1	4σ orbital?
33.191	v=2	
33.381	v=3	
33.598		$^2\Sigma^+$
33.769		3σ/4σ mixing
33.938		
34.107		
34.273		
34.422		
34.563		
34.726		A
34.964		A
35.150		A
35.254		B
35.482		B
35.651		B
35.827		
35.994		C
36.110		C
36.250		C
36.441		C
36.581		
36.721		D
36.861		D
37.000		D
37.157		
37.381		
37.551		
37.712		E
37.874		E
37.778		E
37.964		E
38.150		E
38.336		
38.522		
38.237		
38.462		F
38.687		F
38.870		F
39.137		

A further peak has been observed by Asbrink et al [1] at 22.039eV, which is presummed to be v=0.

* All assignments are tentative, as discussed in the text.

[1] Asbrink L, Fridh C, Lindholm E, Codling K 1974 Physica Scripta 10 183

[2] Yousif M, Ramaker DE, Sambe H 1983 Chem. Phys. Letts **101** 472
Langhoff PW, Langhoff SR, Rescigno TN, Schirmer J, Cederbaum LS, Domcke W, von Niessen W 1981 Chem. Phys. 58 71 (POLCI)

[3] Schirmer J and Walter O 1983 Chem Phys 201

Table 8(e)
The energy of the atomic autoionisation lines following photodissociation of CO, compared to the values from the study of autoionisation of atomic oxygen A.A. Wills et al [62].

O from O_2 [62] (eV)	**O from CO (this work)**
0.426	0.418
0.489	0.492
0.650	
0.748	0.749
0.830	0.832
1.104	
1.143	1.133
1.290	
1.310	1.311
1.412	1.414
1.480	
1.526	
1.557	
1.793	1.803

as expected, between the near threshold spectrum (NTPES) and photoelectron spectra taken at fixed photon energy. The high resolution of the NTPES, derived from the 2D scanning method, has revealed many new satellite lines. This has created a new challenge for more detailed theoretical studies, no one theoretical approach proving wholly consistent with this high resolution data.

The 2D data collection technique also ensures that the features due to molecular photoionisation are not confused with those due to atomic autoionisation. The latter have been confirmed by comparison with data from the photodissociation of O_2 [62].

CHAPTER NINE

PHOTOELECTRON STUDY OF HYDROGEN CHLORIDE

9.1 Introduction

Previous photoelectron studies of the valence ionisation of HCl using monochromatic synchrotron radiation include that of M.Y.Adam [73] which shows the breakdown of the molecular orbital picture. Cafolla et al [74] have used the Daresbury synchrotron source to investigate autoionisation in HCl.

Further insight into the ionisation processes has been provided by electron energy-loss [75] and (e-2e) [76][77] techniques.

Electron correlation effects adding to the complexity of the ionisation process have stimulated theoretical studies using Greens function calculations [78][79]. They are also the main subject of the present study.

9.2 Experimental

In this study the Toroidal Grating Monochromator (TGM sect.2.3.2) has been used to produce two Binding Energy Range 2D spectra (BE2D) (sect.5.6.2). The first BE2D spectrum has a binding energy range from 14.2eV to 17.4eV scanned over a photon energy range of 20eV to 23.9eV. This involved accepting electrons with a range of kinetic energy from 2.6eV to 9.7eV. The second BE2D spectrum covered a binding energy range of 12.4eV to 13.7eV over a photon energy range of 18.6eV to 30.0eV. The resulting

spectra, shown in figures 9.1 and 9.2 respectively, illustrate how this method of data collection produces vertical molecular photoionisation lines.

Two Collection Energy Range 2D spectra (CE2D) (sect. 5.6.2) of HCl have also been obtained using the TGM. The first, taken over a photon energy range of 26.5eV to 31.4eV and accepting electrons from 0.2 to 2.6eV is shown in figure 9.3. The diagonal molecular photoionisation lines indicate intense satellite structure, while the vertical lines at around 0.9eV electron energy suggest strong atomic autoionisation mechanisms at lower photon energies. This observation prompted the collection of the second CE2D spectrum. Electrons from 0.2 to 3.6eV were collected over a photon energy range of 21.5 to 26.6eV. The resulting spectrum, shown in figure 9.4 revealed many vertical atomic autoionisation lines of constant kinetic energy. In addition the first of the diagonal molecular photoionisation lines of figure 9.3 can be seen in the top left of this spectrum.

After the usual data corrections and calibrations (sect. 5.7 & 5.8) were applied to this data, a further correction had to be made to account for pressure variations of the target gas.

Due to gas handling difficulties a gradual reduction of the preset pressure in the target region had to be monitored. Data collection was paused periodically to reset this pressure. Thus a time dependent correction factor had to be applied to the data.

Since photon energy varied linearly with time, and the pressure variation over the collection period of a single slice of data was negligible, a photon energy dependent correction factor could be used. This factor was

Figure 9.1
The first Binding Energy Range 2D spectrum of HCl, showing the vertical constant binding energy lines. These are due to molecular photoionisation of the A-State of HCl.

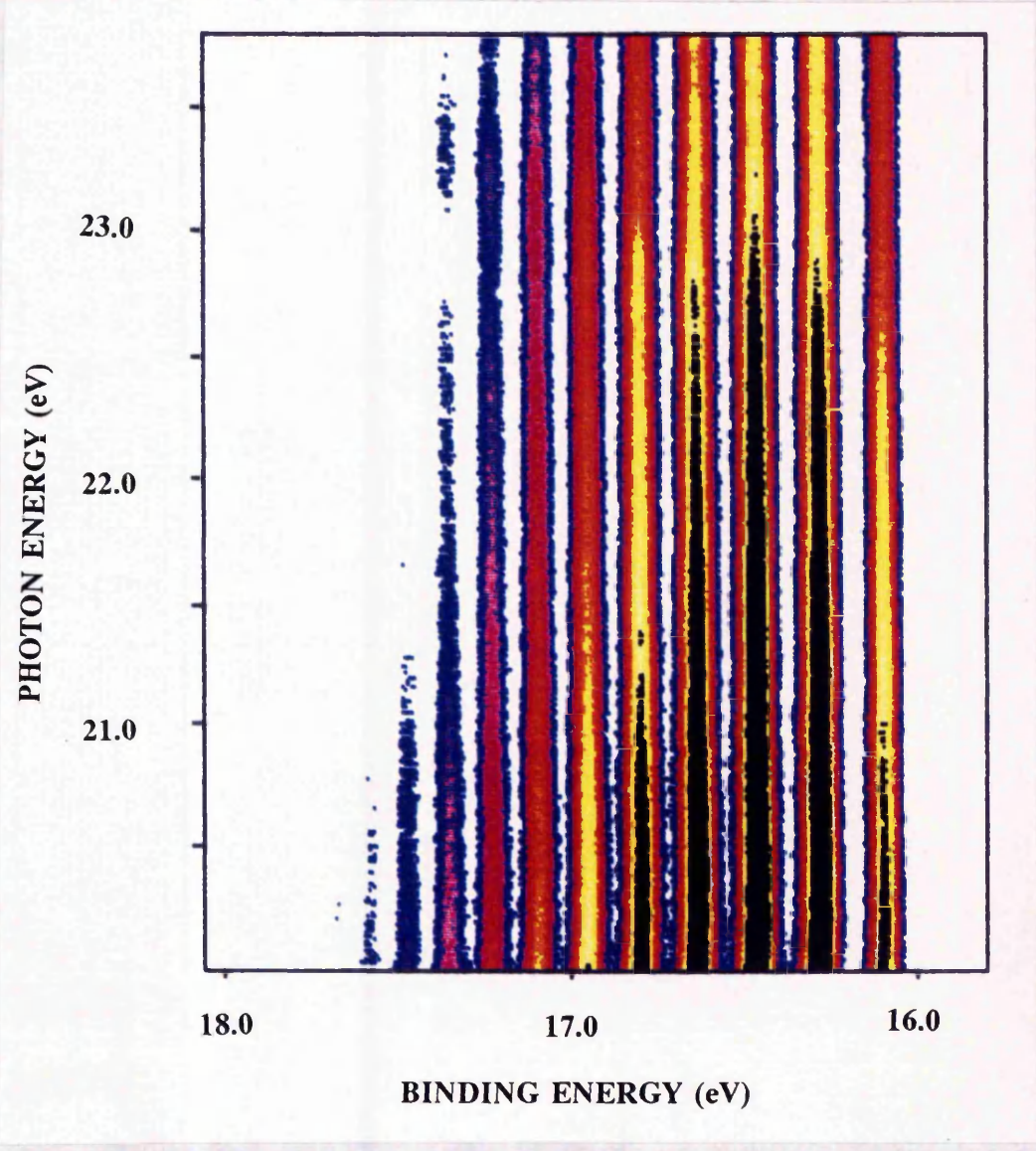

Figure 9.2
The second Binding Energy Range 2D spectrum of HCl, showing vertical constant binding energy lines due to molecular photoionisation of the X-State of HCl.

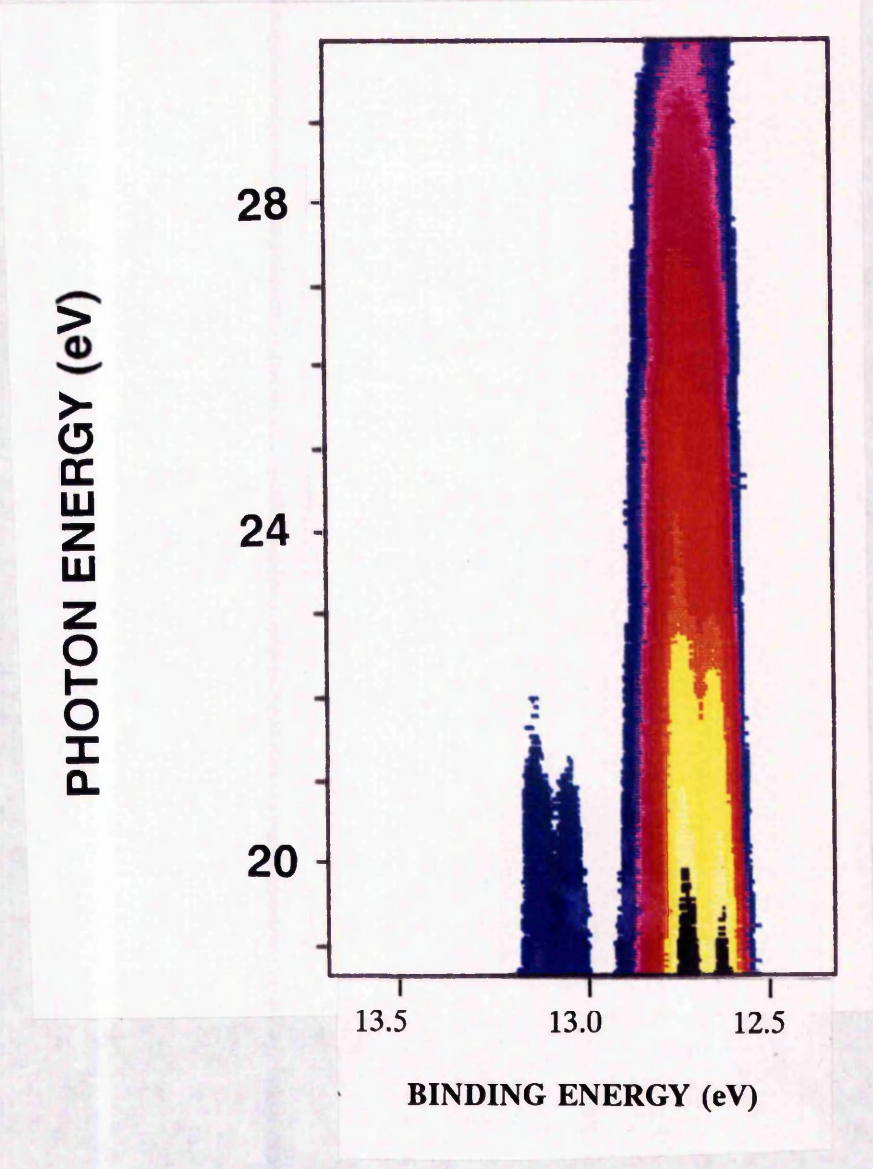

Figure 9.3
The first Collection Energy Range 2D spectrum of HCl, showing diagonal constant binding energy lines due to molecular photoionisation. There is also some indication of strong constant kinetic energy features at the lower photon energies, particularly around 0.9eV collection energy.

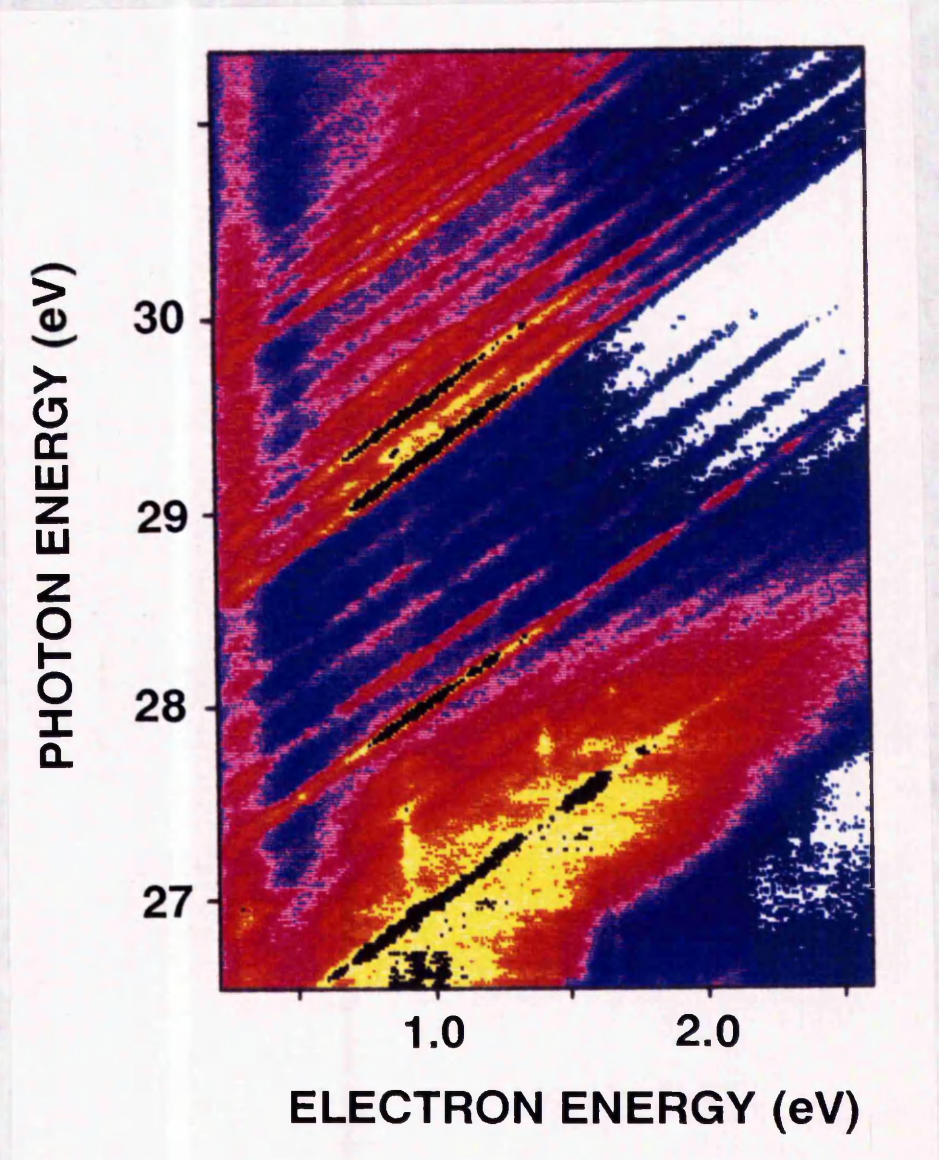

Figure 9.4
The second Collection Energy Range 2D spectrum of HCl, showing vertical constant kinetic energy lines due to autoionisation of atomic chlorine. The threshold of the lowest binding energy diagonal line in figure 9.3 can also be seen (top left). The vertical summation of this spectrum is also shown.

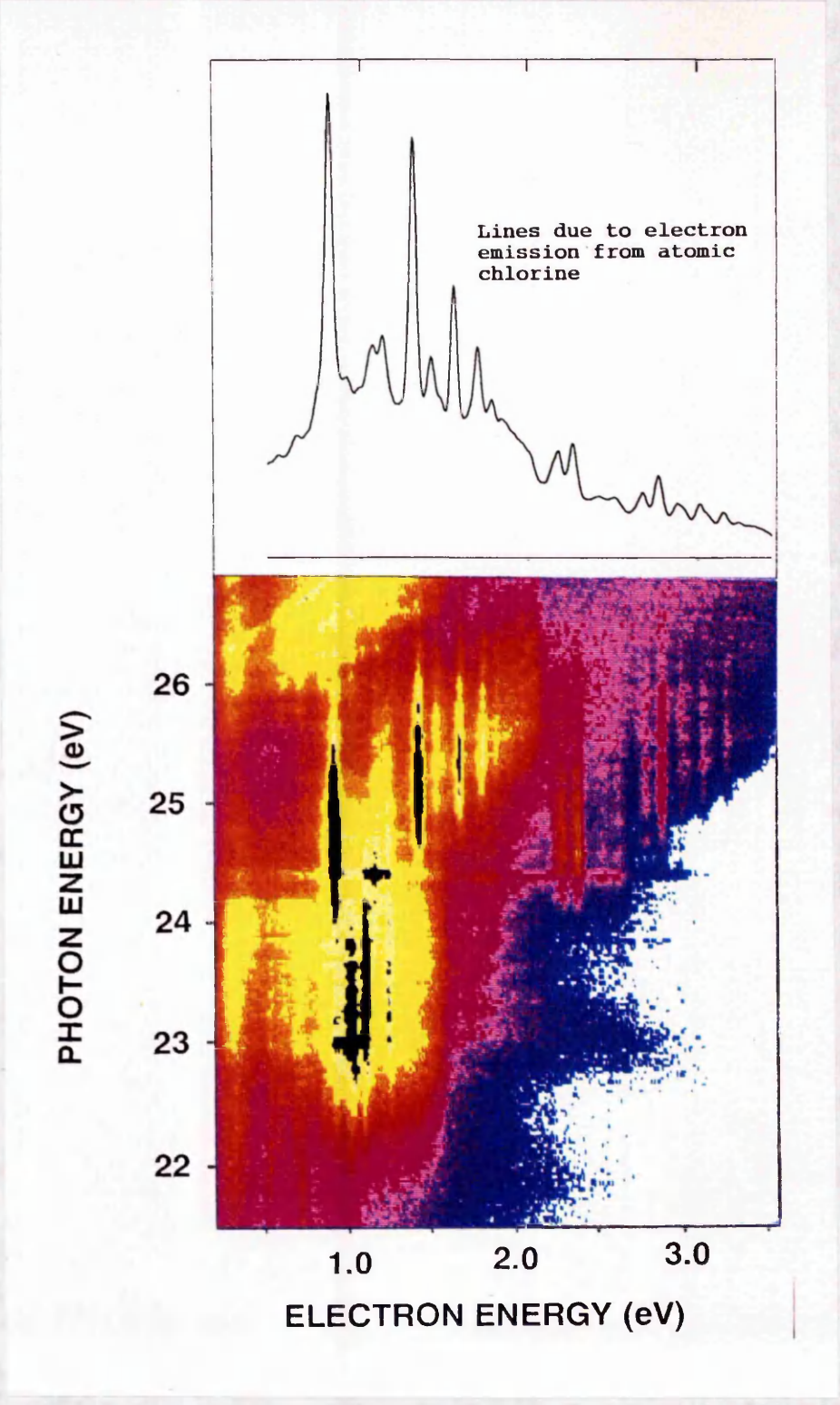

derived from the spectra themselves.

A vertical strip of electron intensities was defined from each spectrum in a region of least structural variation. These intensities were then summed in the horizontal, constant photon energy direction. The resulting photon energy dependent electron intensity curve showed the pressure variations and jumps clearly. After smoothing each section of gradual pressure reduction to remove any remnants of spectral features, the curve was used to correct the data.

9.3 The Satellite Spectrum of Hydrogen Chloride

9.3.1 Introduction

The ground state configuration of HCl can be expressed, using the LS coupling scheme, as;

$$\{(1\sigma)^2(2\sigma)^2(3\sigma)^2(1\pi)^4\}\ (4\sigma)^2(5\sigma)^2(2\pi)^4\ {}^1\Sigma^+_g$$

The two lowest energy states of HCl^+ are well described in the independent particle model as ionisation from the 2π and 5σ orbitals. The 2π orbital corresponds to a lone-pair and 5σ to a Cl-H bonding orbital. They have been assigned as $X^2\Pi$ and $A^2\Sigma^+$ respectively, with ionisation energies 12.75eV and 16.27eV found from photoelectron spectroscopic studies with HeI radiation [80].

The first inner valence shell ionisation spectrum of HCl was

obtained in 1980 by Brion et al [76] using (e, 2e) spectroscopy. Although resolution with this method was poor these results did demonstrate the complete breakdown of the molecular orbital model of ionisation in the 20-41eV binding energy region. Furthermore, observation of the maxima in the (e, 2e) momentum distribution suggested that all the structures above 20eV corresponded to transitions from an "s-type" orbital. Thus it seemed that the 4σ pole strength was split amongst a number of ion states.

A more recent (1986) study of the inner valence ionisation spectrum of HCl has been made by M.Y.Adam [73] using monochromatic synchrotron radiation. The increased resolution afforded by this method revealed seven bands where the (e, 2e) work found three.

Individual vibrations of the satellite bands were still not yet resolved, and it should be noted that each experimentally observed band may have contributions from satellite lines originating from different orbitals. Adam concluded that most of the observed bands obtain their intensity from $4\sigma^{-1}$ ionisation, but also, from measurements of the asymmetry parameter β, gave evidence that part of the structure might arise from outer valence, $5\sigma^{-1}$ and $2\pi^{-1}$ ionisation.

9.3.2 Calculations

In 1980, Suzuki et al [78] used Green's function calculations to achieve qualitative agreement with the valence ionisation spectrum of HCl obtained in the (e, 2e) spectroscopic study of Brion et al [76]. More recently (1989), Green's function calculations accurate to fourth order perturbation

theory (ADC(4)) have been used by W. Von Niessen and P. Tomasello [79] to achieve some quantitative agreement with the valence ionisation spectrum obtained by M.Y.Adam at the L.U.R.E synchrotron.

Von Niessen and Tomasello concluded that most intensity was gained from $4\sigma^{-1}$ ionisation with several satellite lines having a minor contribution from $5\sigma^{-1}$. Although small pole-strengths in the right energy range were also calculated for satellite lines originating from $2\pi^{-1}$, the authors found no need to use these in explaining the experimental spectra.

Having discussed from which orbitals they gain their intensity, Von Niessen and Tomasello looked into the character of the satellite bands. They concluded that none of the bands thus far observed could be characterised by a single ionic configuration, but listed several dominant ones: $(4\sigma^{-1}, 5\sigma^{-1})\ 5\sigma^{-2}\ n\sigma$ with n = 6-16, $2\pi^{-1}5\sigma^{-1}\ n\pi$ with n = 3-8, $2\pi^{-2}\ n\sigma$ with n = 6-15 and $2\pi_x^{-1}2\pi_y^{-1}\ n\delta$ with n = 1-3.

The ionisation energies and relative intensities produced by Von Niessen and Tomasello have been presented in table 9(a).

9.3.3 The 24-31eV Binding Energy Range

The Collection Energy range 2D spectrum of figure 9.3 has been summed in the diagonal, constant binding energy direction, to produce the near threshold photoionisation spectrum (NTPES) shown in figure 9.5.

The NTPES is dominated by a repulsive state centred on 25.9eV. This state is well predicted by Von Niessen and Tomasello at 25.88eV with high pole-strength originating from the 4σ orbital. Some intensity may also have

Table 9(a)
Calculated Ionisation Energies and Pole-Strengths of HCl computed by W Von Niesen and P Tomasello using ADC(4) calculations [79]

Ionisation Energies	Pole-Strengths
σ-symmetry	
23.28	0.143
25.88	0.397
27.94	0.036
29.34	0.010
30.53	0.043
31.55	0.006
π-symmetry	
27.57	0.005
29.10	0.010
29.34	0.003
31.12	0.006

Figure 9.5
The Near Threshold Photoelectron Spectrum (NTPES) of HCl, obtained by summation of figure 9.3. The assignments A to F have been highlighted.

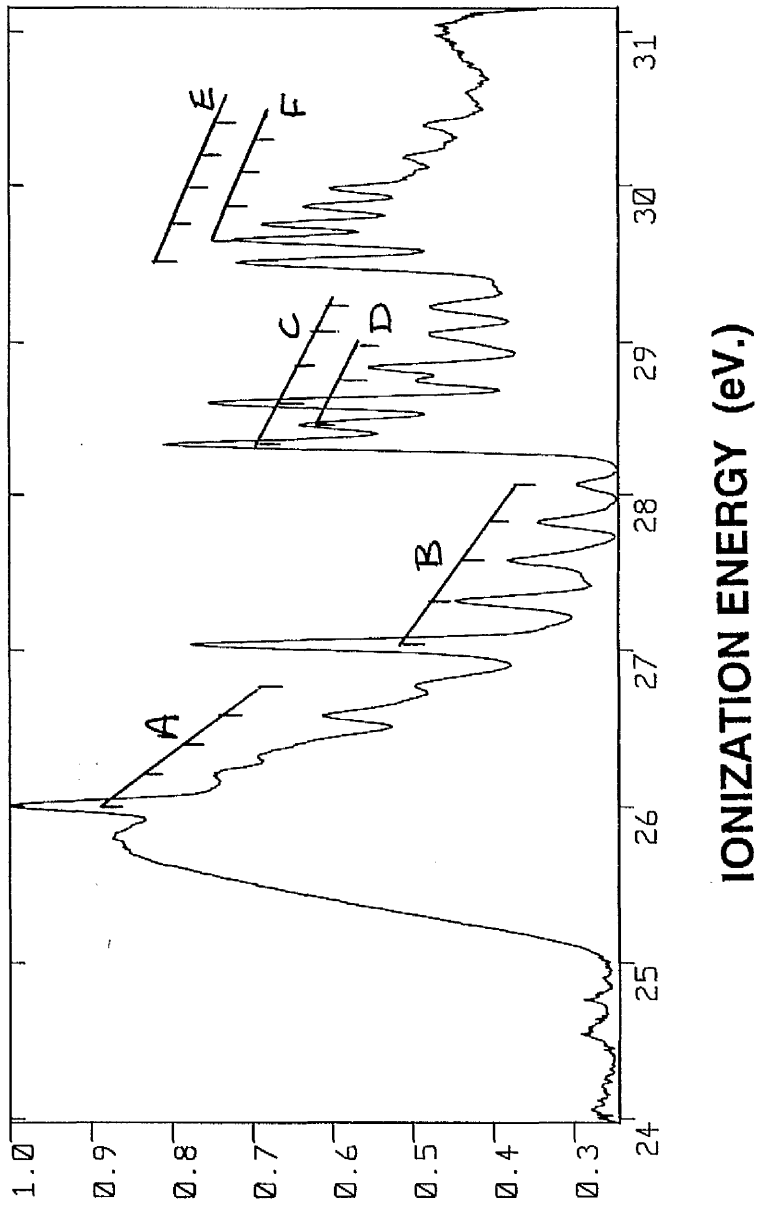

been borrowed from $5\sigma^{-1}$ ionisation as Von Niessen and Tomasello have summed these contributions in their results.

A dramatic increase in resolution in this work has enabled vibrational structure of the satellite bands to be resolved for the first time on the high energy side of the repulsive state. Six vibrational bands have been observed and labled A-F in figure 9.5. Their energies and vibrational constants are listed in table 9(b).

At first sight bands C and D, together with bands E and F, appear to be doublets. On closer inspection the spacing of peaks with corresponding vibrational quantum numbers (v) do not remain constant as v increases, suggesting that all bands A-F are different electronic states.

Double ionisation potentials observed in electron impact with HCl include 36.0 ± 0.8eV [81] and 35.5 ± 0.5eV [82]. These values are 1-2eV too high for any of the states A-F to be in the same Rydberg series.

In their comparison with the experimental values of Adam [73], Von Niessen and Tomasello [79] recognised the repulsive state, but showed no values corresponding to states A or B, which were not resolved by Adam. A calculated pole-strength at 27.94eV was attributed to a single peak observed by Adam at 28.5eV. This can be seen in the present work to be made up of the two states C and D. Finally, Von Niessen and Tomasello assigned two calculated states (29.34 and 30.53eV) to the single peak observed by Adam at 29.8eV, which has in fact been resolved into the two peaks E and F in the present study.

Although there appears to be some correspondence between

Table 9(b)
Experimental Energies of the Satellite States A-F of HCl.

Energy (eV)
A
26.003
26.212
26.331
26.585
26.780
B
27.036
27.318
27.576
28.822
28.065
C
28.332
28.606
28.837
29.052
29.227
D
28.461
28.755
28.958
29.370
E
29.507
29.751
29.981
30.391
F
29.652
29.865
30.067
30.269

theoretical and experimental work, any assignment of states in this region of the photoelectron spectrum of HCl will remain speculative until the theory yields further information. Calculation of the vibrational behaviour of states would be of particular value.

9.4 Atomic Autoionisation following Photodissociation of HCl

The collection energy range 2D spectrum of figure 9.4 shows a number of features of constant kinetic energy. These have been summed in the vertical constant collection energy direction to produce the spectrum shown in figure 9.6.

The process creating these features is one of neutral photodissociation of HCl, leaving the chlorine fragment in an excited state, which then decays by electron emission to a state of Cl^+.

$$h\nu + HCl \rightarrow HCl^* \rightarrow H + Cl^* \searrow H + Cl^+ + e$$

The onset of this process occurs as the photon energy reaches about 22eV (see figure 9.4). It is at this point that the photon has enough energy to excite the HCl molecule into a repulsive neutral state lying energetically above the ground state of the fragments. This is shown schematically in figure 9.7, where the ground state of Cl^+ is shown to be a triplet, thus explaining the triplet groups of lines in the spectrum.

As the photon energy is increased higher energy repulsive neutral states of HCl become accessible. These dissociate to leave the chlorine fragment in a higher excited state. Electrons of higher kinetic energy may now

Figure 9.6
The constant kinetic energy spectrum of HCl showing the assignment of lines due to autoionisation of atomic chlorine. Lines A to F are due to decay to the ground state triplet of Cl^+. Lines c to f are due to decay to the first excited state of Cl^+. Lines labelled with the same letter decay from the same excited state.

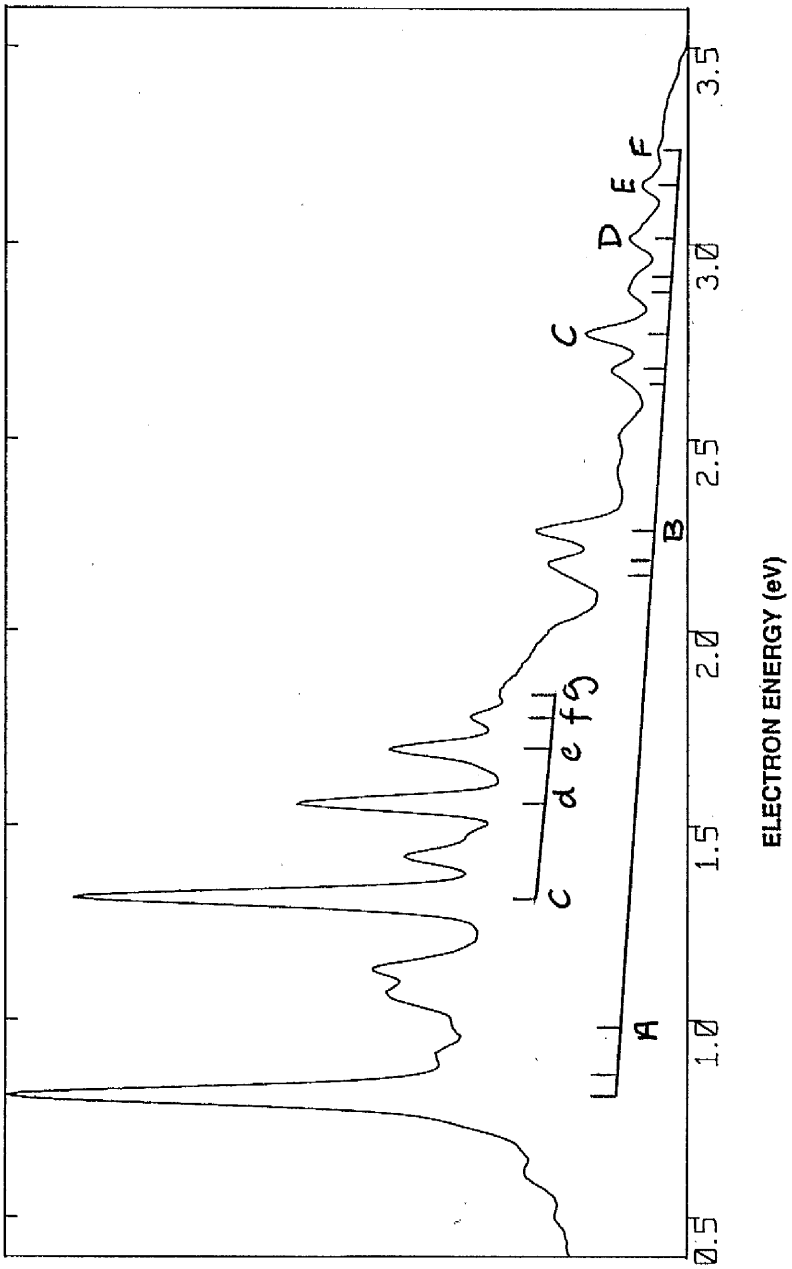

Figure 9.7
A schematic of the mechanisms of atomic autoionisation of chlorine obtained from the photodissociation of HCl.

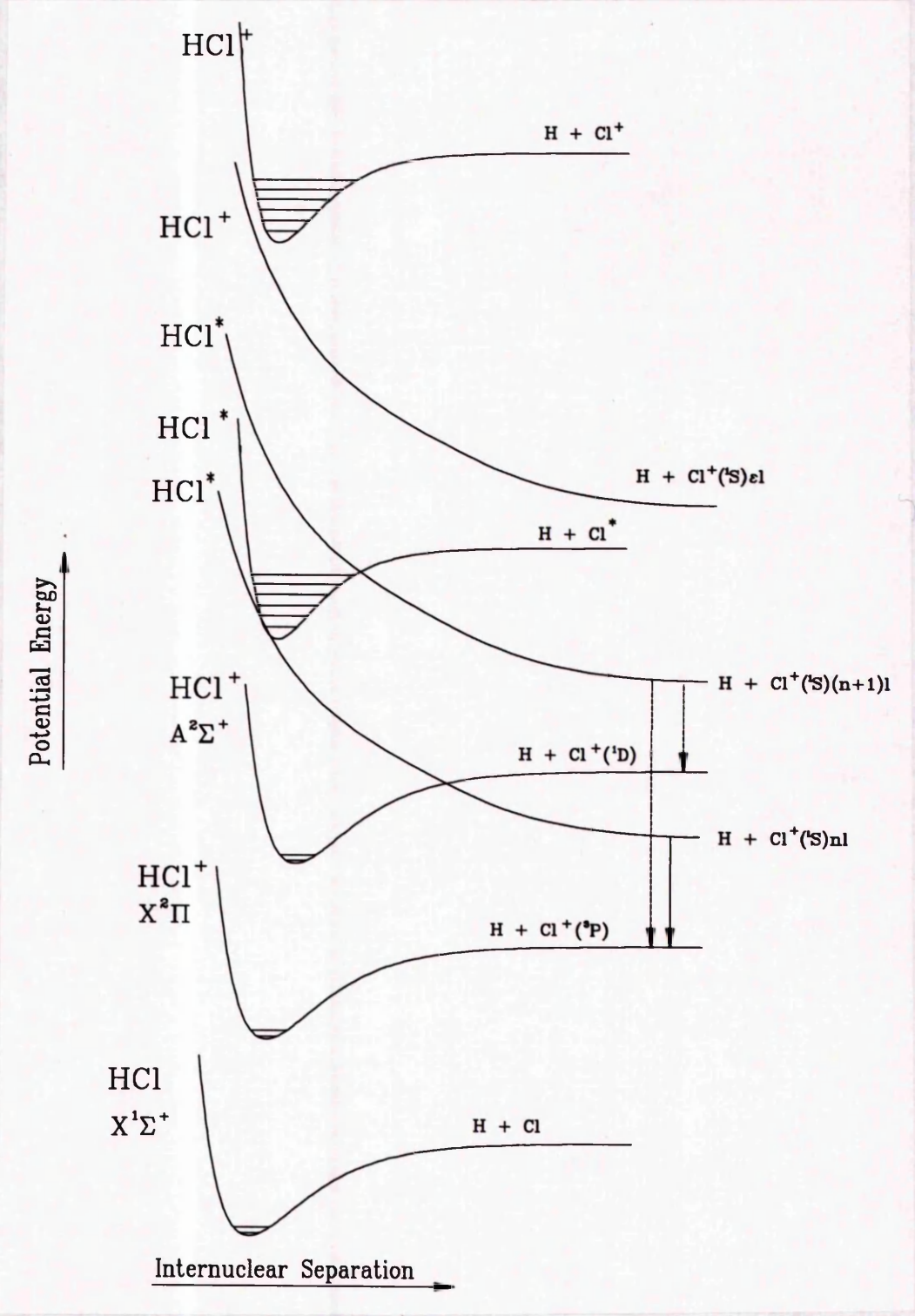

be emitted as the Cl^* decays by autoionisation to the ground state of Cl^+. Furthermore, if the repulsive neutral state places the excited chlorine fragment above the first excited state of Cl^+, then it may decay to that state by emitting an electron of lower kinetic energy.

As the photon energy is further increased it becomes clear that most of the repulsive neutral states of HCl^* belong to a Rydberg series converging on a repulsive ionic state of HCl^+. This is shown in figure 9.7. Dissociation from the states in the series places the chlorine atom in Rydberg states converging on an excited state of Cl^+.

Thus the majority of the lines observed in figure 9.6 can be successfully explained as the decay, by electron emission, of excited states of a Rydberg series of chlorine to the ground ($^3P0,1,2$) and first excited state ($^1D_0$) of Cl^+. This has been indicated on figure 9.6 by the groupings A-F, which represent decay to the ground state triplet, and c-g which represent decay to the first excited state.

Peaks labled with the same letter (disregarding upper and lower cases) correspond to decay from the same excited Rydberg state. They therefore differ in collection energy by the energy separation of the ground and first excited state of atomic chlorine. The energies of these features, together with other observed features are given in table 9(c).

Some structure has been observed in the excitation functions of the individual peaks of figure 9.4. Three such excitation functions, shown in figure 9.8, illustrate how the emission of electrons varies with photon

Table 9(c)
Experimental Energies of the constant kinetic energy lines from autoionisation of chlorine.

Assignment	Energy (eV)
A	0.996
B	2.262
C	2.676
D	3.010
E	3.154
F	3.239
c	1.313
d	1.559
e	1.701
f	1.779
g	1.839
-	1.068
-	1.128
-	1.420
-	1.481
-	2.415
-	2.504

Figure 9.8
Excitation functions of three lines due to atomic autoionisation of chlorine. From top to bottom the lines chosen are those labelled A, c and B in figure 9.6.

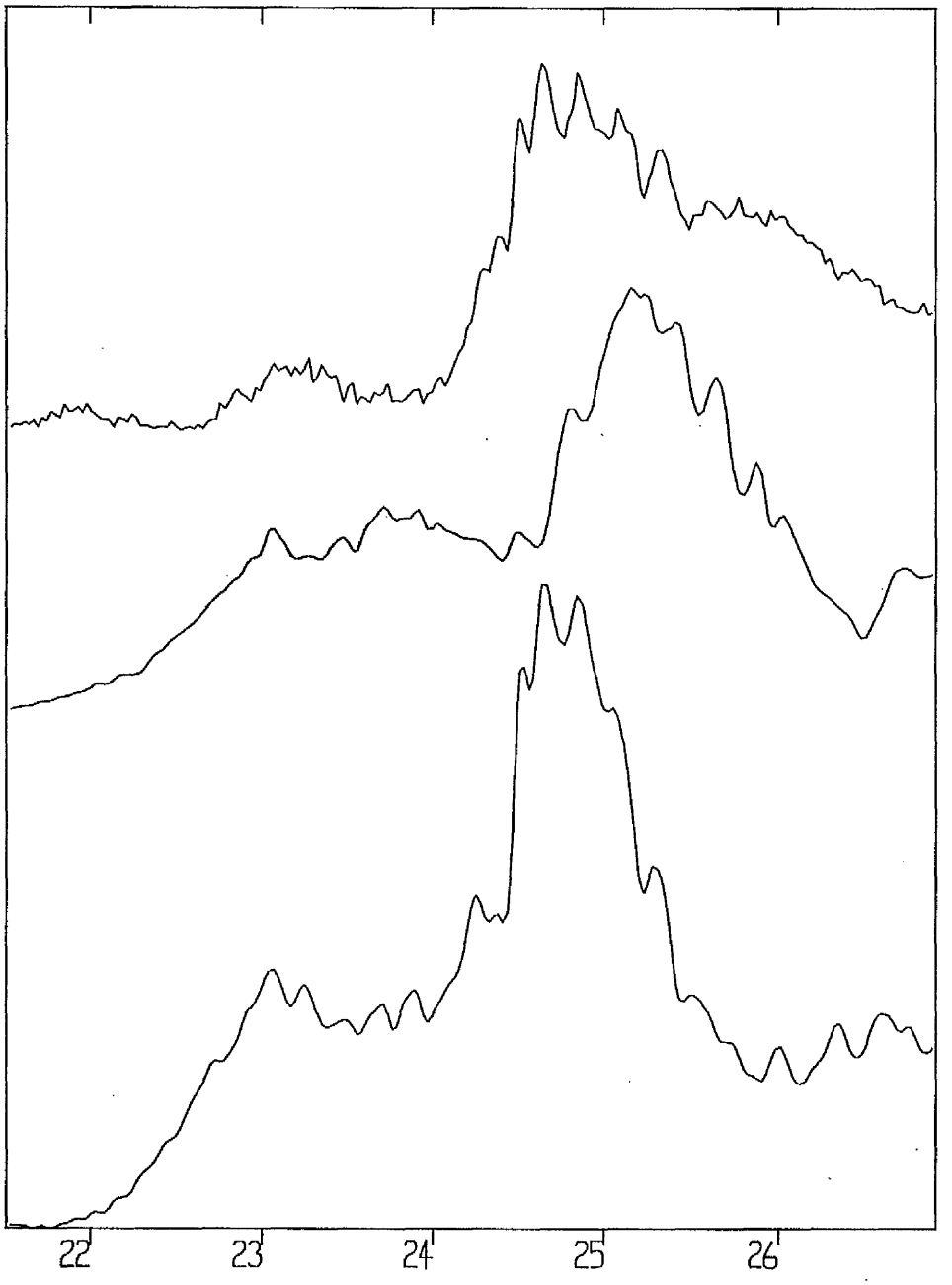

energy. It indicates that the population of the repulsive neutral state of HCl^* that leads to the emission of these electrons is subject to some fine structure as hν is increased.

This phenomenon can be explained by the existence of bound neutral states of HCl^*. As shown in figure 9.7, a bound neutral may lie energetically close to a repulsive neutral. In this case population of the repulsive neutral may occur through predissociation of the bound neutral. This is a process that varies with photon energy giving vibrational structure similar to that found in the excitation function.

9.5 The A-State of Hydrogen Chloride

The binding energy range 2D spectra of figure 9.1 has been summed in the vertical, constant binding energy direction, to produce the spectra in figure 9.9.

The peaks featured in this spectra are vibrations resolved from the $A^2\Sigma^+$ state. As mentioned above this feature is well described in the independent particle model as ionisation from the 5σ, Cl-H bonding orbital.

9.6 The X-State of Hydrogen Chloride

The binding energy range 2D spectra of figure 9.2 has been summed in the vertical, constant binding energy direction, to produce the spectra of figure 9.10.

The features are due to the ground state doublet $X^2\Pi$, which is well described in the independent particle model as ionisation from the

Figure 9.9
A photoionisation spectrum of the A-State of HCl obtained by the vertical summation of the BE2D data set shown in figure 9.1.

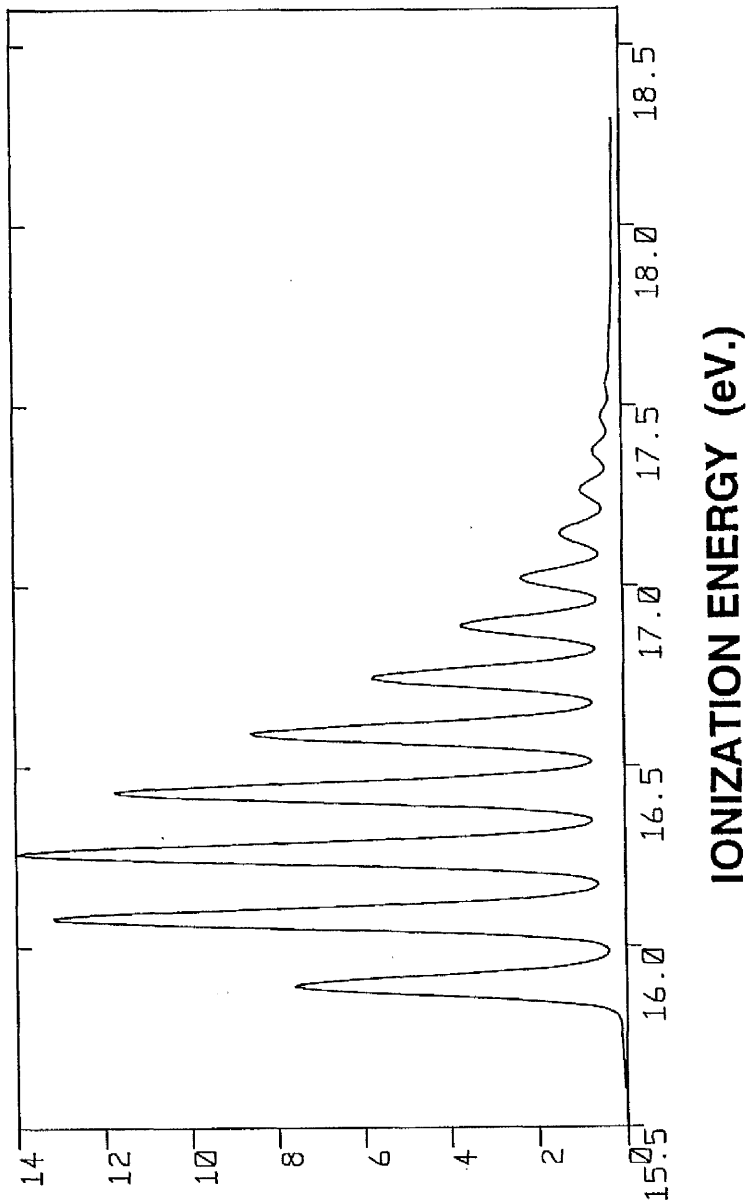

Figure 9.10
A photoionisation spectrum of the X-State of HCl obtained by the vertical summation of the BE2D data set shown in figure 9.2.

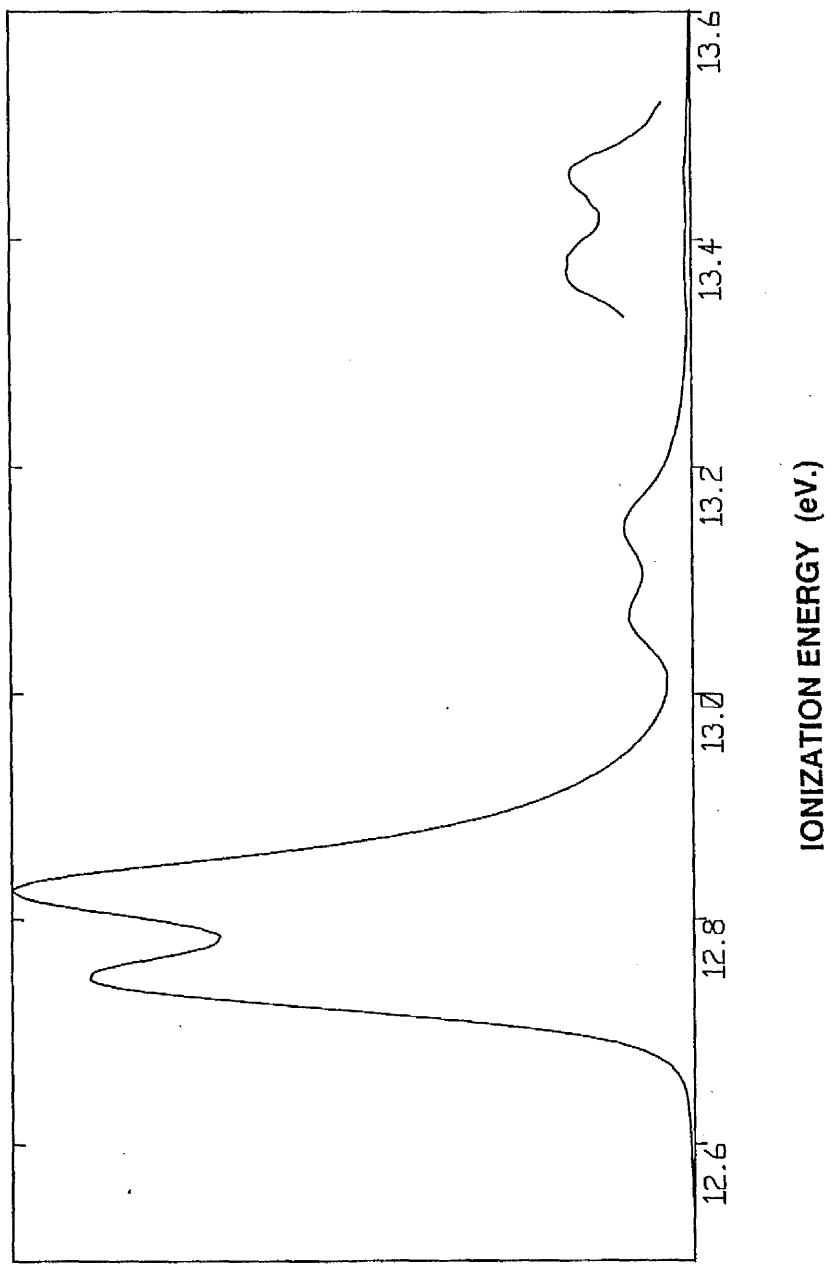

lone-pair 2π orbital.

An excitation function has been derived from one of the X-state vibrations and is shown in figure 9.11. The photon energy dependent structure revealed in this feature has a similar explanation to the structure found in the excitation function of the peak due to atomic autoionisation, figure 9.8.

With reference to figure 9.7, it is suggested that the excited neutral bound state of HCl^* which may predissociate via the repulsive state of HCl^* to give structure in the atomic lines, may alternatively decay to the ground state of HCl^+. These processes compete with each other, the most popular route of decay depending on photon energy, and produce structure in the excitation function.

9.7 Conclusion

The versatility of the experimental apparatus has been highlighted in an extensive photoelectron study of HCl. Improved resolution has revealed vibrational structure previously unobserved in the satellite spectrum. Comparison with the theory of Von Niessen and Tomasello has allowed some tentative assignments to be made, and highlighted the need for further theoretical advances to clarify the spectrum.

Finally, the mechanisms of atomic autoionisation and excitation of the A and X-states of HCl have been discussed.

Figure 9.11
An excitation function of the v=2 vibrational level of the X-State of HCl obtained from the BE2D data set shown in figure 9.2.

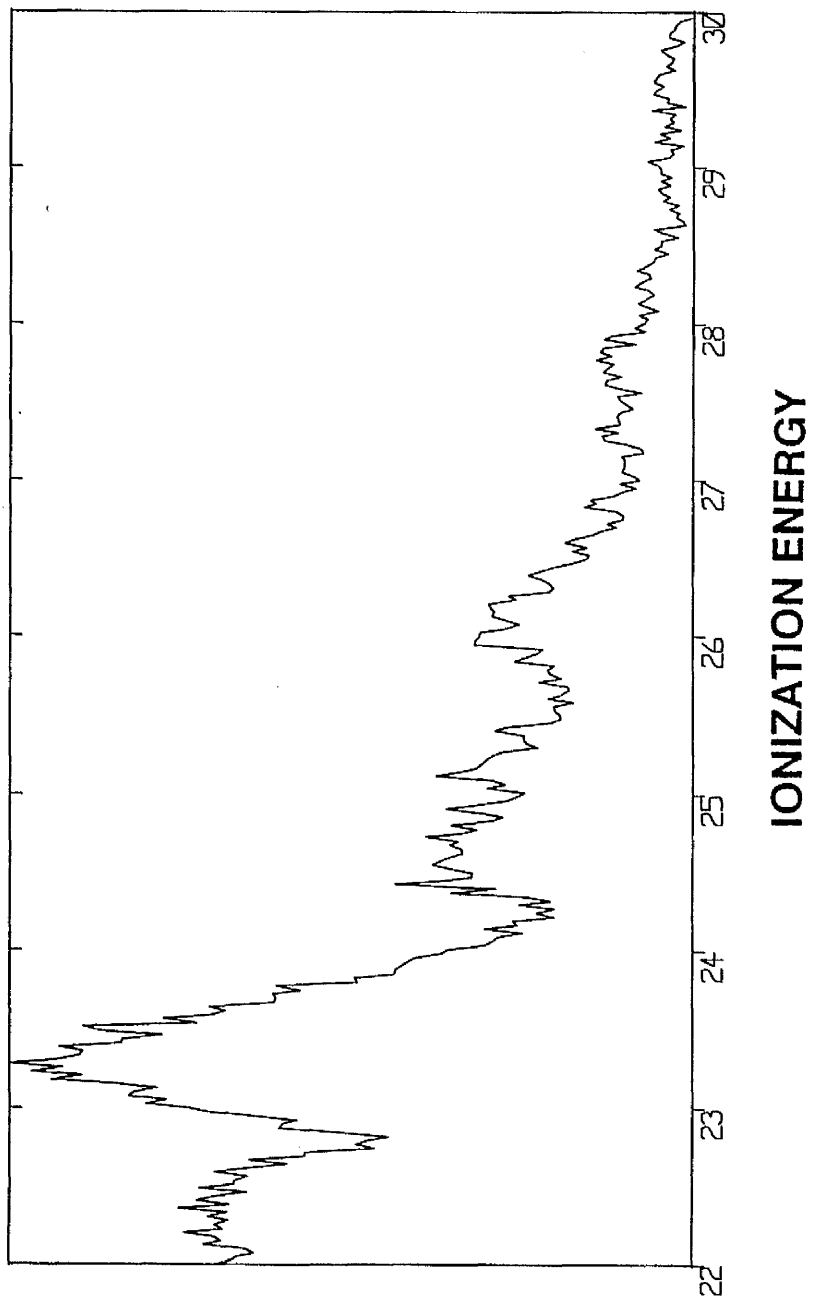

CHAPTER TEN

CONCLUSION AND FUTURE DEVELOPMENTS

A photoelectron spectrometer with a new position sensitive multidetector has been used at the Daresbury Synchrotron Radiation Source to investigate the inner-valence photoionisation of N_2, CO and HCl. A two dimensional data scanning technique has been employed at near threshold collection energies to maximise the sensitivity of this apparatus and has revealed many vibrationally resolved satellite lines for the first time.

A discussion of these results is given above with more detailed conclusions for each gas. Some assignments have been suggested from comparisons with the relevant calculations of various authors. The theoretical models used do not, however, describe the breakdown of the molecular orbital picture of ionisation with enough quantitative detail to completely clarify the spectra. It is hoped that the high resolution of this data will encourage further theoretical studies, including vibrational information.

The two dimensional method of data collection has allowed the simultaneous observation of constant kinetic energy features in the spectra of each gas. These have been assigned as due to atomic autoionisation following photodissociation of the neutral diatomic molecules and are due to the oxygen atom of CO and the chlorine atom of HCl. The peaks from autoionisation of the chlorine atom were found to be particularly strong due to the excitation of a neutral Rydberg series in HCl.

Future developments of this experiment include modification of the electron energy analyser to enable the angular distribution of photoelectrons to be measured. Also, the modular nature of the position sensitive multidetector will be exploited to extend the number of detecting pixels, initially to 116, reducing data collection time and increasing sensitivity.

REFERENCES

[1] Hertz H, **1887** Wien. Ann. **31** 983

[2] Einstein A, **1905** Ann. Phys. **17** 132

[3] King GC, Zubek M, Rutter PM, Read FH, MacDowell AA, West JB and Holland DMP, **1988** J. Phys. B. At Mol. Opt. Phys. **21** L403

[4] Vilesov FI, Kurbatov BL and Terenin AN, **1961** Sov. Phys. Dokl. **6** 490

[5] Blake AJ and Carver JH, **1967** J. Chem. Phys. **47** 1038

[6] Berkowitz J and Chupka WA, **1969** J. Chem. Phys. **51** 2341

[7] Bahr JL, Blake AJ, Carver JH, Gardner JL and Kumar V, **1971** J. Quant. Spectrosc. Radiat. Transf. **11** 1839

[8] Tanaka K and Tanaka I, **1973** J. Chem. Phys. **59** 5042

[9] McCarthy IE and Weigold E, **1976** Phys. Rept. **27c** 275

[10] Read FH, Comer J, Imhof RE, Brunt JNH and Harting E, **1974** J. Electron Spectrosc. Relat. Phenom. **4** 293

[11] Wiza JL, "Microchannel plate detectors", **1979** Nucl. Instrum. Methods **162** 587

[12] Fraser GW, "X- and γ-ray imaging using microchannel plates", **1984** Nucl. Instrum. Methods Phys. Res. **221** 115

[13] Richter LJ and Ho W, "Position sensitive detector performance and relevance to time resolved electron energy loss spectroscopy", **1986** Rev. Sci. Instrum. **57** 1469

[14] Siegmund OHW and Malina RF, "Detection of extreme UV and soft X-rays with microchannel plates: A review", in Multichannel Image Detectors (ACS symp. series 236) **1983** Vol II. Talmi Y, Ed. New York; ACS, 253

[15] Cromwell MH, Buck TM, Labuda EF, Dalton JV, Walsh EJ, **1967** Bell System Tech. J. **46** 491

[16] Gelius U, Basilier E, Svensson S, Bergmark T, Siegbahn K, **1973** J. Electron Spectros. and Relat. Phenom. **2** 405

[17] Basilier E, **1976** Nucl. Instrum. Meth. **138** 663

[18] Solid state Photodiode devices; EG&G Reticon.

[19] Boyle WS, Smith GE, **1970** Bell System Tech. J. **49** 587

[20] Hicks PJ, Daviel S, Wallbank B, Comer J. **1980** "An electron spectrometer using a new multidetector system based on a charge-coupled imaging device", J. Phys. E. Sci. Instrum. **13** 713

[21] Moak CD, Datz S, Garcia Santibanez F, Carlson TA, 1975 "A position sensitive detector for electrons", J. Electron Spectrosc. Relat. Phenom. **6** 151

[22] Gott R, Parkes W, Pounds KA, **1970** "The use of channel-multiplier arrays for one and two dimensional X-ray image dissection", IEEE Trans. Nucl. Sci **NS-17** 367

[23] Smith D, Adams NG, **1975** "An improved detector for a multicollector, cycloidal focussing, magnetic mass spectrometer", J. Phys. E. Sci. Instrum. **8** 44

[24] Timothy JG, Mount GH, Bybee RL, **1981** "Multi-anode microchannel arrays", IEEE Trans. Nucl. Sci **NS-28** 689

[25] McClintock WE, Barth CA, Steele RE, Lawrence GM, Timothy JG, **1982** "Rocket-borne instrument with a high resolution microchannel plate detector for planetary UV spectroscopy", Appl. Opt. **21** №17 3071

[26] Timothy JG and Bybee RL, **1975** "One-dimensional photon counting detector array for use at EUV and soft X-ray wavelengths", Appl. Opt. **14** 1632

[27] Salaneck WR, Gibson HW, Plummer EW, Tonner BH, **1982** "UV photoelectron spectroscopy of optically excited states in trans-polyacetylene", Phys. Rev. Lett. **49** 801

[28] Gurney BA, Ho W, Richter LJ, Villarrubia JS, **1988** "Multidetector electron energy-loss spectrometer for time resolved surface studies", Rev. Sci. Instrum. **59** 22

[29] Oba K, Sugiyama M, Suzuki Y, Yoshimura Y, **1979** "A 400 anode chevron microchannel plate PMT for high-energy applications", IEEE Trans. Nucl. Sci. **NS-26** 346

[30] Hatfield JV, York TA, Comer J, Hicks PJ, **1989** "Development of a new type of self scanned electron image sensing integrated circuit", IEEE J. Solid state circuits **24** №3 704

[31] Vanner KC, Jackson NF, Rhodes SJ, **1984** "Resin and chips", Physics Bulletin 158

[32] Iscoff R, **Oct. 1984** "Polyimides in semiconducter manufacturing", Semiconducter International 116

[33] Senturia D, Millar RA, Denton DD, Smith III FW, Neuhaus HJ, **Oct. 1985** "Polyimides and VLSI: A research perspective", in Proc. 2nd Conf. on Polyimides, Ellenville NY, 107

[34] York TA, **1989** Private Communication

[35] Singular Si8255 "Digital I/O and Counter card", Intel peripheral components book

[36] Marr GV and West JB, **1976** At. Data Nucl. Data Tables **18** 497

[37] Peatman Wm B, Gotchev B, Gürtler P, Koch EE, Saile V, **Sept. 1978** "Transition probabilities at threshold for the photoionisation of molecular nitrogen", J. Chem. Phys **69** 2089

[38] Åsbrink L, Fridh C, Lindholm E, Codling K, **1974** "Photoelectron Spectrum and Rydberg Transitions of CO" Physica Scripta **10** 183

[39] Wannberg et al, **1988** J. Electron Spectrosc. and Relat. Phenom. **47** 159

[40] Cederbaum LS, Domcke W, Schirmer J, Von Niessen W, **1986** "Correlation effects in the ionisation of molecules: Breakdown of the molecular orbital picture", Adv. Chem. Phys. (Wiley) 115

[41] Müller J, **1982** Int. J. Quantum Chem. **XXI** 465

[42] Schultz R, Schweig A, Zittlau W, **1983** J. Am. Chem. Soc. **105** 2980

[43] Langhoff PW, Langhoff SR, Rescigno TN, Schirmer J, Cederbaum LS, Domcke W, Von Niessen W, **1981** "Theoretical studies of inner valence-shell photoionisation cross sections in N_2 and CO", Chem. Phys. **58** 71

[44] Tomasello P, **1987** J. Chem. Phys. **87** 7146

[45] Schirmer J and Walter O, **1983** "Complete valence-shell ionisation spectra of N_2 and CO: Application of the Two-particle-hole Tamm-Dancoff approximation (2ph-TDA)" Chem Phys **78** 201

[46] Nichols JA, Yeager DL, Jøgenson P, **1984** J. Chem. Phys. **80** 293

[47] Von Niessen W, Schirmer J, Cederbaum LS, **1984** Comp. Phys. Rep. **1** 57

[48] Gelius U, Basilier E, Svensson S, Bergmark T, Siegbahn K, **1973** J. Electron Spectrosc. and Relat. Phenom. **2** 405

[49] Banna MS and Shirley DA, **1976** J. Electron Spectrosc. and Relat. Phenom. **8** 255

[50] Nilsson R, Nyholm R, Berndtsson A, Hedman J, Nording C, **1976** J. Electron Spectrosc. Relat. Phenom. **9** 337

[51] Potts AW and Williams TA, **1974** J. Electron Spectrosc. Relat. Phenom. **3** 3

[52] Krummacher S, Schmidt V, Wuilleumier F, **1980** "Inner shell photoionisation in molecules: the nitrogen case", J. Phys. B. Atom Molec. Phys. **13** 3993

[53] Morin P, Adam MY, Nenner I, Delwi he J, Hubin-Franskin MJ, Lablanquie P, **1983** Nucl. Instr. Meth. **208** 761

[54] Hamnet A, Stoll W, Brion CE, **1976** J. Electron Spectrosc. Relat. Phenom. **8** 367

[55] Cook JPD, Pascual R, Weigold E, von Niessen W, Tomasello P, **1990** Chem. Phys. **141** 211

[56] Herman MF, Freed KF, Yeager DL, **1981** Adv. Chem. Phys. **1** (Wiley)

[57] Loftus A and Krupenie PH **1977** J. Phys Chem. Ref. Data **6** 113

[58] Schirmer J, Cederbaum LS, Domcke W, von Niessen W, **1977** "Strong correlation effects in inner-valence ionisation of N_2 and CO", Chem. Phys. **26** 149

[59] Sambe H and Ramaker DE, **1986** "An interpretation of the N_2 photoelectron spectrum", Chem. Phys. Lett. **124** №5 420

[60] Gelius U, Basilier E, Svensson S, Bergmark T, Siegbahn K, **1973** J. Electron Spectrosc. and Relat. Phenom. **2** 405

[61] Nyholm R, Berndtsson A, Nilsson R, Hedmann J and Nordling C, **1977** Phys. Sci. **16 383**

[62] Wills AA, Cafolla AA, Comer J, **1991** "The production of Autoionising states of atomic oxygen by the photodissociation of O_2", in press.

[63] Cafolla AA, Redish T, Comer J, **1990** J. Phys. B: At. Mol. Opt. Phys. **22** L273

[64] Čermák V, **1974** "Electron spectroscopy of autoionising states of nitrogen atoms", J. Electron Spectrosc. Relat. Phenom. **3** 329

[65] Čermák V and Šrámek J, **1973** J. Electron Spectrosc. **2** 97

[66] Boumsellek S and Esaulov VA, **1990** J. Phys. B. **23** L605

[67] Krummacher S, Schmidt V, Wuilleumier F, Bizau JM, Ederer D, **1983** "Inner-shell photoionisation in molecules: the carbon monoxide case", J. Phys. B: At. Mol. Phys. **16** 1733

[68] French CL, Brion CE, Bawagon AO, Bagus PS, Davidson ER, **1988** "Electron momentum spectroscopy of the valence orbitals of CO: quantitative comparisons using wavefunctions up to the Hartree-Fock limit", Chem. Phys. **121** 315

[69] Bagus PS and Viinikka EK, **1977** Phys. Rev. A **15** 1486

[70] Honjou N, Sasajima T, Sasaki F, **1981** Chem. Phys. **57** 475

[71] von Niessen W, Cederbaum LS, Schirmer J, Dierckson GHF, Kraemer WP, **1982** J. Electron Spectrosc. Relat. Phenom. **28** 45

[72] Yousif M, Ramaker DE, Sambe H, **1983** "Comparison of autoionisation and photoelectron spectra for CO" Chem. Phys. Lett. **101** №4,5 472

[73] Adam MY, **1986** "Highly resolved photoelectron spectra of the HCl inner valence shell" Chem. Phys. Lett. **128** Nº3 280

[74] Cafolla AA, Comer J and Reddish T, **1988** "Autoionisation in HCl measured with a position-sensitive photoelectron spectrometer" J. Phys. B. At. Mol. Opt. Phys. **21** 3571

[75] York TA and Comer J, **1984** "Electron energy-loss studies using a position-sensitive multidetector electron spectrometer: the spectrum of HCl" J. Phys. B. At. Mol. Phys. **17** 2563

[76] Brion CE, Hood IH, Suzuki E, Weigold E and Williams GRJ, **1980** "Momentum distribution and ionisation potentials for the valence orbitals of HF and HCl" J. Electron. Spect. **21** 71

[77] Daviel S, Ilda Y, Carnovale F and Brion CE, **1984** "Absolute oscillator strengths for the partial photoionisation ionic fragmentation and photoabsorption of HCl" Chem. Phys. **83** 391

[78] Suzuki IH, Brion CE, Weigold E and Williams GRJ, **1980** "Binding energies at different momenta for the valence orbitals of HCl by the Binary (e, 2e) method" Intern. J. Quantum Chem. **18** 275

[79] Von Niessen W and Tomasello P, **1989** "Inner valence photoelectron spectra_from qualitative to quantitative results" J. Mol. Struct. (Theochem.) **202** 213

[80] Kimura K, Katsumata S, Achiba Y, Yamazaki T and Iwata I, Handbook of HeI photoelectron spectra of fundamental organic molecules (Japan Scientific Societies Press, Tokyo/Halsted Press, New York **1981**)

[81] Thorburn R, **1959** "Ionisation and dissociation by electron impact in F, HF, Cl_2 and HCl" Proc. Phys. Soc. (London) **73** 122

[82] Doorman FH and Morrison JD, **1961** "Double and Triple ionisation in molecules induced by Electron Impact" J. Chem. Phys. **35** 575